CHARACTERIZATION OF NANO-PHASE SEGREGATION IN MULTICOMPARTMET MICELLE AND ITS APPLICATIONS: COMPUTATIONAL APPROACHES

A Dissertation
Presented to
The Academic Faculty

by

Byeongjae (Ben) Chun

In Partial Fulfillment
of the Requirements for the Degree
Doctor of Philosophy in the
School of Chemical & Biomolecular Engineering

Georgia Institute of Technology
December 2015

CHARACTERIZATION OF NANO-PHASE SEGREGATION IN MULTICOMPARTMET MICELLE AND ITS APPLICATIONS: COMPUTATIONAL APPROACHES

Approved by:

Dr. Seung Soon Jang, Advisor
School of Materials Science and
Engineering
Georgia Institute of Technology

Dr. David S. Sholl, Co-Advisor
School of Chemical & Biomolecular
Engineering
Georgia Institute of Technology

Dr. Sven Holger Behrens
School of Chemical & Biomolecular
Engineering
Georgia Institute of Technology

Dr. Christopher W. Jones
School of Chemical & Biomolecular
Engineering
Georgia Institute of Technology

Dr. J. Carson Meredith
School of Chemical & Biomolecular
Engineering
Georgia Institute of Technology

Date Approved: [October 30, 2015]

성공보다 더 값진 실패를 위하여

ACKNOWLEDGEMENTS

Over the past five years I have received valuable supports and encouragements from a great number of individuals. First of all, I would like to thank my academic advisor Prof. Seung Soon Jang for his continuous supports and scientific training over the course of my PhD studies. Especially, I cannot thank enough for providing me an opportunity to join his group when I went through a tough time to seek for research advisor in my first year. Since then, his encouragement and advice have helped me improve as a researcher. Without his guidance, I would not be here. I also greatly thank my co-advisor Prof. David S. Sholl, who has kindly allocated his time to help me build my research career. Every meeting and discussion we have had over the years have been significantly valuable and helpful to resolve not only academic difficulties but also personal matters.

I was very honor to have my PhD committees whose expertise is highly related fields to my studies. I would like to thank Prof. Svan Holger Behrens, Prof. Christopher W. Jones, and Prof. J. Carson Meredith for accepting my request to be a member of committees, showing their interest and providing great suggestions for my research. I would like to thank them individually. Prof. Behrens, whose specialty is substantially related to this work, has provided his experimental perspective that helped start my thesis in the beginning. Prof. Jones, one of principle investigators for my major project funded by Department of Energy, have showed his genuine interest in computational research and provided his critical opinions to shape my thesis work over the last three years. I also personally thank Prof. Meredith for encouraging me seeking for academic advisors

work could have been done without ACS Petroleum Research Funding and Department of Energy.

Throughout my graduate study, I have had an unforgettable time with many bright friends. Especially, during my captainship for the Korean soccer club, Dokdo United, I met many individuals from all different fields and learned teamwork. I want to thank my team members who have followed me without any complains. Likewise, my officemate Khaldoon Abu-Hakmeh must be appreciated since we have helped each other during rough time we had. I believe he will complete his PhD studies with great success.

Without supports from my family I would never be here. Since 2005, my parents have lived without their youngest son but they have never showed their worries and frustrations when I had tough time to settle in the United States. Their unconditional love and patience have made me capable of completing my thesis work and becoming who I am now. Special thanks go to my aunt Sun Sook Kim who has been like my mother since I moved to the United States. She has never hesitated to support and advise me whenever I requested. I also want to thank my big brother Byeung Gak for sacrificing his dream to study in the United States for me. I am grateful to have him by my side. I always wish him and my niece So Youl the best of luck. I would never forget all the supports from my family in Virginia throughout my PhD studies, as well.

The last person I would like to thank is my wife Hennim for understanding and supporting me unconditionally during my time in Georgia Tech. I consider myself as the luckiest person in the world since she is always there for me. In spite of my silly mistakes and childish behavior, she has been always a patient and wise one to arrange things

correctly. Without her none of my career would have been accomplished. I do not know how to thank her enough for being by my side and loving me regardless.

I thank all who never stop believing and supporting me.

Byeongjae (Ben) Chun, Atlanta, October 26th 2015

TABLE OF CONTENTS

LIST OF TABLES

LIST OF FIGURES

SUMMARY

Micelle is a spherical-nanoscale aggregate with multiple discrete regions formed by the difference in solubility in particular solvent environment. The fundamental micellar structure can be often obtained from the dilution of surfactants in solvent. Due to the ability to synthesize multi-functionalized block copolymers, the advanced micellar systems are nowadays manufactured using block copolymers and its outcomes have shown great potential for the diverse range of applications from drug delivery to reaction chemistry.

The driving force of the process to synthesize micellar structures, so called micellization, is simply by the difference in the incorporation of components of micelle-building materials with solvent environment. For the case of polymeric micelle, the micelle is often synthesized as multicompartment aggregates, the body of which has more than one region composed of blocks with similar physical properties. The size, shape, and chemical properties of these regions in micellar structure are controlled by the particular nature of block copolymer that determines the characteristics of noncovalent interactions among neighboring components.

Since there are many variables that are significantly influential on the properties of micelle, this thesis work has focused on utilizing robust computation methodologies to profoundly understand the correlation of structural and thermodynamic properties with the tested variables. Using a number of computing schemes including Density Functional Theory (DFT), molecular dynamics (MD) simulations, and dissipative particle dynamics

(DPD), the study investigated the properties of micelle in wide-ranging scale from atomistic to macromolecular structure.

The wettability of the hydrophilic calcium carbonate surface is altered by the adsorption of amphiphilic carboxylate compounds forming an oleophilic layer on the surface. In this study, the nature of amphiphilic materials that often form micellar aggregated structures in the presence of solvent was investigated. Therefore, the adsorption of carboxylates such as benzoate and stearate on the calcium carbonate ($10\bar{1}4$) surface was characterized using DFT and MD simulations. From our DFT computations using PBE-D3 method, the binding energy of a carboxylate adsorbed on the calcium carbonate in water phase is calculated to be −29.45 kcal/mol, which is utilized to develop a new set of force field parameters for molecular simulations. The optimal adsorption density of the carboxylates on the carbonate surface is determined using the newly developed force field: the adsorption of benzoate shows two probable adsorption densities at 20.20 Å2/molecule and 40.40 Å2/molecule, while the stearate adsorption has a single optimum at 20.20 Å2/molecule, which is in a good agreement with the experimental results. Lastly, through performing the steered molecular dynamics simulations to characterize the potential of mean force for the desorption of the carboxylate molecules from the calcium carbonate surface, the binding free energy is calculated as −148 kcal/mol in the presence of oil phase. This indicates that due to the stability of the carboxylate monolayer on calcium carbonate, the spontaneous desorption of carboxylate molecule from the calcium carbonate surface in nature is not likely.

To validate the scheme of modeling micelle structures, a micelle consisting of 60 sodium dodecyl sulfate (SDS) molecules in water phase using MD simulation method.

The dimension of the micelle is evaluated as ~16 Å and ~21 Å for the radius of gyration and geometric radius, respectively, which are well agreed with the previous studies. By calculating the formation energy, it is found that the stability of micelle is driven by the interaction of the micelle with water phase. Via Connolly surface analysis, it was found that ~58% of the micelle surface is occupied by the hydrophobic alkyl tails. The conformation analysis shows that the individual SDS molecules are bent within the micelle and are not aligned radially from the center-of-mass of the micelle. However, it turns out that the micelle is well packed with a small free volume (0.35% of the micelle volume) which does not allow the diffusion-in of water molecules. The PMF required to drag a water molecule from water phase to the center-of-mass of micelle is calculated as ~10 kcal/mol while the PMF for a SDS molecule to be dissociated from the micelle is ~13 kcal/mol, both of which demonstrate that the micellization is driven by minimizing unfavorable interaction of hydrophobic alkyl tail of SDS molecule with water phase.

For the next step, the scope of study was expanded to the application of micelle nanostructures, which is the case of micellar catalysis. Through the error and trial, to facilitate the simulation for complicated structure like micelle, the thermodynamics of phase segregation in the micelle system was individually investigated since the phase segregation among components determine the characteristics of micellar structure. Moreover, it is desired to build the correlation of the degree of phase segregation with the functionalities of micelle as nanoreactor. The hydrolytic kinetic resolution (HKR) of epoxides has been performed in a shell-crosslinked micellar (SCM) nanoreactor consisting of amphiphilic triblock copolymers based on poly(2-oxazoline)s polymer derivatives with attached Co (III)-salens to the micelle core. To investigate the effect of

the molecular interaction of reactant/product molecules with the SCM nanoreactor on the rate of HKR, we calculated the Flory-Huggins interaction parameters (χ) using the molecular dynamics simulation method. It is hypothesized that a specific region limits the permeation of reactant or product molecules within the micellar structure. There are two properties that govern the permeation: the permeability of materials and the miscibility of molecule in a permeate. Under the assumption that the polymer network in the micelle is flexible enough to wiggle, the incorporation of molecules in the complex is recognized as a property directly linked to the permeation. For this, the blend systems were constructed with various compositions such as 15, 45, and 70 wt% of the reactant/product molecules with respect to the polymers such as poly(2-methyl-2-oxazoline) (PMOX), poly(2-(3-butinyl)2-oxazoline) (PBOX), and poly(methyl-3-(oxazol-2-yl) pentanoate with Co(III)-salen (PSCoX). From the χ parameters, we demonstrate that the miscibility of reactants/products with polymers has a strong correlation with the experimental reaction rate of the HKR: phenyl glycidyl ether (Reac-OPh) > epoxyhexane (Reac-C4) > styrene oxide (Reac-Ph) > epichlorohydrin (Reac-Cl). To validate this finding, we also conducted the potential of mean force analysis using steered molecular dynamics simulation for the molecular displacement of Reac-Cl and Reac-OPh through PMOX and PSCoX, revealing that the free energy reduction was greater when Reac-OPh molecule enters the polymer phase compared to Reac-Cl, which agrees with the findings from the χ parameters calculations.

For further analysis for the effect of physical and chemical properties of blocks on the micellar nanostructure, DPD simulations were employed using the POXs block copolymers. The input parameters of DPD simulation were obtained from the Flory-

Huggins interaction parameters using the Hildebrand Solubility parameters of each component, which allows to characterize the phase segregation without testing the systems of mixture. The reactants and products of the HKR were introduced to the system to investigate their association with each domain and distribution in the interior of micelle. According to the results of the simulation, the molecules with high tendency to be associated with individual blocks, the study of which was completed from the previous task, were also observed to be well-dispersed in the complex of micelle. On the other hand, the immiscible reactants and products in those polymers displayed weak association. This agreement of two methods indicated that the results of DPD simulation would exclusively illustrate micellar structures within fairly short amount of computation time.

The computational procedure to characterize and predict aggregated nanoparticle, particularly micellar structures, was performed at various scales ranging from atomistic scale to mesoscale. Via the computation at atomistic level, not only was the thermodynamics involved in the hydrophobic effect characterized using the free energy calculation, but also the physical and chemical properties of monomeric units and additives (reactant/product molecules) were characterized to explain the experimental results by employing the Flory-Huggins theory. The mesoscale simulation like DPD simulation generated the series of micelle structures with various block copolymers so that the experiment can be started from certain models, which reduces the cost of research and enables to predict the outcome on very short time-scales.

CHAPTER 1

INTRODUCTION

1.1. Micelle Nanostructure Materials

The ability to control the physical and chemical properties of organic materials on the nanometer size scale has received growing attention due to their wide-ranging applications from medicine to reaction chemistry.[1-3] The establishment of advanced chemistry to synthesize small molecular precursors such as block copolymers leads to the control of supramolecular structures.[4, 5] To facilitate the synthesis of nanostructures as well-functionalized materials for the applications, efforts have been made through numerous studies to tweak both covalent and noncovalent interactions to form robust multi-functional blocks such as functionalized block copolymers.[6-9] The formation of nanostructures occurs via the assembly of amphiphilic via noncovalent interactions in solvent environment. This process so called the dimensional evolution of organic chemistry[10] is widely employed to produce various types of nanostructures for a number of applications.[5]

Based on the nature of noncovalent interactions, their dimensional evolution leads to the formation of various nanostructure architectures such as spheres, toroids, helices, rods, disks, vesicles and tubes.[1, 11-14] Spherical micelles and nanoparticles among many structures are perhaps the most common and interesting outcome of the self-assembly, having a remarkable potential in applications ranging from drug delivery vehicles[1, 2, 10, 15, 16], molecular imaging agents[5], microelectronic devices[17], and nanoreactor containing reaction agents[5, 18, 19].

In this thesis, we focus on developing robust methodologies based on computation to predict and understand structural and thermodynamic properties of micelles at both atomistic- and macro-scale. Using molecular dynamics (MD) simulation, both compatible

and incompatible interactions within multicomponent systems of amphiphilic materials and solvent were recognized and expressed qualitatively and quantitatively, which leads to the insight of the structural and thermodynamic properties of micellar system.

1.2. Versatility of Block Copolymer based Micelle

Aided by the recent advances established in polymer chemistry, the ability to design block sequences allows to synthesize well-defined amphiphilic block copolymers, which therefore allows for structural and chemical control over the properties of micellar aggregates.[1, 2, 4-6, 9, 18] As a result, the synthesis technologies lead to being able to adjust the polymer properties and achieve excellent versatility in chemical nature of these aggregates.
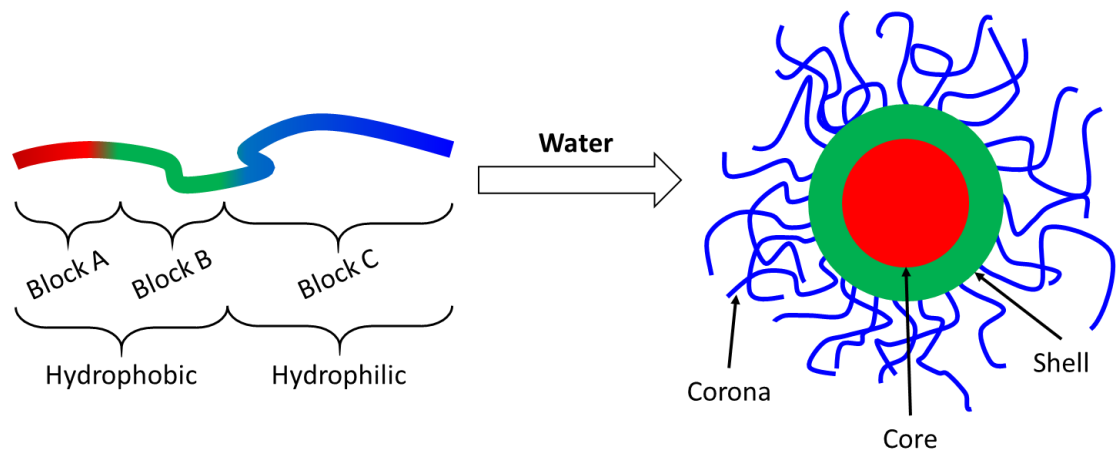
Figure 1.1. Schematic representation of micellization of amphiphilic materials in aqueous solution

The physical and chemical characteristics of each segregated domain shown in Figure 1.1 are inherited from the nature of components forming the domains. For instance, the state of internal micelle can vary as glassy, crystalline, amorphous, or fluid-like, based on the chemical structures of components.[5, 18] In the case of a multicompartment micelle, the aforementioned nature is utilized to achieve a high degree of control over morphologies of micellar structure.[1, 4-9, 11-13, 17] In addition, particular functional groups/moieties of monomeric units bring about functionalizing micelles. The electrochemical properties of

micelle, for example, can be modified using the ionic functional groups on the shell layer so that the layer can be positively- or negatively-charged for certain purpose.[5, 20] Furthermore, the reactions among reactive moieties resulting in covalently linking the polymer chains allows for subsequent stabilization of the micelle , which is known to be the cross-linking reaction throughout specific domain.[3, 5, 15, 16, 21-28]

Catalytic functional groups or catalyst-containing organic substrates can be embedded in the desired region of micelle depending on their purpose.[6, 18, 29-36] Commonly, embedding a catalyst into the core compartment forms a high concentration of catalysts within the limited volume of the micelle core, which provides a favorable condition for catalytic reactions.[18, 30-32] In some cases, the polymer chains of the micelle can carry two or more reactive sites so that a single micelle system is used for the consecutive reactions.[31] Moreover, the micellar nanostructure is often used as a living-cell like system for the drug delivery applications.[1, 2, 10, 15, 16] Micelle drug containers can be considered as a smart system that releases drugs or encapsulated contents at the target site in the biological system by responding to their surroundings, such as pH[37] or thermal conditions[38]. Due to this great potential of micelle materials for various applications including micellar catalysis and drug delivery, there have been a number of experiments[4, 5, 18] and simulations[39-55] performed by numerous researchers to understand unique properties and facilitate the versatility of micellar complex for improving their performance in each case.

1.3. Phase Segregation

The major driving force for the self-assembly of amphiphilic materials is the decrease in the free energy of system, in which the hydrophobic components spontaneously tend to form the micelle core to minimize the incompatible noncovalent interaction with water phase.[5] Meanwhile, the hydrophilic parts protect the micelle core from the water environment by forming the micelle outer shell. This is a result of the hydrophobic effect.[5]

Chapter 3 and 4 include further discussion regarding the behavior of classical amphiphilic molecules such as surfactants in two different environments.

Whereas the hydrophobic effect is the driving force for the micellization of block copolymers in water solvent condition, the formation of compartmentalized structure within micelle core or shell is governed by the difference in the hydrophobicity among components.[5] The compartmentalized structure within the confined region is often achieved by difference in the molar mass of the monomers for the case of hydrocarbon based classical amphiphilic block copolymers such as poly(ethylene oxide-block-propylene oxide)[56] or poly(styrene-block-methacrylic acid)[57]. The larger the monomeric unit is, the stronger its hydrophobicity is, and the inner its phase is located within nanostructure. However, the use of hydrocarbon-based polymers for synthesizing multicompartment micelle can be difficult because there is still similarity in chemical nature of the segments, which can lead to the weak segregation among components. Recently, the synthesis of multicompartment nanoparticles has been successful by maximizing the incompatible interactions of hydrocarbon and fluorocarbon hydrophobic segments for the core.[4, 8, 9, 11, 58-62]

1.4. Multicompartment Micelle Nanoreactor

Enzymes in natural systems have been known as the smart nanoreactor with high catalytic activity and specificity, which are formed by the perfect placement of amino acid residues during the folding of protein chains.[36, 63] These active sites are composed based on the physical and chemical properties of residues such as shape, size, hydrogen bonding, and hydrophobicity.[1, 11-14] The combinations of those allow numerous reactions to occur simultaneously in nature.

Great efforts to mimic these highly sophisticated and intelligent systems have been made in macromolecular chemistry.[18, 29-35, 63] Recent results in this field have shown the

ability to synthesize polymers able to assemble well-defined complex nanostructure such as core-shell micelles as scaffolds in nanoreactor technology (Figure 1.2.).[18, 31]
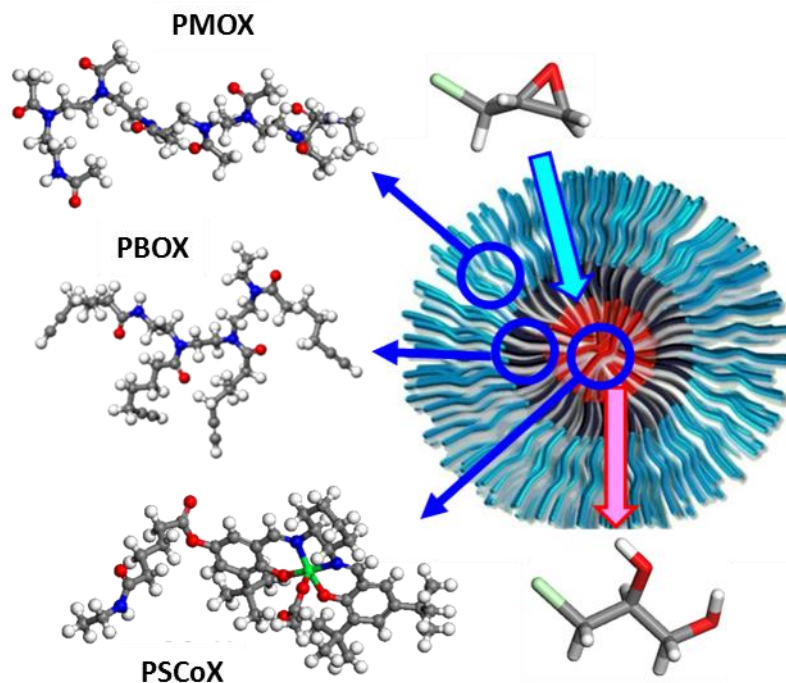
Figure 1.2. Schematic representation of poly(2-oxazoline) (POX) based multicompartment micelle nanoreactor for the hydrolysis kinetic resolution of epoxides. POX block copolymer consists of poly(2-methyl-2-oxazoline) (PMOX), poly(2-(3-butinyl)-2-oxazoline) (PBOX), and poly(methyl-3-oxazol-2-yl) pentanoate with Co(III)-salen (PSCoX). The molecule entering the core region is a reactant (epoxide) and the molecule exiting from the micelle is a product (diol).[31]

High increase in the local concentration of both substrates and catalysts has been observed within the confined reaction pocket of micelles. Since the general reactive sites in the micelle are located in the core domain, this increase enhances in reaction rates. In addition, the rest of micellar structure encapsulates the entire active sites, which protect the functionality from degradation or deactivation by solvent environment.[18, 31] For enhancing the stability of micelle, cross-linking chemistry is often utilized to covalently bond polymer chains. Weck and his coworkes[31] utilized Co(III)—salen catalyst supported by poly(2-

oxazoline) shell cross-linked multicompartment micelle (SCM) for the hydrolytic kinetic resolution (HKR) of epoxide. The hydrophobic component of micelle building block copolymer containing catalysts formed the highly reactive site within the core domain as the micellization of polymers occurred in water. The following process, in which the monomeric units of micelle structure are cross-linked, resulted in the outstanding enhancement of recycling properties with up to 8 cycles.[31]

1.5. Characterization of Micelle

Advanced small-angle light scattering or transmission electron microscopy technique has been available to characterize the internal structure of nanoparticles at micro-scale level.[5] For instance, in the work of Skrabania and coworkers[62], they rigorously characterized the internal structure of multicompartment micelle, which was a result of the self-assembly of ternary, hydrophilic-lipophilic-fluorophilic block copolymers. Their goal was to observe any structural change as altering the sequence order of hydrophilic and lipophilic blocks. The analysis by cryogenic transmission electron microscopy (cryo-TEM) was performed and captured the noticeable segregation between lipophilic and fluorophilic domains within the confined core of micelle. With strong evidence obtained by the analyzing tool, they have established the correlation of block sequence with the morphologies of the core region.

Likewise, computational methods have been developed and employed to learn more about the influence of molecular architecture on the phase segregation in multicompartment micelle and provide predictive information in order to either reduce the experimental cost or enable analyzing the internal structure of nanoparticle. Such a theory like Flory-Huggins (FH) interaction theory, for instance, has been continuously modified and utilized to scale the degree of phase separation in binary mixture systems.[64-66] Recent computational works have shown that MD simulation is an effective tool to provide reliable thermodynamic information of binary mixture system, such as enthalpy and entropy of

mixing.[64] Therefore, using the MD simulation based methodologies, the FH interaction parameters are calculated to determine the characteristics of phase segregation at nano-scale, and the information can be used to experimentally design and synthesize new micelle building polymers. The characterization of phase segregation based on the FH theory are further described in Chapter 5.

Not only is it possible to numerically express the state of phase segregation via MD simulation, but also the morphologies within micellar aggregates can be qualitatively and quantitatively analyzed by mimicking the entire structure using various modeling schemes.[34, 39, 46, 49-55] Simulations at atomistic scale allows to profoundly understand the influence of component particularities such as hydrophobicity, hydrogen bonding, chemical nature, and so on. Meanwhile, mesoscale simulations, such as coarse-graining methods based on the force field parameters or dissipative particle dynamics (DPD) simulation, can be used to provide possible structures with variety of block copolymers and blending conditions, such as critical micelle concentration or critical micelle temperature, for directing experiments in spite of the loss of atomistic details.[40-44] In Chapter 6, the results of DPD simulations for nanoreactor application are introduced and followed by the suggested tasks for further investigation.

1.6. References

[1]   Riess, G. *Prog. Polym. Sci.* **2003**, *28*, 1107.

[2]   Allen, C.; Maysinger, D.;Eisenberg, A. *Colloids Surf. B. Biointerfaces* **1999**, *16*, 3.

[3]   Wooley, K.L. *J. Polym. Sci., Part A: Polym. Chem.* **2000**, *38*, 1397.

[4]   Laschewsky, A. *Current Opinion in Colloid and Interface Science* **2003**, *8*, 274.

[5]   O'Reilly, R.K.; Hawker, C.J.;Wooley, K.L. *Chem. Soc. Rev.* **2006**, *35*, 1068.

[6]   Li, Z.; Hillmyer, M.A.;Lodge, T.P. *Macromolecules* **2006**, *39*, 765.

[7]   Thünemann, A.F.; Kubowicz, S.; von Berlepsch, H.;Möhwald, H. *Langmuir* **2006**, *22*, 2506.

[8]   Lodge, T.P.; Rasdal, A.; Li, Z.;Hillmyer, M.A. *J. Am. Chem. Soc.* **2005**, *127*, 17608.

[9]   Kubowicz, S.; Baussard, J.F.; Lutz, J.F.; Thunemann, A.F.; von Berlepsch, H.;Laschewsky, A. *Angew. Chem. Int. Ed.* **2005**, *44*, 5262.

[10]   Hawker, C.J.;Wooley, K.L. *Science* **2005**, *309*, 1200.

[11]   Fu, G.D.; Phua, S.J.; Kang, E.T.;Neoh, K.G. *Macromolecules* **2005**, *38*, 2612.

[12]   Minatti, E.; Borsali, R.; Schappacher, M.; Deffieux, A.; Soldi, V.; Narayanan, T.;Putaux, J.L. *Macromol. Rapid Commun.* **2002**, *23*, 978.

[13]   Pispas, S.; Hadjichristidis, N.; Potemkin, I.;Khokhlov, A. *Macromolecules* **2000**, *33*, 1741.

[14]   Xu, J.;Zubarev, E.R. *Angew. Chem. Int. Ed.* **2004**, *43*, 5491.

[15]   Iijima, M.; Nagasaki, Y.; Okada, T.; Kato, M.;Kataoka, K. *Macromolecules* **1999**, *32*, 1140.

[16]   Rösler, A.; Vandermeulen, G.W.M.;Klok, H.-A. *Adv. Drug Del. Rev.* **2001**, *53*, 95.

[17]   Spatz, J.; Mößmer, S.; Möller, M.; Kocher, M.; Neher, D.;Wegner, G. *Adv. Mater.* **1998**, *10*, 473.

[18]   Lu, A.;O'Reilly, R.K. *Curr. Opin. Biotechnol.* **2013**, *24*, 639.

[19]   Narayan, S.; Muldoon, J.; Finn, M.G.; Fokin, V.V.; Kolb, H.C.;Sharpless, K.B. *Angew. Chem. Int. Ed.* **2005**, *44*, 3275.

[20]   Harada, A.;Kataoka, K. *Macromolecules* **1995**, *28*, 5294.

[21]   Procházka, K.; Baloch, M.K.;Tuzar, Z. *Makromol. Chem.* **1979**, *180*, 2521.

[22]   Guo, A.; Liu, G.;Tao, J. *Macromolecules* **1996**, *29*, 2487.

[23]   Zhang, L.; Katapodi, K.; Davis, T.P.; Barner-Kowollik, C.;Stenzel, M.H. *J. Polym. Sci., Part A: Polym. Chem.* **2006**, *44*, 2177.

[24]   Bronich, T.K.; Keifer, P.A.; Shlyakhtenko, L.S.;Kabanov, A.V. *J. Am. Chem. Soc.* **2005**, *127*, 8236.

[25]   Li, Y.; Lokitz, B.S.; Armes, S.P.;McCormick, C.L. *Macromolecules* **2006**, *39*, 2726.

[26]   Shanmugananda Murthy, K.; Ma, Q.; Clark Jr, C.G.; Remsen, E.E.;Wooley, K.L. *Chem. Commun.* **2001**773.

[27]   Thurmond, K.B.; Kowalewski, T.;Wooley, K.L. *J. Am. Chem. Soc.* **1996**, *118*, 7239.

[28]   Huang, H.; Kowalewski, T.; Remsen, E.E.; Gertzmann, R.;Wooley, K.L. *J. Am. Chem. Soc.* **1997**, *119*, 11653.

[29]   Ahn, H.;Park, M.J. *Macromol. Rapid Commun.* **2011**, *32*, 1790.

[30]   Cotanda, P.; Lu, A.; Patterson, J.P.; Petzetakis, N.;O'Reilly, R.K. *Macromolecules* **2012**, *45*, 2377.

[31]   Liu, Y.; Wang, Y.; Wang, Y.; Lu, J.; Piñón, V.;Weck, M. *J. Am. Chem. Soc.* **2011**, *133*, 14260.

[32]   Zhang, H.; Ding, L.; Chen, Y.; Yang, W.;Deng, J. *J. Polym. Sci., Part A: Polym. Chem.* **2012**, *50*,

[33]   Korovin, A.N.; Sergeyev, V.G.; Pyshkina, O.A.; Hanske, C.; Fery, A.; Wittemann, A.;Tsarkova, L. *Macromol. Rapid Commun.* **2011**, *32*, 462.

[34]   Cotanda, P.;O'Reilly, R.K. *Chem. Commun.* **2012**, *48*, 10280.

[35]   Onaca, O.; Hughes, D.W.; Balasubramanian, V.; Grzelakowski, M.; Meier, W.;Palivan, C.G. *Macromol. Biosci.* **2010**, *10*, 531.

[36]   Chandrawati, R.; van Koeverden, M.P.; Lomas, H.;Caruso, F. *Journal of Physical Chemistry Letters* **2011**, *2*, 2639.

[37]   Licciardi, M.; Tang, Y.; Billingham, N.C.; Armes, S.P.;Lewis, A.L. *Biomacromolecules* **2005**, *6*, 1085.

[38]   Wei, H.; Zhang, X.-Z.; Zhou, Y.; Cheng, S.-X.;Zhuo, R.-X. *Biomaterials* **2006**, *27*, 2028.

[39]   Bruce, C.D.; Berkowitz, M.L.; Perera, L.;Forbes, M.D.E. *J. Phys. Chem. B* **2002**, *106*, 3788.

[40]   Zhong, C.;Liu, D. *Macromol. Theory Simul.* **2007**, *16*, 141.

[41]   Yamamoto, S.; Maruyama, Y.;Hyodo, S.-a. *J. Chem. Phys.* **2002**, *116*, 5842.

[42]   Xin, J.; Liu, D.;Zhong, C. *J. Phys. Chem. B* **2007**, *111*, 13675.

[43]   Soddemann, T.; Dünweg, B.;Kremer, K. *Physical Review E* **2003**, *68*,

[44]   Chen, S.; Guo, C.; Hu, G.-H.; Liu, H.-Z.; Liang, X.-F.; Wang, J.; Ma, J.-H.;Zheng, L. *Colloid. Polym. Sci.* **2007**, *285*, 1543.

[45]   Storm, S.; Jakobtorweihen, S.;Smirnova, I. *J. Phys. Chem. B* **2014**, *118*, 3593.

[46]   Tang, X.; Koenig, P.H.;Larson, R.G. *J. Phys. Chem. B* **2014**, *118*, 3864.

[47]   Xu, Z.J.; Yang, X.N.;Yang, Z. *J. Phys. Chem. B* **2008**, *112*, 13802.

[48]   Uttarwar, R.G.; Potoff, J.;Huang, Y. *Ind. Eng. Chem. Res.* **2013**, *52*, 73.

[49]   Chun, B.J.; Choi, J.I.;Jang, S.S. *Colloids Surf. Physicochem. Eng. Aspects* **2015**, *474*, 36.

[50]   Abel, S.; Dupradeau, F.-Y.;Marchi, M. *J. Chem. Theory Comput.* **2012**, *8*, 4610.

[51]   Abel, S.; Sterpone, F.; Bandyopadhyay, S.;Marchi, M. *J. Phys. Chem. B* **2004**, *108*, 19458.

[52]   Amani, A.; York, P.; de Waard, H.;Anwar, J. *Soft Matter* **2011**, *7*, 2900.

[53]   Barone, V.; Casarin, M.; Forrer, D.; Monti, S.;Prampolini, G. *Journal of Physical Chemistry C* **2011**, *115*, 18434.

[54]   Bast, T.;Hentschke, R. *J. Mol. Model.* **1996**, *2*, 330.

[55]   Bogusz, S.; Venable, R.M.;Pastor, R.W. *J. Phys. Chem. B* **2000**, *104*, 5462.

[56]   Chiappetta, D.A.;Sosnik, A. *Eur. J. Pharm. Biopharm.* **2007**, *66*, 303.

[57]   Qin, A.; Tian, M.; Ramireddy, C.; Webber, S.E.; Munk, P.;Tuzar, Z. *Macromolecules* **1994**, *27*, 120.

[58]   Weberskirch, R.; Preuschen, J.; Spiess, H.W.;Nuyken, O. *Macromol. Chem. Phys.* **2000**, *201*, 995.

[59]   Kotzev, A.; Laschewsky, A.; Adriaensens, P.;Gelan, J. *Macromolecules* **2002**, *35*, 1091.

[60]   Kotzev, A.; Laschewsky, A.;Rakotoaly, R.H. *Macromol. Chem. Phys.* **2001**, *202*, 3257.

[61]   Stähler, K.; Selb, J.;Candau, F. *Langmuir* **1999**, *15*, 7565.

[62]   Skrabania, K.; Berlepsch, H.v.; Böttcher, C.;Laschewsky, A. *Macromolecules* **2010**, *43*, 271.

[63]   Bain, J.;Staniland, S.S. *PCCP* **2015**, *17*, 15508.

[64]   Pajula, K.; Taskinen, M.; Lehto, V.-P.; Ketolainen, J.;Korhonen, O. *Mol. Pharm.* **2010**, *7*, 795.

[65]   Thakral, S.;Thakral, N.K. *J. Pharm. Sci.* **2013**, *102*, 2254.

[66]   Kasimova, A.O.; Pavan, G.M.; Danani, A.; Mondon, K.; Cristiani, A.; Scapozza, L.; Gurny, R.;Möller, M. *J. Chem. Phys. B* **2012**, *116*, 4338.

CHAPTER 2

COMPUTATIONAL METHODS

Molecular dynamics (MD) simulation methods originated from theoretical physics during the 1950s.[1] In the early era of MD simulations, atoms were described by the so-called hard-sphere model in which the interactions of atoms were recognized through perfect collisions.[2] Then, a smooth, continuous potential was employed by Rahman to mimic real atomic interactions.[3] For the last six decades, MD simulations were developed for much more complex systems such as biomolecules[4], polymers[5], and metal-organic frameworks materials[6]. Since the versatility of MD simulation was recognized for characterizing various materials, there have been the increase in demand for developing highly advanced simulation techniques to mimic the physical properties of materials that are difficult to handle in experiment.

Since computing resources and MD codes became more accessible, the computational efforts to characterize a large complex of organic compounds, such as a micellar nanoparticle, have been made using a number of computation techniques.[7-11] Micellar models are known as the product of evolution of amphiphilic molecules, such as surfactant and lipid, in aqueous solutions.[12] Due to the ability to synthesize amphiphilic block copolymers with a high degree of control, it became feasible to synthesize highly functionalized polymeric multicompartment micelles.[13-16] Along the growth of interest in the micelle study, computational methodologies have been a powerful tool to assess the self-assembly of amphiphilic materials, thermodynamic and structural properties of equilibrated micellar systems, critical micellization conditions (temperature and concentration) and so on.[7-11]

In this work, we followed the procedure shown in Figure 2.1 to develop and implement computational methods to thoroughly understand the particular characteristics of materials and extend the study to its applications.
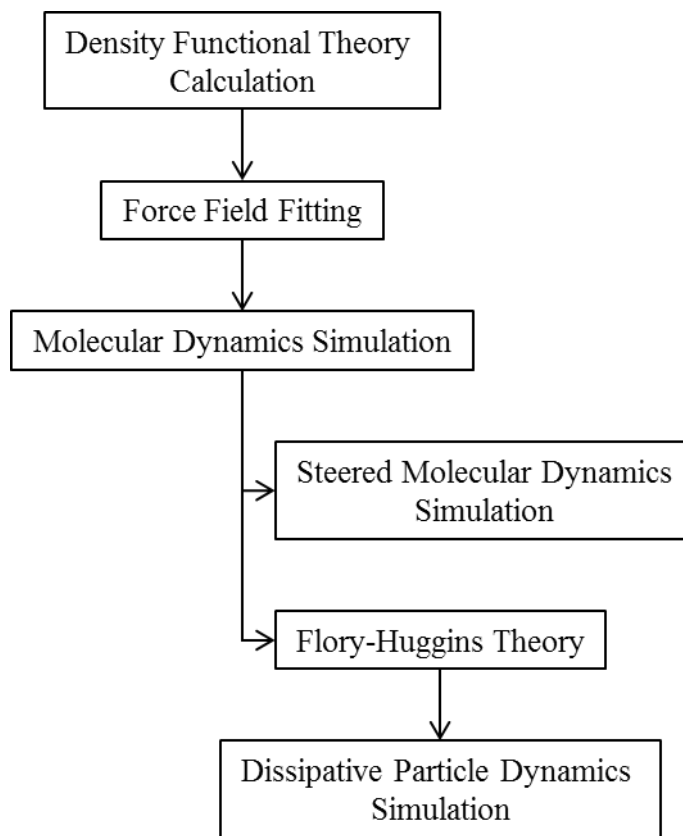
Figure 2.1. Work flow chart

2.1. Density Functional Theory Calculation and Force Field

Density Functional Theory (DFT) calculation can provide accurate solvation free energy, optimized structure, electrostatic information, etc. of target molecules.[17] Moreover, the obtained information can be used as the basis of input parameters of MD simulations. These input parameters are the so-called Force Field, which is a set of parameters and equations used to approximate the potential energy of materials. The potential energy is generally expressed as a sum of bonded and non-bonded interaction terms[18, 19]:

$$E_{total} = E_{bond} + E_{angle} + E_{torsion} + E_{inversion} + E_{vdW} + E_Q \qquad (1)$$

where E_{total}, E_{bond}, E_{angle}, $E_{torsion}$, $E_{inversion}$, E_{vdW}, and E_Q are the total energy, bond-stretching, angle-bending, torsion, inversion, van der Waals, and electrostatic energy components, respectively. The first four terms are the components of bonded interactions and the last two terms describe non-bonded interaction. The values of each term are initially estimated via DFT calculations. Since DFT calculations are prohibitively expensive for large scale (>1,000 atoms) simulations, a force field contains a set of simpler terms and corresponding parameters to reproduce the potential energy from DFT calculation. In the course of this study, both bonded and non-bonded potential energy terms were parameterized using force field fitting techniques to carry out robust simulations. The details of DFT calculation conditions and force field fitting are included in Chapter 3.

2.2. Molecular Dynamics Simulation Approach

MD simulation has advanced since the hard-sphere model was introduced. As the demands for elaborate characterization of nanomaterials increase along advances in synthesis techniques for applications, the role of computation methods became significant in materials science and engineering. MD simulation is still classified as a theoretical method. However, the impact of simulation is so powerful that the results interpreted in terms of physical properties of interest materials are used as prediction to design the future experiment. In the following chapters, we performed a series of simulations to determine the physical properties of micelle nanostructures. With the force field parameters that were updated through DFT calculation, MD simulation measured physical quantities that experiment may not easily achieve. Particularly, computational methods were employed to examine the thermodynamics involved in the phase segregation among components in the micellar system for the study of its application.

2.2.1. Potentials of Mean Force Calculation via Steered Molecular Dynamics Simulation

One of thermodynamic properties to express the degree of phase segregation is the free energy change of placing one component in another. Steered molecular dynamics (SMD) simulation is capable of providing the potentials of mean force (PMF) that can be interpreted as the energy required to displace a specific atom or molecule along the designated path. Therefore, the obtained thermodynamic data can be linked to the nature of interaction between the displaced object and its surroundings.

The difference of the PMF between the initial and final coordinate is considered to be the estimated free energy difference as the calculation is performed as quasi-static:[20-29]

$$\left\langle e^{-\beta W} \right\rangle = e^{-\beta \Delta F} \tag{2}$$

Based on the Jarzynski's equality as shown in Equation 2 (β denotes the inverse temperature), the calculation of free energy difference (ΔF) can be done by the calculation of work done (W) through non-equilibrium processes, which is the displacement of molecule. In the SMD simulation, the external work done (W) is calculated by the pulling force and the pulling velocity that is interpreted into the displacement of molecule along with the reaction coordinate within the step size. The following equation expresses the external work done to pull the target molecule:

$$W = -kv\int_{0}^{t} dt' \left[x(t') - x_0 - vt'\right] \tag{3}$$

where *W, k, v, t, x(t),* and x_0 denote the external work done, the pulling force constant, the pulling speed, the time, the reaction coordinate, and the initial coordinate of molecule. In this study, the inputs for the SMD simulation were the force constant, the pulling speed,

and the reaction coordinate. In each step, the pulling force is calculated by multiplying the pulling force constant by the displacement of molecule that is dependent on the pulling speed and the step size. For the accuracy of calculation, the quasi-static condition must be acquired and maintained throughout the simulation.[26, 27] Demonstrated by Park and coworkers,[27] the significant strength of force constant and the effectively slow pulling speed allow maintaining the quasi-static condition.

For the robust calculation of the free energy difference, multiple sets of SMD simulation need to be performed independently with the same displacement conditions to obtain ensemble average of multiple sets of PMF data using the following equation:

$$PMF(r) = -RT \ln \left[\frac{1}{n} \sum_{i=1}^{n} \exp \left(\frac{-PMF_i(r)}{RT} \right) \right] \qquad (4)$$

where R, T, n, r, and $PMF(r)$ denote the ideal gas constant, the temperature, the number of trajectories, the displacement coordinate, and the potentials of mean force value. Through this Equation (4), the PMFs are averaged, which is introduced from the Jarzynski equality that is most frequently used in obtaining approximate free energy change over a given process along irreversible paths.

2.2.2. *Phase Segregation Analysis via Flory-Huggins Theory*

A micelle is an aggregate of amphiphilic materials that assemble themselves in an approximately spherical form in a selective solvent. Due to their amphipathic nature, the micellar structure contains both hydrophobic regions forming the core as well as hydrophilic regions protecting its inside from solvent phase. In the case of multicompartment micelle, more than two discrete regions can be arranged. As mentioned, each region can carry distinct features. For instance, in the study of nanoreactors, it is hypothesized that a specific region limits the permeation of reactant or product molecules

within the micellar structure.[30] There are two properties that govern the permeation: the permeability of materials and the miscibility of molecule in a permeate. Under the assumption that the polymer network in the micelle is flexible, the incorporation of molecules in the complex is recognized as a property directly linked to the permeation. Therefore, the Flory-Huggins (FH) interaction parameters (χ_{FH}) can be employed to evaluate the miscibility of reactants and products with each block, which is defined by the following equation:[29]

$$\chi_{FH} = \frac{V_{ref} \Delta H_{mix}}{RT} \qquad (5)$$

where V_{ref} is the molar volume of molecules in the mixture systems and ΔH_{mix} denotes the enthalpy of mixing, a measure of the molecular interaction. According to the original theory, the higher the χ_{FH} parameter is calculated from binary mixture, the stronger the phase segregation is between two components.[31-33] The detailed mathematical terms can be found in Chapter 5.

2.3. Dissipative Particle Dynamics Simulation Approach

Simulating a full micellar structure is desirable but prohibitively computationally expensive. For instance, the radius of a typical polymeric multicompartment micelle simulated in this study was experimentally determined to be in the range from 20 nm to 50 nm. A number of atoms required to construct the structure including water phase would be millions of atoms.

This is where the coarse-graining method become effective to simulate macromolecular structures. Coarse-grained models have been widely used for computational research for large scale simulations.[34-43] Mainly, for instance, many simulation studies for soft condensed matter physics and biomolecular materials encounter

a common problem with handling the large number of atoms in the simulation system.[43] The size and time scale of the mentioned materials are considered to be too large to handle via quantum or all atomic force-field molecular dynamics methods in spite of the advance of both computational hardware and software. Coarse grained simulation technique can provide an efficient means to simulate and investigate the properties of materials at the mesoscale level that both of the atomistic representation and the continuum theory cannot handle.

For these practical reason, we employed dissipative particle dynamics (DPD) simulation as a multiscale simulation. The scheme of DPD simulation is different from the conventional coarse-grained model even though the concept of coarse-graining is applied for both. For instance, most of coarse-grained force field parameters still include all the equations and parameters required to reproduce the potential energy as Equation 1. In addition, one of the common drawbacks from the use of coarse-grained force field is that there has been no coarse-grained force field that can be universally employed since a number and variety of atoms represented by pseudoatoms always vary. Since the coarse-grained force field parameters are obtained in practical way, even well-known coarse-grained force fields such as the MARTINI force field is limited to simulating specific materials.[34] On the other hand, the DPD simulation is based on the nature of phase segregation among components, which are parameterized using the Flory-Huggins theory. Therefore, since the simulation requires only non-bonded interaction parameters, the DPD simulation has been extensively employed to study various complex systems, such as the hydrodynamic behavior of complex fluids, the microphase separation of polymer mixtures, and the morphology and structure control of the multicompartment micelles from amphiphilic polymers.[44-46 47-50] The computation details are introduced in Chapter 6.

2.4. References

[1]   Adcock, S.A.;McCammon, J.A. *Chem. Rev.* **2006**, *106*, 1589.

[2]   Alder, B.J.;Wainwright, T.E. *J. Chem. Phys.* **1957**, *27*, 1208.

[3]   Rahman, A. *Phys. Rev.* **1964**, *136*, A405.

[4]   Duan, Y.;Kollman, P.A. *Science* **1998**, *282*, 740.

[5]   Jang, S.S.; Molinero, V.; Çağın, T.;Goddard, W.A. *J. Phys. Chem. B* **2004**, *108*, 3149.

[6]   Skoulidas, A.I. *J. Am. Chem. Soc.* **2004**, *126*, 1356.

[7]   Xin, J.; Liu, D.;Zhong, C. *J. Phys. Chem. B* **2007**, *111*, 13675.

[8]   Bruce, C.D.; Berkowitz, M.L.; Perera, L.;Forbes, M.D.E. *J. Phys. Chem. B* **2002**, *106*, 3788.

[9]   Storm, S.; Jakobtorweihen, S.;Smirnova, I. *J. Phys. Chem. B* **2014**, *118*, 3593.

[10]   Tang, X.; Koenig, P.H.;Larson, R.G. *J. Phys. Chem. B* **2014**, *118*, 3864.

[11]   Ingram, T.; Storm, S.; Kloss, L.; Mehling, T.; Jakobtorweihen, S.;Smirnova, I. *Langmuir* **2013**, *29*, 15.

[12]   Dechant, J. *Acta Polym.* **1988**, *39*, 150.

[13]   Lu, A.;O'Reilly, R.K. *Curr. Opin. Biotechnol.* **2013**, *24*, 639.

[14]   Chandrawati, R.; van Koeverden, M.P.; Lomas, H.;Caruso, F. *J. Phys. Chem. Lett* **2011**, *2*, 2639.

[15]   Monteiro, M.J. *Macromolecules* **2010**, *43*, 1159.

[16]   Liu, Y.; Wang, Y.; Wang, Y.; Lu, J.; Piñón, V.;Weck, M. *J. Am. Chem. Soc.* **2011**, *133*, 14260.

[17]   Sholl, D.S.;Steckel, J.A. *Density Functional Theory*; John Wiley & Sons, Inc., **2009**.

[18]   Allen, M.P. *Computational Soft Matter: From Synthetic Polymers to Proteins*; **2004**.

[19]   Mayo, S.L.; Olafson, B.D.;Goddard, W.A. *J. Phys. Chem.* **1990**, *94*, 8897.

[20]   Czaplewski, C.; Kalinowski, S.; Liwo, A.;Scheraga, H.A. *Mol. Phys.* **2005**, *103*, 3153.

[21]   Kim, H.; Goddard, W.A.; Jang, S.S.; Dichtel, W.R.; Heath, J.R.;Stoddart, J.F. *J. Phys. Chem. A* **2009**, *113*, 4.

[22]   Kumar, S.; Bouzida, D.; Swendsen, R.H.; Kollman, P.A.;Rosenberg, J.M. *J. Comput. Chem.* **1992**, *13*, 1011.

[23]   Patargias, G.; Martay, H.;Fischer, W.B. *J. Biomol. Struct. Dyn.* **2009**, *27*, 1.

[24]   Roux, B. *Comput. Phys. Commun.* **1995**, *91*, 275.

[25]   Sprik, M.;Ciccotti, G. *J. Chem. Phys.* **1998**, *109*, 7737.

[26]   Yu, T.; Lee, O.-S.;Schatz, G.C. *J. Phys. Chem. A* **2013**, *117*, 7453.

[27]   Park, S.; Araghi, F.; Tajkhorshid, E.;Schulten, K. *J. Chem. Phys.* **2003**, *119*, 3539.

[28]   Trzesniak, D.; Kunz, A.-P.E.;van Gunsteren, W.F. *ChemPhysChem* **2007**, *8*, 162.

[29]   Xu, Z.J.; Yang, X.N.;Yang, Z. *J. Phys. Chem. B* **2008**, *112*, 13802.

[30]   Chun, B.J.; Lu, J.; Weck, M.;Jang, S.S. *Phys. Chem. Chem. Phys.* **2015**

[31]   Flory, P.J. *J. Chem. Phys.* **1942**, *10*, 51.

[32]   Huggins, M.L. *J. Phys. Chem.* **1942**, *46*, 151.

[33]   Kasimova, A.O.; Pavan, G.M.; Danani, A.; Mondon, K.; Cristiani, A.; Scapozza, L.; Gurny, R.;Moller, M. *J. Phys. Chem. B* **2012**, *116*, 4338.

[34]   Marrink, S.J.; Risselada, H.J.; Yefimov, S.; Tieleman, D.P.;De Vries, A.H. *J. Phys. Chem. B* **2007**, *111*, 7812.

[35]   Bhargava, B.L.; Devane, R.; Klein, M.L.;Balasubramanian, S. *Soft Matter* **2007**, *3*,

[36]   Bond, P.J.; Holyoake, J.; Ivetac, A.; Khalid, S.;Sansom, M.S. *J. Struct. Bio.* **2007**, *157*,

[37]   Marrink, S.J.; De Vries, A.H.;Mark, A.E. *J. Phys. Chem. B* **2004**, *108*,

[38]   Marrink, S.J.; Risselada, J.;Mark, A.E. *Chem. Phys. Lipids* **2005**, *135*,

[39]   Monticelli, L.; Kandasamy, S.K.; Periole, X.; Larson, R.G.; Tieleman, D.P.;Marrink, S.-J. *J. Chem. Theory Comput.* **2008**, *4*,

[40]   Padding, J.;Briels, W. *J. Chem. Phys.* **2002**, *117*,

[41]   Rudd, R.E.;Broughton, J.Q. *Phys. Rev. B* **1998**, *58*,

[42]   Tozzini, V. *Curr. Opin. Struct. Biol.* **2005**, *15*,

[43]   Uttarwar, R.G.; Potoff, J.;Huang, Y. *Ind. Eng. Chem. Res.* **2013**, *52*, 73.

[44]   Groot, R.D. *J. Chem. Phys.* **2003**, *118*, 11265.

[45]   Hoogerbrugge, P.J.;Koelman, J.M.V.A. *Europhys. Lett.* **1992**, *19*, 155.

[46]   Koelman, J.;Hoogerbrugge, P.J. *Europhys. Lett.* **1993**, *21*, 363.

[47]   Yamamoto, S.; Maruyama, Y.;Hyodo, S.-a. *J. Chem. Phys.* **2002**, *116*, 5842.

[48]   Li, X.; Pivkin, I.V.; Liang, H.;Karniadakis, G.E. *Macromolecules* **2009**, *42*, 3195.

[49]   Soddemann, T.; Dünweg, B.;Kremer, K. *Phys. Rev. E* **2003**, *68*,

[50]   Chen, S.; Guo, C.; Hu, G.-H.; Liu, H.-Z.; Liang, X.-F.; Wang, J.; Ma, J.-H.;Zheng, L. *Colloid. Polym. Sci.* **2007**, *285*, 1543.

CHAPTER 3

ADSORPTION OF CARBOXYLATE ON CALCIUM CARBONATE $\left(10\bar{1}4\right)$ SURFACE:

MOLECULAR SIMULATION APPROACH*

3.1. Introduction

Wettability alteration of carbonate surface is defined as the change of the surface characteristics, especially, from hydrophilic surface to oleophilic surface through the adsorption of amphiphilic compounds onto the surface.[1] It has been understood that such wettability alteration of the oil reservoir due to the adsorption of amphiphilic molecules is problematic for the petroleum recovery process.[1, 2] Specifically, the wettability alteration of the carbonate surface deteriorates the water-flooding based petroleum recovery due to the small or negative capillary pressure within the oleophilic surface fractures, repelling water phase.[3] In order to develop better techniques to improve oil recovery, therefore, it is necessary to understand the fundamentals of the carboxylate adsorption onto the carbonate surface.[4-7]

Numerous experimental studies have been conducted to investigate wettability alteration of carbonate surfaces using various carboxylates.[1, 3, 6-9] To understand the adsorption equilibrium of carboxylates on carbonate surfaces, thermodynamic models based on Langmuir adsorption have been developed through previous studies.[1-3, 5-8, 10]

As the results of these efforts, the surface density of the carboxylate molecules adsorbed on the carbonate surface has been experimentally characterized, and the molecular structure of the adsorbate on the surface has been predicted through theoretical

study.[2, 11, 12] Thomas et al.[13], for instance, have suggested that the negatively charged carboxylate in the crude oil be strongly associated with the carbonate surface as shown in Figure 3.1, which actually impart the oleophilicity to the carbonate surface through the non-polar moiety of the carboxylate. There have been simulation studies characterizing the thermodynamic properties of the carboxylate adsorption on the carbonate adsorbent, as well.[10, 14-17] For example, Legens et al.[10] have performed the experiments of the benzoate adsorption on the calcium carbonate surface (calcite hereafter) to attain the area occupied by a single benzoate on the calcite and attempted to determine the adsorptive interaction energy using ab Initio method. In their study[10], however, only one benzoate molecule and four pairs of $CaCO_3$ were used, which seems to be too small for investigating the structures and thermodynamic properties of carboxylate adsorption on the calcite surface. Here, we investigate the adsorbed layer of carboxylates on the calcite $\left(10\bar{1}4\right)$ surface using molecular simulation (MD) method to characterize the molecular packing and adsorptive binding interaction of carboxylates.

Over the past decade, molecular simulation approaches such as MD simulation and Monte Carlo (MC) method have been employed to study the interaction of fatty acids with various materials such as proteins, graphite surface, water, oil, and so on[10, 14-17], which unveils the structural and thermodynamic details in the fatty acid layer. In this context, it should be noted that the adsorption of a carboxylate onto the calcite surface has not been thoroughly investigated at molecular level.
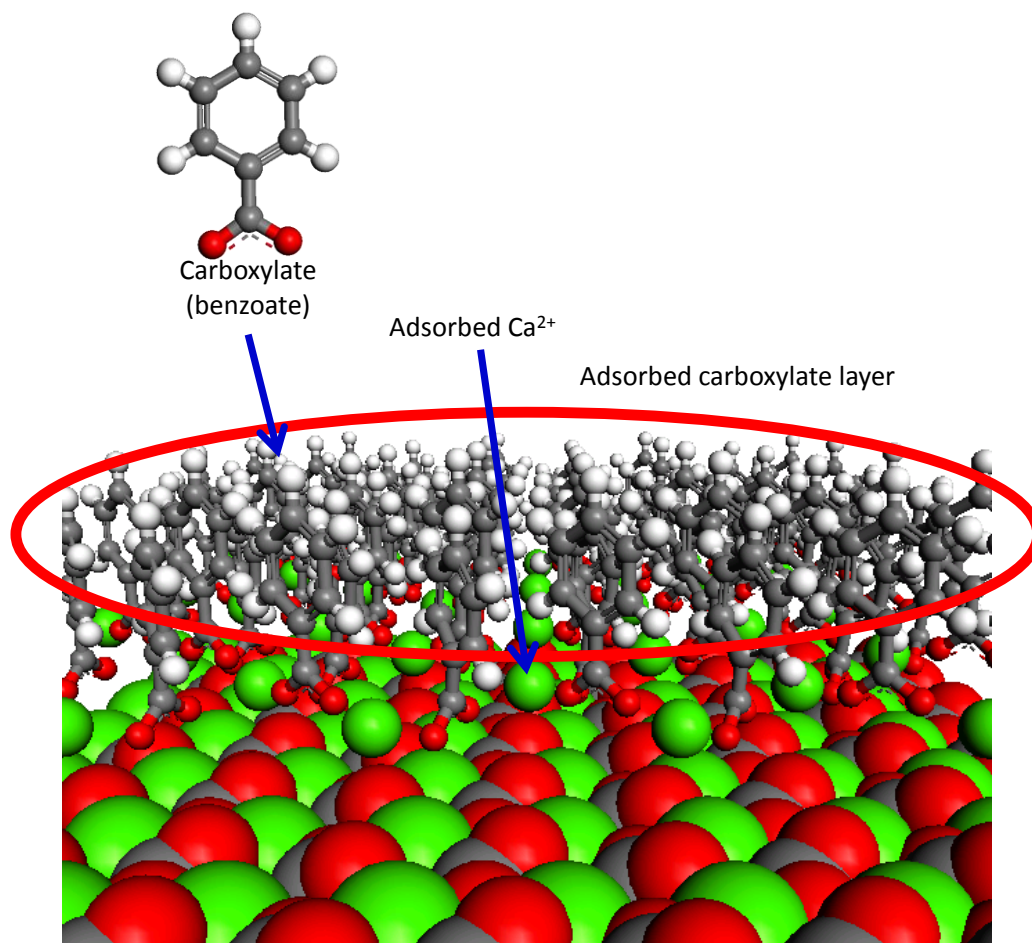
Figure 3.1. Carboxylate layer adsorbed on the carbonate surface. The benzoate is a model compound for the carboxylate dissolved in the crude oil. The green, red and grey and white colors denote calcium, oxygen, carbon, and hydrogen, respectively.

We report our simulation results for the adsorption of carboxylate on the calcite $(10\bar{1}4)$ surface using the molecular modeling methods based on DFT computation and MD simulation. We used two types of carboxylate: benzoate and stearate. The calcite surface model consists of Ca^{2+} and CO_3^{2-} as shown in Figure 3.2, indicating that the surface is originally hydrophilic due to its ionic character.[18, 19] We perform DFT calculation to obtain the adsorptive binding energy and molecular orientation of the carboxylate molecule on the calcite surface. These DFT results are used to develop a new set of force field (FF) parameters for MD simulations, which allows us to search the most probable adsorption

density of adsorbates and their molecular orientation in the layer on the chosen surface. The computational results are compared to the available experimental data for the validation of our simulation. Furthermore, the spontaneity of the carboxylate adsorption is demonstrated by calculating the potentials of mean force (PMF) via steered molecular dynamics (SMD) simulation.[20-28]

(a)   (b)
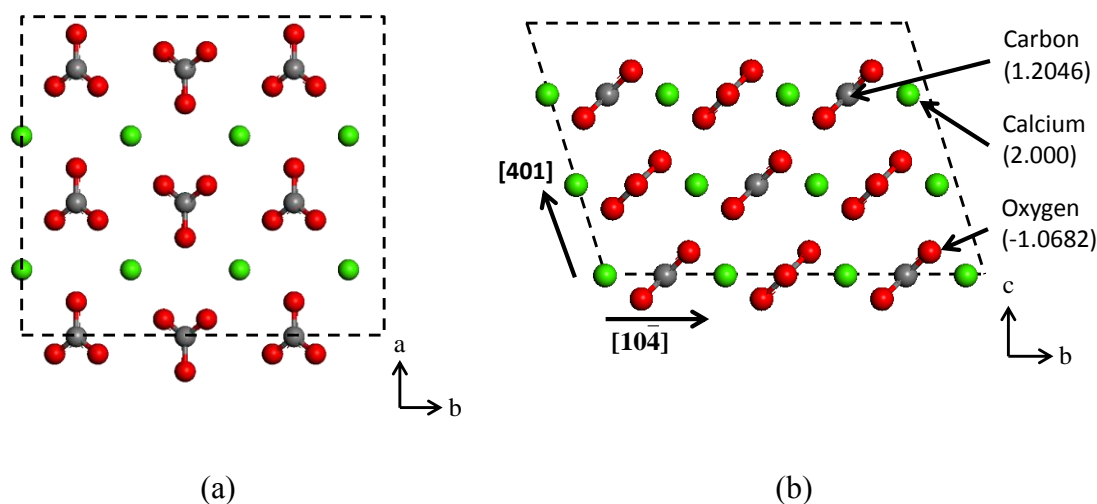
Figure 3.2. Atomistic model of calcite $(10\bar{1}4)$ surface: (a) top view and (b) side view. The calcite surface in $(10\bar{1}4)$ direction is known to have the lowest surface energy compared to other directions.[29] The values in the parentheses are the atomic charges,[19] indicating the ionic character of the atoms at calcite surface. The green, red and grey and white colors denote calcium, oxygen, carbon, and hydrogen, respectively.

3.2. Model and Simulation Methods

In order to investigate the probable structure of the carboxylate monolayer on the calcium carbonate (calcite) surface, the $(10\bar{1}4)$ surface was constructed as displayed in Figure 3.2 by cleaving the crystal structure[30] in a simulation box ($16.19 \times 19.96 \times 120\,\text{Å}^3$) as a 4-layer slab, containing 64 pairs of Ca^{2+} and CO_3^{2-}. The $(10\bar{1}4)$ surface has been known as the most stable surface with the lowest surface energy ($0.59\ \text{J/m}^2$) in vacuum from experimental[31, 32] and theoretical studies[33, 34].

This box size was specifically employed to calculate the binding energy and probable packing density using DFT and MD simulation, respectively, while a larger simulation box ($32.38 \times 39.96 \times 300$ Å³) was used to obtain the PMF.

Benzoate and stearate molecules were prepared as the adsorbates (Figure A1). Particularly, the united atom model[35-38] was employed for the non-polar alkyl tail (C16) of the stearate molecule to reduce the computational resources such as time and memory[39]. To simulate water and octane molecules, F3C model developed by Levitt and co-workers [40], and the united atom model developed by Siepmann et al.[35-38] were employed, respectively. This united atom model for alkanes describes one saturated carbon with a single pseudo-atom. The carboxylate molecules and the calcite surface were simulated using Dreiding FF[41] and MS-Q FF[18, 19, 42], respectively. The partial charges for atoms in carboxylate were calculated using Mulliken population analysis with B3LYP and 6-31G** through a quantum chemistry package, Jaguar[43].

Here, it should be noted that Dreiding FF and MS-Q FF use different non-bonded interaction functions: the former uses Lennard-Jones 12-6 function (Equation (1)) whereas the latter uses Exponential-6 function (Equation (2)).

$$U_{Lennard-Jones}(r) = D_0\left[\left(\frac{R_0}{r}\right)^{12} - 2\left(\frac{R_0}{r}\right)^{6}\right] \tag{1}$$

$$U_{Exp6}(r) = D_0\left\{\left[\left(\frac{6}{\eta - 6}\right)\exp\left(\eta\left(1 - \frac{r}{R_0}\right)\right)\right] - \left[\left(\frac{\eta}{\eta - 6}\right)\left(\frac{R_0}{r}\right)^{6}\right]\right\} \tag{2}$$

where D_0 is the energy well-depth in kcal/mol, R_0 and r are equilibrium distance and distance in Å, respectively, and η is a scaling factor. Although the intermolecular interactions in MD simulations are usually obtained from the standard geometric

combination rules[18, 19, 44], we developed a new DFT-based FF using Morse function (Equation (3)) in order to accurately describe the carboxylate-calcite interaction.

$$U_{Morse}(r) = D_0\left\{\exp\left[-\gamma\left(\frac{r}{R_0}-1\right)\right]-2\exp\left[-\frac{\gamma}{2}\left(\frac{r}{R_0}-1\right)\right]\right\} \qquad (3)$$

where D_0 is the energy well depth in kcal/mol, R_0 and r are equilibrium distance and distance in Å, respectively, and γ is a factor that controls the width of energy well. All the DFT calculations in this FF development were performed by the Generalized Gradient Approximation (GGA) spin-unrestricted Perdew-Burke-Ernzerhof (PBE) functional with DNP numerical basis set through DFT package, DMol3.[45, 46] The dispersion interaction correction was implemented using DFT-D3 method.[47]

Energy minimization was employed to search for the optimal coverage area per adsorbed molecule on the calcite surface. For the search of the most probable adsorption, various packing conditions of sodium dicarboxylate were explored to obtain the formation energy as a function of the number of molecules. The process was done in vacuum condition with the simulation box size of $16.19 \times 19.96 \times 120\,\text{Å}^3$. The energy minimization was performed using Cerius2 modeling package.[48]

In addition, to investigate the structure of carboxylate monolayer on calcite surface in equilibrium state, the canonical ensemble (NVT) MD simulations were performed at 300 K. The temperature was controlled using Nosé-Hoover thermostat[49, 50] with 0.1ps of relaxation time. The long-range electrostatic interactions were evaluated using the particle-particle particle-mesh (PPPM) method.[51] The equation of motion was integrated using the velocity-Verlet algorithm[52] with a time step of 1 fs. The periodic boundary conditions were imposed in all directions. The LAMMPS (large-scale atomic/molecular massively parallel

simulator)[53] code developed at Sandia National Laboratories was employed and modified to perform our MD simulation.

To assess the free energy change of carboxylate molecule as a function of adsorption states, we calculated the PMF using SMD simulation. The carboxylate molecule was slowly displaced to retain the quasi-static states.[25-28] For the robust calculation of the free energy difference, five sets of SMD simulation were performed independently with the same conditions to obtain an ensemble average of the multiple PMF results by the following:

$$PMF(r) = -RT \ln \left[\frac{1}{n} \sum_{i=1}^{n} \exp \left(\frac{-PMF_i(r)}{RT} \right) \right]$$ (4)

where *R, T, n and r* denote the gas constant, temperature, number of trajectories, and displacement coordinate. Through this Equation (4), the PMFs are averaged, which is introduced from the Jarzynski equality that is most frequently used in obtaining approximate free energy change over a given process along irreversible paths.[28]

In this study, a single benzoate molecule was slowly pulled at the rate of 10^{-5} Å/fs from the calcite surface up to the octane phase (a model for oil) in a multi-phase system (Figure A2) with the size of $32.38 \times 39.96 \times 300$ Å³. The thicknesses of the octane phase and the water phase are ~ 70 Å and ~ 60 Å, respectively. The number of water molecules and octane molecules are 2,608 and 323, respectively. The reason the multi-phase system was constructed was to describe the oil phase wetting the carboxylate monolayer under sea water. Figure A.2 shows a snapshot from one of the equilibrated multi-phase system simulations during 3.3 ns of NVT-MD simulations. During the NVT-MD simulation, the calcium atoms of the second layer from the bottom were restrained with 100 kcal/mol/Å.

3.3. Results and Discussion

3.3.1. Adsorptive Binding Energy

From the geometry optimization using DFT method with PBE, it is found that the benzoate molecule stands on calcite $(10\overline{1}4)$ surface as shown in Figure 3.3. The distance between the topmost calcium atoms of the calcite surface and the oxygen atoms of carboxylate group is 1.543Å. The adsorptive binding energy ($\Delta E_{binding}$) of one benzoate molecule is calculated as -29.45 kcal/mol using Equation (5) with DFT-D3 correction:

$$\Delta E_{binding} = E_{system} - (E_{surface} + E_{carboxylate}) \qquad (5)$$

where E_{system}, $E_{surface}$, and $E_{carboxylate}$ denote the energy of the total system, the surface and the carboxylate, respectively. In this work, to eliminate the influence of non-neutral condition, two anionic benzoate and a cationic calcium are placed on both sides of the calcite slab as clearly displayed in Figure 3.3b. By analyzing the energy components, it is suggested that this benzoate adsorption on the calcite surface is mainly driven by the electrostatic interaction between the carboxylate and the calcium cation.

(a)	(b)	(c)
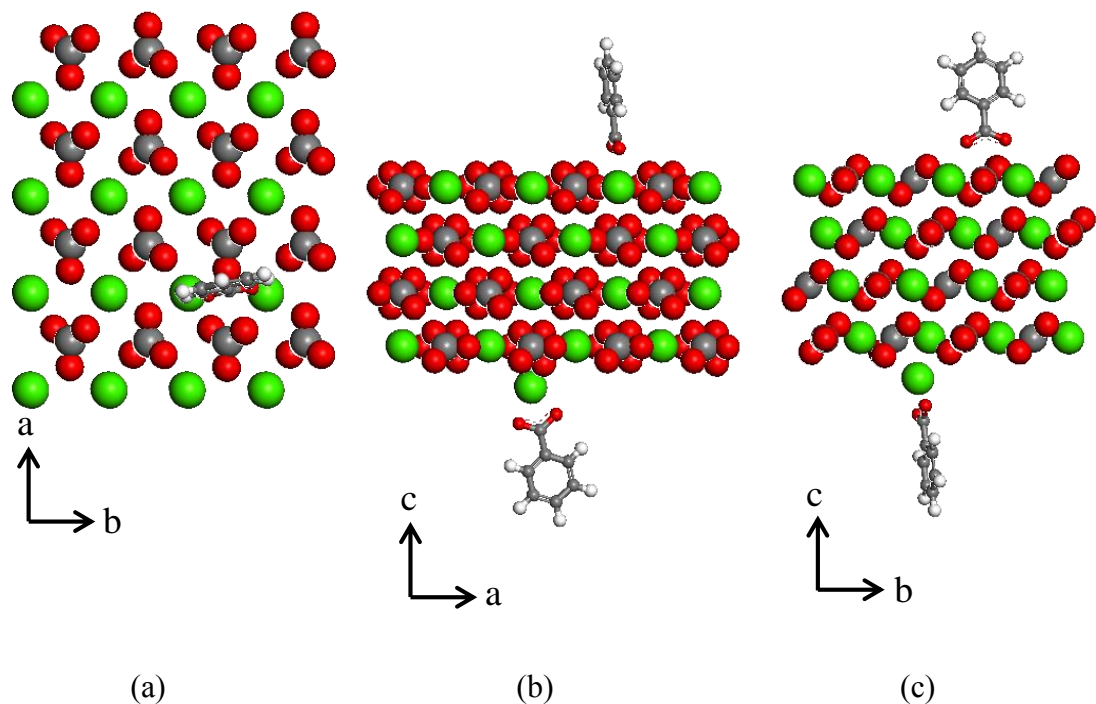
Figure 3.3. Geometry optimized structure using DFT with PBE: top view (a) and side views (top view; (b) and (c)). The green, red, grey and white color denote calcium, oxygen, carbon, and hydrogen, respectively.

3.3.2. Force Field Development

In order to simulate a multi-phase system (Figure A2) using MD simulation method, accurate force field (FF) needs to be used. Thus, we developed new FF parameters by employing Morse potential energy to describe the interaction between the carboxylate and calcite surface as summarized in Table 3.1, reproducing the aforementioned DFT results. In this study, it should be noted that we developed a new FF types (O_CO2 and C_CO2) for the carboxylate (COO⁻) in adsorbate molecule (Figure A3) while other atoms of benzoate use the generic Dreiding FF types (C_R and H_). While the interactions between the phenyl group in benzoate and calcite surface were calculated using the geometric mean value of the parameters in Exponential-6 energy function (Equation (2)), the carboxylate-calcite interaction was described by the new FF parameters. Figure 3.4 confirms that our

newly developed FF reproduces the distance-dependent binding energy obtained from DFT calculation.

Table 3.1. Newly developed force field parameters using Morse potential energy describing the interaction between carboxylates (benzoate or stearate) and calcite surface

Potential Function Type	Pairs		η	R_0	γ
	Calcite	Carboxylate			
Morse	Ca_RC	O_CO2	3.7694	0.3324	9.2202
	C_RC	O_CO2	3.8386	0.1710	26.8705
	O_RC	O_CO2	29.7294	0.0021	5.9359
	Ca_RC	C_CO2	4.2484	0.0100	0.7841
	C_RC	C_CO2	3.0553	0.0873	0.5014
	O_RC	C_CO2	3.5095	0.0600	0.6023
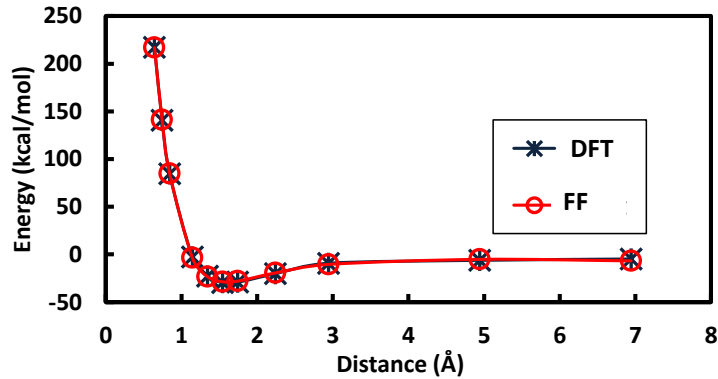
Figure 3.4. Change of adsorptive binding energy of benzoate molecule on calcite $(10\overline{1}4)$ surface as a function of distance between them. The binding energy calculated using DFT is successfully reproduced by the newly developed Morse potential force field parameters.

3.3.3. Determination of the Probable Packing Density

Through the energy minimization process with the newly developed FF, we characterize the probable packing of carboxylate molecules on calcite $(10\overline{1}4)$ surface. The optimal packing density is determined by the formation energy ($\Delta E_{formation}$) as a function

32

of the number of calcium dicarboxylate consisting of two carboxylate molecules and one calcium cation on calcite surface. This is because we need to keep the electroneutrality of system while we add carboxylate molecules on the calcite surface. $\Delta E_{formation}$ is defined in Equation (6):

$$\Delta E_{formation} = \frac{E_{system} - (E_{surface} + n_{calcium\ dicarboxylate} \times E_{calcium\ dicarboxylate})}{n_{calcium\ dicarboxylate}} \qquad (6)$$

where E_{system}, $E_{surface}$, $E_{calcium\ dicarboxylate}$ and denote the energy of the total system consisting of calcium dicarboxylates and calcite surface, the energy of calcite surface, and the energy of a calcium dicarboxylate, respectively, and $n_{calcium\ dicarboxylate}$ is the number of calcium dicarboxylate. We think that the most probable number of calcium dicarboxylate on the calcite surface is determined at which the most negative formation energy is obtained at 0 K. Therefore, the energy minimization was employed for the search.

As mentioned, the adsorption densities of the benzoate and stearate molecules on the calcite surface are investigated as a function of the number of calcium dicarboxylate on the surface in comparison with the experimental observation [2, 10-12]. Figure 3.5 presents the change of $\Delta E_{formation}$ as a function of the occupation area per molecule for the both cases. The comparison with experimental values at the most probable packing condition is summarized in Table 3.2.
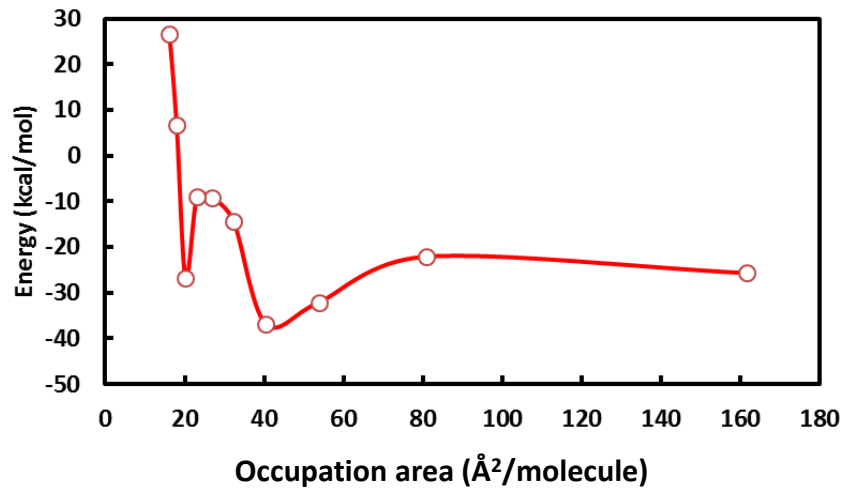
(a)
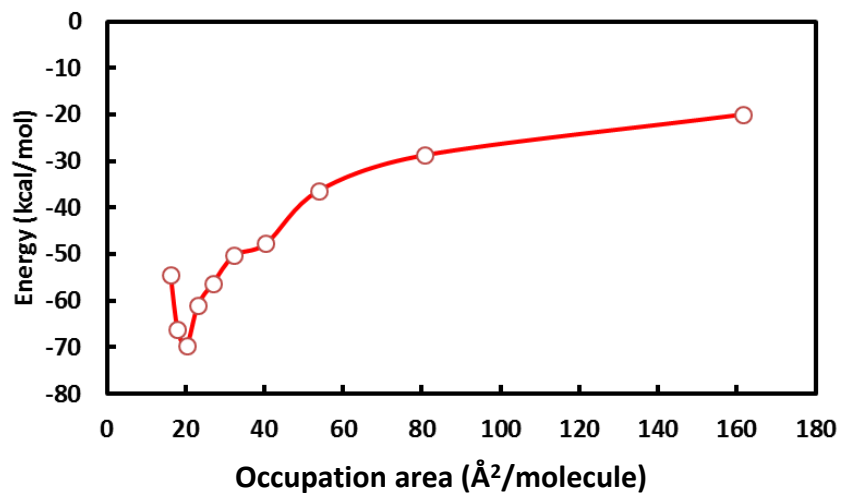
(b)

Figure 3.5. Change of formation energy as a function of the coverage area per molecule: (a) benzoate and (b) stearate. The red represents the results from the energy minimization.

Table 3.2. Molecular occupation area of carboxylate on calcite $(10\bar{1}4)$ surface

Carboxylate		Molecular occupation area (Å²/molecule)	Number of adsorbed molecule
Benzoate	Experiment [10]	41.93	7.71
		28.73	11.25
	Simulation	40.40	8
		20.20	16
Stearate	Experiment [2, 10, 11]	27.91	11.58
	Simulation	20.20	16

From the formation energy calculation of the benzoate adsorption, it is observed in Figure 3.5a that there are two probable occupation areas per molecule of the benzoate on the calcite surface: 40.40 Å²/molecule and 20.20 Å²/molecule. At those two probable occupation areas, the adsorbed carboxylate monolayers develop well-organized patterns as shown in Figures 3.6a and 3.6b, which is often observed in molecular layer on solid surface.[29, 54] Since the crystalline solid surfaces have ordered atomic arrangement, the dynamics and orientation of the adsorbate molecules are restricted as they absorb on the adsorbent, which is assumed to induce the decrease of the entropy during the formation of the patterned monolayer on solid surface.[29, 54] In particular, it is also found that the packing densities of our models are in good agreement with the experimental results reported by Legens et al.: the occupation area per molecule is reported to be 41.93 Å²/molecule and 28.73 Å²/molecule, respectively.[10]

Top view   Side view   Side view

(a)

Top view   Side view   Side view

(b)
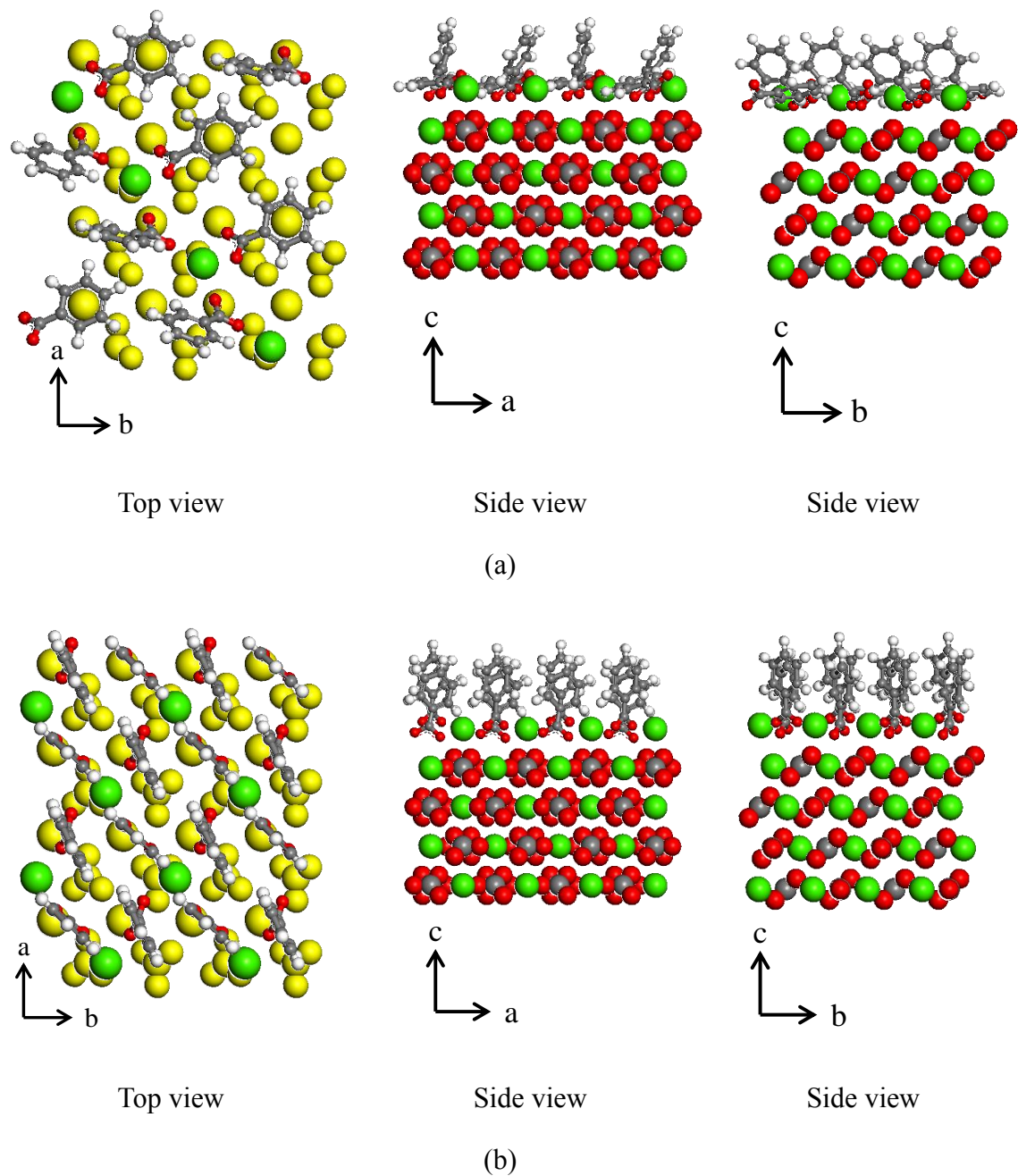
Figure 3.6. Structures of benzoate molecules adsorbed on calcite $(10\bar{1}4)$ surface for (a) the low density packing with the molecular coverage area of 40.40 Å²/molecule and (b) the high density packing with the molecular occupation area of 20.20 Å²/molecule. The green, red, grey and white color denote calcium, oxygen, carbon, and hydrogen, respectively. The yellow layer represents the first layer of calcite slab.

The adsorption of the stearate on the calcite surface is also investigated. The probable occupation area per molecule on calcite $(10\bar{1}4)$ surface is found at 20.20 Å²/molecule (Figure 3.7). The experimental value of the occupation area per molecule at 298K was reported as 27.91 Å²/molecule.[2, 10, 11] While the case of the benzoate adsorption shows two probable occupation areas, a single occupation area is observed from the results of the stearate case. The major difference between the stearate adsorption and the benzoate adsorption seems to be attributed to the hydrocarbon in the molecular structure. Due to the long alkyl tail in stearate, 1) the molecular interaction between 17-carbon alkyl tails is stabilized in densely packed structure and 2) the lying-down conformation as seen in Figure 3.6a for benzoate does not develop an ordered pattern for stearate with a stable formation energy.

To quantitatively analyze the conformation of carboxylate molecules on the calcite surface, the tilt angles of hydrocarbon part from the normal vector of the surface are measured as shown in Figure A4. It is found that the benzoate monolayer at 20.20 Å²/molecule (Figure 3.6b) holds the vertically standing conformation on the calcite surface with the tilt angle of 8.1±4.4 degree, and likewise, the tilt angle of 17-carbon alkyl tail of stearate molecule is measured as 14.0±2.9 degree from the probable adsorption density, whose agreement with the experimental report[11, 55] infers the validity of our simulation approach.

| Top view | Side view | Side view |
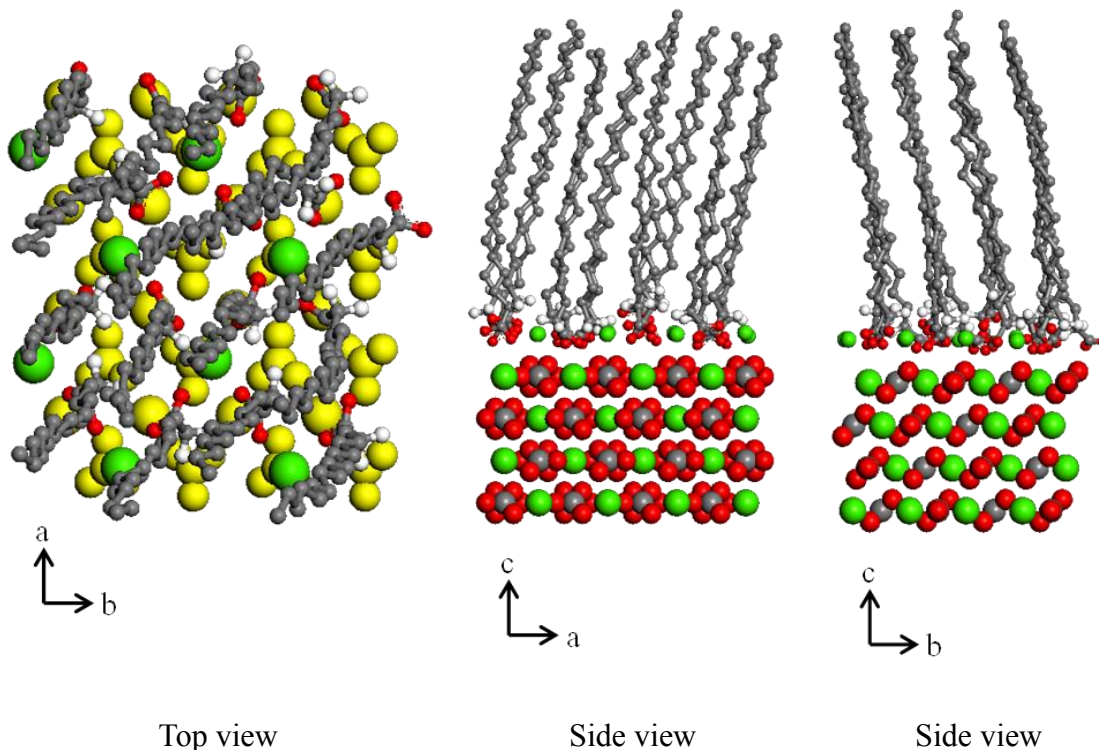
Figure 3.7. Structure of stearate molecules adsorbed on calcite $(10\bar{1}4)$ surface with the molecular occupation area of 20.20 Å²/molecule. The green, red, grey and white color denote calcium, oxygen, carbon, and hydrogen, respectively. The yellow layer represents the first layer of calcite surface.

In this study, it is noted that both benzoate and stearate commonly exhibit the perpendicularly standing molecular conformation on the calcite surface with a high molecular packing at the molecular occupation area of 20.20 Å²/molecule. The calculation results suggest that such similar level of the area occupied by benzoate and stearate indicates that the structure of the adsorbed molecules is predominantly determined by the strong carboxylate-calcium interaction on the calcite surface rather than by the interaction among the hydrophobic hydrocarbons. The distinct difference between benzoate and stearate is that the benzoate can have a low stable packing density (Figure 3.6a) with the molecular occupation area of 40.40 Å²/molecule where the stearate does not form a stable packing at such occupation area. From Figure 3.6a showing that half of the benzoate

molecules are lying on the surface, it is inferred that the π electrons of phenyl group of benzoate has a favorable interaction with the calcite surface, especially the calcium cation, which is not the case for stearate.

3.3.4. Potentials of Mean Force for Molecular Desorption

The free energy change during molecular desorption process is calculated using potential of mean force (PMF) via Steered Molecular Dynamics (SMD) simulation. Figure 3.8 presents the process of desorption in which we observe a calcium cation and another benzoate are dragged up together with the benzoate pulled by SMD simulation (Figures 3.8b and 3.8c), which is repeatedly observed through five independent SMD simulations. We believe that this is due to the strong electrostatic attraction of those two carboxylate groups with the attached calcium cation. This result is consistent with the strong binding energy between calcium atom and carboxylate (-42.72 kcal/mol in octane phase calculated using B3LYP and 6-31G** (LACVP for calcium) with Poisson-Boltzmann method[54]). Therefore, it is presumed from our simulations that the desorption of benzoate molecule from the surface would take place as an entire calcium dibenzoate.

Another point we stress is that such desorption would have multiple energy barriers during the process as shown in Figure 3.9. It is found that the first energy barrier of ~67 kcal/mol should be overcome for the detachment of the benzoate molecule (green colored in Figures 3.8b and 3.8c). In addition, the second energy barrier is calculated to be ~90 kcal/mol based on the difference between the first local minimum (the displacement distance of 6 Å) and the second peak. This measured energy difference is the amount of energy to completely free the whole calcium dibenzoate from the carboxylate monolayer.
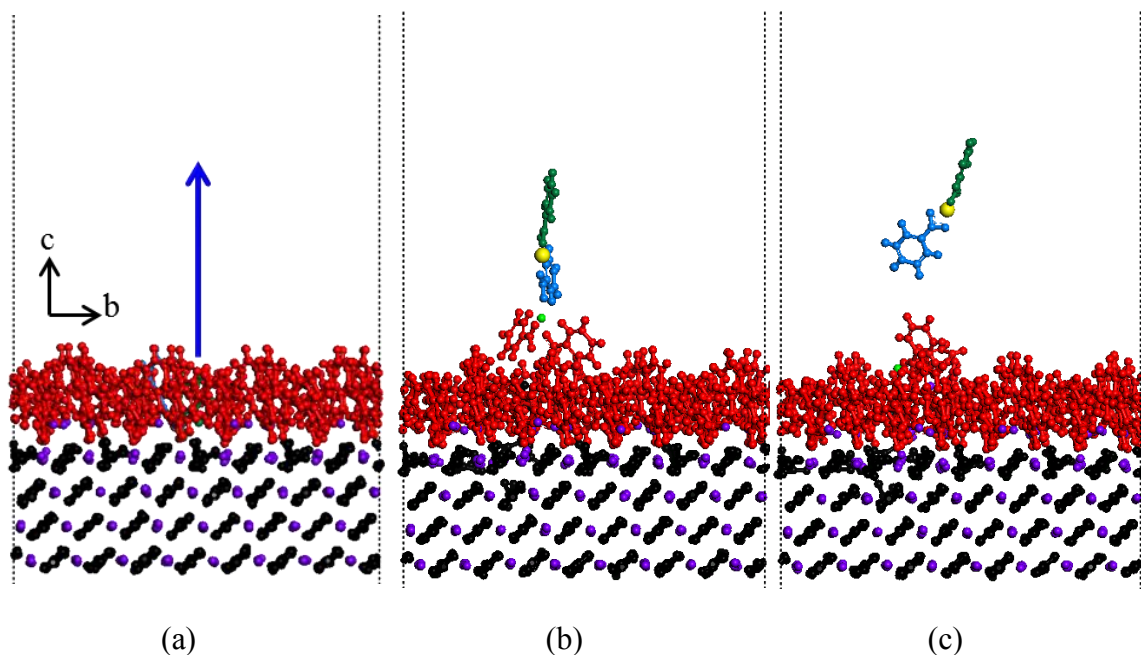
Figure 3.8. Structures sampled during steered molecular dynamics simulation: (a) t = 0 ps; (b) t = 1.75 ns, it is observed that the pulled calcium dibenzoate has an interaction with other benzoate molecules on the calcite surface; (c) is at 2 ns of the simulation. The black, purple, and red colors denote the carbonate group of calcite, the calcium, the benzoates of the monolayer, respectively. The green and blue color denote the pulled benzoate and its paired benzoate, respectively. The blue colored arrow indicates the direction of pulling benzoate during the Steered MD simulation.

In terms of the desorption, the first energy barrier observed within the distance interval from 0 to 5 Å is due to the detachment of calcium cation from the calcite surface and the subsequent second energy barrier is measured when the calcium dibenzoate is completely detached out of the molecular monolayer on the calcite surface. In other words, the observed double energy barrier process is an evidence that the adsorption and desorption take place as a calcium dibenzoate rather than a calcium benzoate.

Overall, the free energy required for the desorption of calcium dibenzoate is calculated to be 148 kcal/mole. This value that is higher than the binding energy of a single benzoate indicates that the adsorbed carboxylates are further stabilized due to the presence of well-packed neighboring molecules. Possible pi stacking occurs among the neighboring benzene rings and thermodynamically strengthens the adsorbed monolayer. Conclusively,

the increase of the PMF along the moving path in Figure 3.9 indicates that the desorption process is very undesirable, meaning that the adsorption of carboxylate molecules on calcite surface and the subsequent formation of monolayer take place spontaneously with the significant free energy stabilization by 148 kcal/mol.
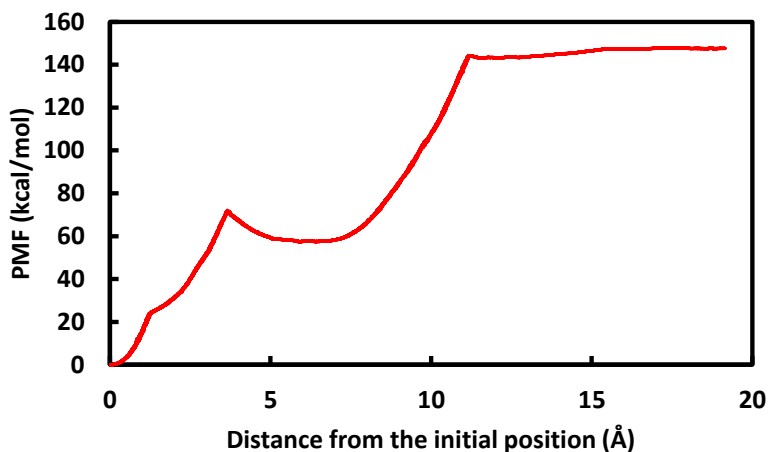
Figure 3.9. Change of potential of mean force along with the reaction coordinate. The origin represents the initial position of the benzoate molecule on the calcite surface.

3.4. Summary

The adsorption of carboxylate molecules such as benzoate and stearate on the calcite $(10\bar{1}4)$ surface was investigated using molecular simulation approach. The simulated structures were validated by comparing with the experimental observation. The adsorption energy for a single benzoate molecule on the carbonate surface was calculated as -29.25 kcal/mol using the DFT calculation with DFT-D3 correction. The results from DFT calculation were used to develop a new set of force field parameters using Morse potential energy function. The newly developed FF reproduced the adsorptive interaction of carboxylate with the calcite surface.

Performing energy minimization using the new FF, it was found that the adsorption of benzoate can have multiple probable packing densities on the calcite surface, which

agrees with the experimental work by Legens and coworkers.[10] Through assessing the structures of carboxylate molecules in the monolayer, it seemed that the benzoate has two probable packing densities at the coverage area per molecule of 40.40 $Å^2$/molecule and 20.20 $Å^2$/molecule, while the stearate exhibits a single probable packing at 20.20 $Å^2$/molecule.

Since the carboxylate adsorption on calcite surface was mainly driven by the electrostatic interaction between carboxylate and calcite surface, the molecular packing was identical at the high packing condition (20.20 $Å^2$/molecule) at which the averaged tilt angles from the surface normal vector of the calcite $(10\bar{1}4)$ surface were simulated as 8.1±4.4 degree and 14.0±2.9 degree for benzoate and stearate, respectively.

From our PMF calculations, it was found that the desorption of carboxylate occurs as a form of calcium dicarboxylate due to strong electrostatic attraction between   two carboxylates and calcium cation, which showed two distinct energy barriers in the PMF curve. We thought that the first energy barrier corresponds to the energy (~67 kcal/mol) required to break the binding of calcium cation from the calcite surface while the second energy barrier specifies the energy (~90 kcal/mol) required to detach the binding of the second carboxylate. Therefore, the total free energy difference of the carboxylate desorption is estimated to be 148 kcal/mol, from which it was inferred that the molecular interaction among carboxylate molecules in the well-packed calcium dicarboxylate monolayer lower the formation energy compared to the binding energy of single carboxylate molecule on calcite.

3.5. References

[1]   Austad, T.;Standnes, D.C. *J. Pet. Sci. Eng.* **2003**, *39*, 363.

[2]   Alipour Tabrizy, V.; Denoyel, R.;Hamouda, A.A. *Colloids Surf. Physicochem. Eng. Aspects* **2011**, *384*, 98.

[3]   Puntervold, T.; Strand, S.;Austad, T. *Energy Fuels* **2007**, *21*, 1606.

[4]   Schramm, L.L. *Surfactants: fundamentals and applications in the petroleum industry* Cambridge University Press, **2000**.

[5]   Austad, T.; Matre, B.; Milter, J.; Sevareid, A.;Oyno, L. *Colloids Surf. Physicochem. Eng. Aspects* **1998**, *137*, 117.

[6]   Standnes, D.C.;Austad, T. *J. Pet. Sci. Eng.* **2000**, *28*, 123.

[7]   Standnes, D.C.;Austad, T. *Colloids Surf. Physicochem. Eng. Aspects* **2003**, *216*, 243.

[8]   Osman, M.A.;Suter, U.W. *Chem. Mater.* **2002**, *14*, 4408.

[9]   Standnes, D.C.;Austad, T. *J. Pet. Sci. Eng.* **2000**, *28*, 111.

[10]   Christelle Legens, H.T., Louis Cuiec, Frederic Villieras,Thierry Palermo *SPE J.* **1999**, *4*, 328.

[11]   Gomari, K.A.R.; Hamouda, A.A.;Denoyel, R. *Colloids Surf. Physicochem. Eng. Aspects* **2006**, *287*, 29.

[12]   Rezaei Gomari, K.A.; Denoyel, R.;Hamouda, A.A. *J. Colloid Interface Sci.* **2006**, *297*, 470.

[13]   Thomas, M.M.; Clouse, J.A.;Longo, J.M. *Chem. Geol.* **1993**, *109*, 201.

[14]   Wojciechowski, K.;Buffle, J. *Biosens. Bioelectron.* **2004**, *20*, 1051.

[15]   Levin, L.B.-A.; Ganoth, A.; Amram, S.; Nachliel, E.; Gutman, M.;Tsfadia, Y. *J. Mol. Model.* **2010**, *16*, 929.

[16]   Friedman, R.; Nachliel, E.;Gutman, M. *Biophys. J.* **2006**, *90*, 1535.

[17]   Hibino, M.; Sumi, A.;Hatta, I. *Thin Solid Films* **1996**, *282*, 594.

[18]   Hwang, S.; Blanco, M.; Demiralp, E.; Cagin, T.;Goddard, W.A. *J. Phys. Chem. B* **2001**, *105*, 4122.

[19]   Hwang, S.; Blanco, M.;Goddard, W.A. *J. Phys. Chem. B* **2001**, *105*, 10746.

[20]   Czaplewski, C.; Kalinowski, S.; Liwo, A.;Scheraga, H.A. *Mol. Phys.* **2005**, *103*, 3153.

[21]   Kim, H.; Goddard, W.A.; Jang, S.S.; Dichtel, W.R.; Heath, J.R.;Stoddart, J.F. *J. Phys. Chem. A* **2009**, *113*, 2136.

[22]   Kumar, S.; Bouzida, D.; Swendsen, R.H.; Kollman, P.A.;Rosenberg, J.M. *J. Comput. Chem.* **1992**, *13*, 1011.

[23]   Patargias, G.; Martay, H.;Fischer, W.B. *J. Biomol. Struct. Dyn.* **2009**, *27*, 1.

[24]   Roux, B. *Comput. Phys. Commun.* **1995**, *91*, 275.

[25]   Trzesniak, D.; Kunz, A.-P.E.;van Gunsteren, W.F. *Chemphyschem : a European journal of chemical physics and physical chemistry* **2007**, *8*, 162.

[26]   Xu, Z.J.; Yang, X.N.;Yang, Z. *J. Phys. Chem. B* **2008**, *112*, 13802.

[27]   Yu, T.; Lee, O.-S.;Schatz, G.C. *J. Phys. Chem. A* **2013**, *117*, 7453.

[28]   Park, S.; Araghi, F.; Tajkhorshid, E.;Schulten, K. *J. Chem. Phys.* **2003**, *119*, 3559.

[29]   Wright, K.; Cygan, R.T.;Slater, B. *Structure of the (1014) surfaces of calcite, dolomite and magnesite under wet and dry conditions*; Royal Society of Chemistry, **2001**.

[30]   Effenberger, H.; Mereiter, K.;Zemann, J. *Z. Kristallogr. - New Cryst. Struct.* **1981**, *156*, 233.

[31]   Heywood, B.R.;Mann, S. *Chem. Mater.* **1994**, *6*, 311.

[32]   Didymus, J.M.; Oliver, P.; Mann, S.; Devries, A.L.; Hauschka, P.V.;Westbroek, P. *J. Chem. Soc., Faraday Trans.* **1993**, *89*, 2891.

[33]   Kenway, P.R.; Oliver, P.M.; Parker, S.C.; Sayle, D.C.; Sayle, T.X.T.;Titiloye, J.O. *Mol. Simul.* **1992**, *9*,

[34]   Parker, S.C.; Kelsey, E.T.; Oliver, P.M.;Titiloye, J.O. *Faraday Discuss.* **1993**, *95*, 75.

[35]   Siepmann, J.I.; Karaborni, S.;Smit, B. *Nature* **1993**, *365*, 330.

[36]   Smit, B.; Karaborni, S.;Siepmann, J.I. *J. Chem. Phys.* **1995**, *102*, 2126.

[37]   Smit, B. *Phys. Rev. A* **1988**, *37*, 3431.

[38]   Smit, B.; Hilbers, P.A.J.; Esselink, K.; Rupert, L.A.M.; Vanos, N.M.;Schlijper, A.G. *J. Phys. Chem.* **1991**, *95*, 6361.

[39]   Jang, S.S.; Lin, S.-T.; Maiti, P.K.; Blanco, M.; Goddard, W.A.; Shuler, P.;Tang, Y. *J. Phys. Chem. B* **2004**, *108*, 12130.

[40]   Levitt, M.; Hirshberg, M.; Sharon, R.; Laidig, K.E.;Daggett, V. *J. Phys. Chem. B* **1997**, *101*, 5051.

[41]   Mayo, S.L.; Olafson, B.D.;Goddard, W.A. *J. Phys. Chem.* **1990**, *94*, 8897.

[42]   Rappe, A.K.;Goddard, W.A. *J. Phys. Chem.* **1991**, *95*, 3358.

[43]   *Jaguar*. 2008, Schrödinger, LLC: New York, NY.

[44]   Jang, S.S.;Goddard, W.A. *J. Phys. Chem. B* **2006**, *110*, 7992.

[45]   Delley, B. *J. Chem. Phys.* **1990**, *92*, 508.

[46]   Delley, B. *J. Chem. Phys.* **2000**, *113*, 7756.

[47]   Grimme, S.; Ehrlich, S.;Goerigk, L. *J. Comput. Chem.* **2011**, *32*, 1456.

[48]   Chun, B.J.; Lee, S.G.; Choi, J.I.;Jang, S.S. *Colloids Surf. Physicochem. Eng. Aspects* **2015**, *474*, 9.

[49]   Nose, S. *Mol. Phys.* **1986**, *57*, 187.

[50]   Hoover, W.G. *Phys. Rev. A* **1985**, *31*, 1695.

[51]   Hockney, R.W.;Eastwood, J.W. *Computer simulation using particles*; McGraw-Hill International Book Co., **1981**.

[52]   Swope, W.C.; Andersen, H.C.; Berens, P.H.;Wilson, K.R. *J. Chem. Phys.* **1982**, *76*, 637.

[53]   Plimpton, S.J. *J. Comp. Phys.* **1995**, *117*, 1.

[54]   Tannor, D.J.; Marten, B.; Murphy, R.; Friesner, R.A.; Sitkoff, D.; Nicholls, A.; Ringnalda, M.; Goddard, W.A.;Honig, B. *J. Am. Chem. Soc.* **1994**, *116*, 11875.

[55]   Fenter, P.;Sturchio, N.C. *Geochim. Cosmochim. Acta* **1999**, *63*, 3145.

CHAPTER 4

MOLECULAR DYNAMICS SIMULATION STUDY OF SODIUM DODECYL SULFATE MICELLE: WATER PENETRATION AND SODIUM DODECYL SULFATE DISSOCIATION*

4.1. Introduction

Research on micelles has been mainly focused on the thermodynamic and structural properties at various conditions of micellization such as concentration and temperature.[1-7] Recently, work in this area has been expanded to synthesize various types of amphiphilic molecules in order to harness the properties of micelle for various applications utilizing the compartmentalization capability such as drug delivery[8-12], nano-reactors[13-16] and so on. For instance, O'Reilly and coworkers have successfully demonstrated that the polymeric micelles can have the high catalytic activity and specificity as frequently observed in enzymes of natural systems.[14-16] Following the compartmentalization in micelles, another point of interest is the transport of small molecules through the micelle, which is relevant for their storage and release in such compartments. In this context, it should be noted that a fundamental understanding of the relationship between the micelle structure and the small molecular transport through micelles is essential information for achieving micelle design for desirable performance for various applications.

In this study, we investigated the micellar structure and corresponding transport property in sodium dodecyl sulfate (SDS) micelle using molecular dynamics (MD) simulation method. Please note that SDS micelle has been selected as a model system because it is the most intensively-characterized micelle through experimental analysis[17-32] and simulation methods[33-44]. In experimental approaches, various techniques such as light

---

scattering[18-21], fluorescence[23, 24], SAXS[17, 30] and SANS[25, 26] have been used to characterize the size, shape, aggregation and charge of the SDS micelle at various conditions for concentration and temperature. Here it is noted that, despite great development in such experimental analysis, it is still challenging to attain molecular-level information of the internal structure of the SDS micelle experimentally.

In this context, the molecular dynamics (MD) simulation methods have been extensively used to provide such detailed structural information on the micelle in general[45-65] as well as the SDS micelle[33-35, 37-44, 66]. In 1990, Shelley and coworkers[33] reported the first large scale 182-picosecond MD simulation study on 42 monomer SDS micelle, in which they found that ~12 % of the sodium ions form contact ion pairs with the micelle. In 1995, Mackerell[34] simulated SDS micelle comprised of 60 SDS molecules for 120 ps, reporting radial density profile, conformations of SDS monomer, and the motion of micelle in addition to SDS monomers using CHARMM[67] force field and TIP3P[68] water model. Bruce et al.[35, 36] also performed 5-nanosecond all-atom MD simulations using AMBER[69] force field, reporting detailed structural analyses such as radius of gyration, micellar size, carbon atom distribution, eccentricity, accessible surface area and so on. Yoshii and coworkers investigated the free energy of the SDS micelle as a function of the number of monomers using thermodynamic integration method and MD simulation to analyze the free energy of the micelle as a function of the monomer[37]. They presented that the free energy is minimized at 57 monomers, which comparable to the experimental aggregation numbers (55-75)[22, 23, 26, 27, 29]. Jalili and Akhavan[41] used a coarse-grained MD simulation method with MARTINI force field[70] to investigate the structure of SDS micelle, showing that the coarse-grained MD simulation can describe the SDS micelle accurately. From the recent study done by Tang et al. performing large-scale MD simulation using various FFs for SDS micelle, it was reported that the united-atom FF for sulfate head group does not capture realistic rod-like or cylindrical micelles at high aggregation number (>300) while there is no significant difference at low aggregation numbers (60 or 100).

In this study, we revisited SDS micelle to elucidate the internal and surface structure, particularly focusing on the packing of alkyl tails in the micelle by analyzing the conformation of the individual SDS molecules, the internal free volume, and surface occupation of sulfate groups and alkyl tails. Although the SDS micellar structures such as micelle size, monomer conformation have been characterized in previous studies[33, 34, 38], please note that those results were attained from relatively short MD simulations running for a few nanosecond. Therefore, it is still desirable to thoroughly scrutinize the various aspects of the micellar structure based on the long production run of 20 ns, which will provide more reliable characterization of the micellar structure. In addition, the structural integrity and molecular transport in the micelle is evaluated by calculating the potential of mean force (PMF) via the steered molecular dynamics (SMD) simulation method, which is the free energy change of the system as a function of the molecular displacement along the designated path. We think that the present study can provide computational procedure to investigate the relationship of the molecular transport through micelle with the micellar structure.

4.2. Models and Simulation Methods

The SDS molecules were simulated using a full-atomistic model (Figure 4.1) with Dreiding FF.[71] The atomic partial charges for SDS were calculated using Mulliken population[72] with B3LYP/6-31G** through a quantum chemistry package, Jaguar[73]. The detailed values of the partial charges for the SDS molecule are summarized in Table 4.1.
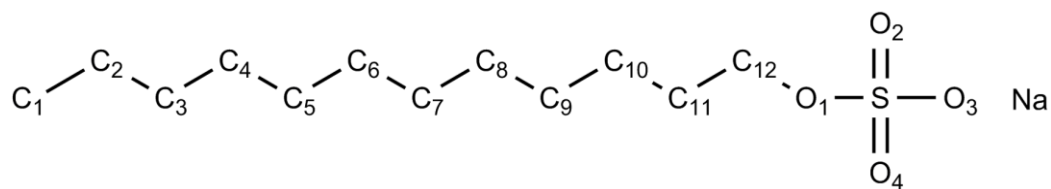
Figure 4.1. Chemical structure of sodium dodecyl sulfate surfactant. C_1 has three explicit hydrogens and the rest of the carbons from C_2 through C_{12} have two explicit hydrogens although those hydrogens are omitted.

Table 4.1. Atomic partial charges for the surfactant molecule. The carbon number and oxygen number correspond to the model in Figure 4.1.

Hydrocarbon						
Carbon Number	**1**	**2**	**3**	**4**	**5**	**6**
C	-0.3165	-0.1720	-0.1641	-0.1726	-0.1727	-0.1724
H₁	0.0994	0.0889	0.0849	0.0849	0.0845	0.0878
H₂	0.0931	0.0900	0.0836	0.0869	0.0823	0.0838
H₃	0.0986					
Carbon Number	**7**	**8**	**9**	**10**	**11**	**12**
C	-0.1716	-0.1716	-0.1706	-0.1664	-0.1948	0.0879
H₁	0.0828	0.0816	0.0683	0.0759	0.0864	0.0812
H₂	0.0784	0.0921	0.0803	0.0129	0.0561	0.0821
Sodium Sulfate						
S	1.2073	**O₁**	-0.5796	**O₂**	-0.6160	
O₃	-0.6137	**O₄**	-0.5810	**Na**	1.000	

For this simulation study, the aggregation number is set as 60 that has been found in experiments[22, 23, 26, 27, 29], and used in simulation studies[34-38, 41, 44]. To build a SDS micelle in water phase, first, we arranged 60 lines radially to occupy the space equally (Figure 4.2a), and subsequently replace them by 60 SDS molecules (Figure 4.2b) in simulation box ($91.4 \times 91.4 \times 91.4 \text{ Å}^3$). This SDS micelle was solvated by 24,650 water molecules, so that the total number of atoms in the system was 76,533. Water molecules were described by F3C model.[74] Since the effect of the amount of water content in the system was proven to be insignificant[44], the box size was determined to be large enough to avoid the influence of neighboring self-image through the periodic boundary conditions. The temperature was maintained at 300K using Nosé-Hoover thermostat[75, 76]. The particle-particle particle-mesh (PPPM) method was used for the long-range electrostatic interaction calculation.[77] The

equation of motion was integrated using velocity-Verlet algorithm with a time step of 1 fs.[78] A periodic boundary condition was imposed in all directions. The LAMMPS (large-scale atomic/molecular massively parallel simulator) code developed by Sandia National Laboratories was employed to perform MD simulations.[79] To equilibrate the system, first, we ran annealing simulation to relax the system out of the local minima. Then, we ran 18 ns of NVT MD simulation to reach the equilibrium state. The actual data collection for statistical analysis, we ran another NPT MD simulation at 1 atm for 20 ns. To verify the equilibration of the system, the radius of gyration (R_g) of micelle was calculated using the following definition[80]:

$$R_g^2 = \sum_i \frac{m_i (\mathbf{r}_i - \mathbf{R}_c)^2}{M} \qquad (1)$$

where m_i and $\mathbf{r}_i$ denote the mass and position of the i-th atom, respectively, and $\mathbf{R}_c$ and M denote the position of the center of mass of the micelle and the total mass of the micelle, respectively. The plot of R_g over simulation time (Figure 4.3) confirms that the micelle is equilibrated during 20 ns NPT MD simulation.
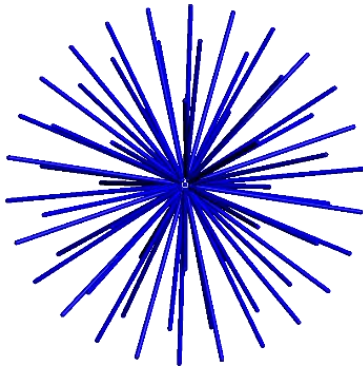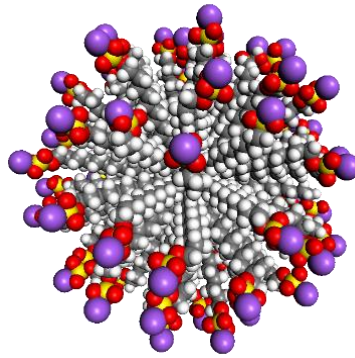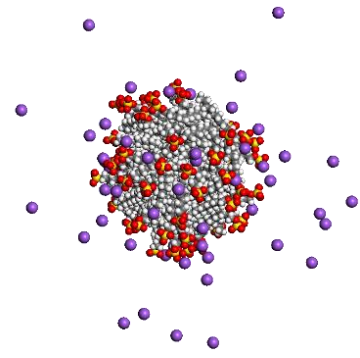
(a) (b) (c)

Figure 4.2. Scheme of constructing a 60 SDS micelle structure. (a) shows the skeleton of 60 SDS molecules equally occupying the space, (b) exhibits the structure of prefixed micelle whose monomers are placed on the blue rods, and (c) is the micelle structure after NPT MD simulation. The white, red, yellow, gray, and purple colored beads denote hydrogen, oxygen, sulfur, carbon, and sodium atoms, respectively. Water molecules in (b) and (c) are omitted.
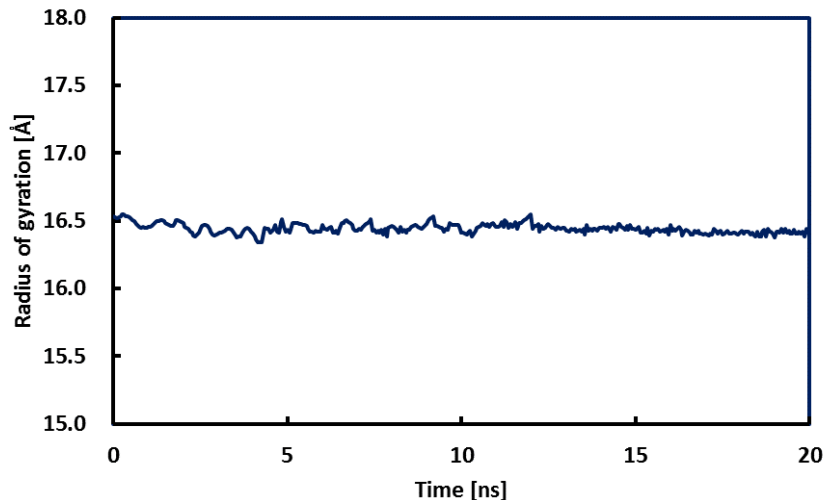
Figure 4.3. Change in radius of gyration of SDS micelle over 20 ns of NPT MD simulation.

To investigate the molecular transport through the SDS micelle, SMD simulation was employed to displace a molecule along a designated path to calculate the PMF based on Jarzynski's equality[81] (Equation (2)) under the assumption that the molecular displacement proceeds through quasi-static state:

$$\left\langle e^{-W/kT} \right\rangle = e^{-\Delta F/kT} \tag{2}$$

where W and ΔF denote the work done through the displacement of molecule and the corresponding free energy difference, respectively, and k and T is the Boltzmann constant

and absolute temperature, respectively. The PMF expresses the amount of work required for the molecular displacement, whose difference between its initial and final values is interpreted as the free energy change. Using such SMD simulation method, first, we obtained the PMF for a single water transport from the water phase to the core of SDS micelle. As shown in Figure 4.4a, the PMF was calculated through performing six independent SMD simulations. The initial positions of the water molecule in all cases were approximately 20 Å away from the surface of micelle. The steered molecular displacement was performed at 2.0×10^{-5} Å/fs with the spring constant of 200.0 kcal/mol/Å, which were determined after testing various conditions to achieve the converged PMF. Similarly, we performed SMD simulations to investigate the dissociation of a SDS molecule from the micelle using the same conditions mentioned above. For this purpose, we displaced a single SDS molecule from the equilibrated micelle to water phase as shown in Figure 4.4b. The simulation was independently repeated six times.

(a)

(b)
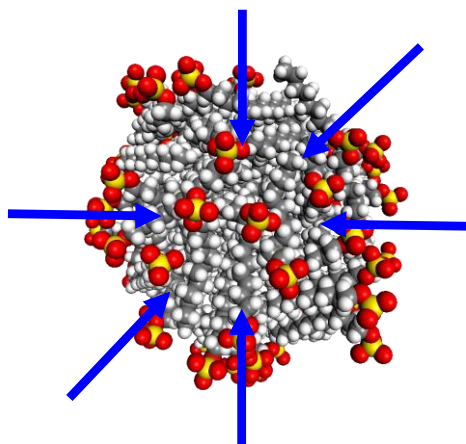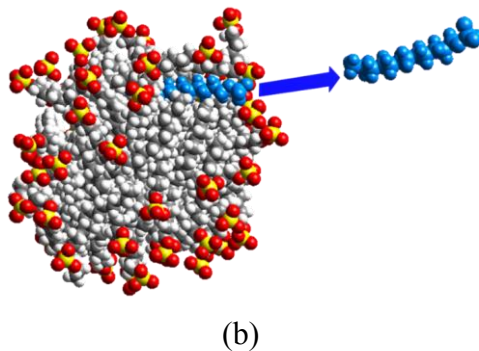
Figure 4.4. SMD simulations to calculate potential of mean force: (a) a water molecule is displaced from water phase to the center-of-mass of the micelle; (b) a SDS molecule is displace from the micelle to water phase. Arrows indicate the direction of the molecular displacement.

4.3. Results and Discussion

4.3.1. Structures and Energetics of SDS Micelle

A snapshot in Figure 4.2c shows one of the equilibrated micelle structures in which we find that the hydrophobic alkyl tails of SDS aggregate well and hydrophilic sulfate groups are located on the micelle surface. The radial density distribution analysis (Figure 4.5) also exhibits a consistent feature of the micelle structure in which the hydrophilic sulfate groups are associated with water phase whereas the hydrophobic hydrocarbons are aggregated in the micelle to reduce their undesirable interaction with water.
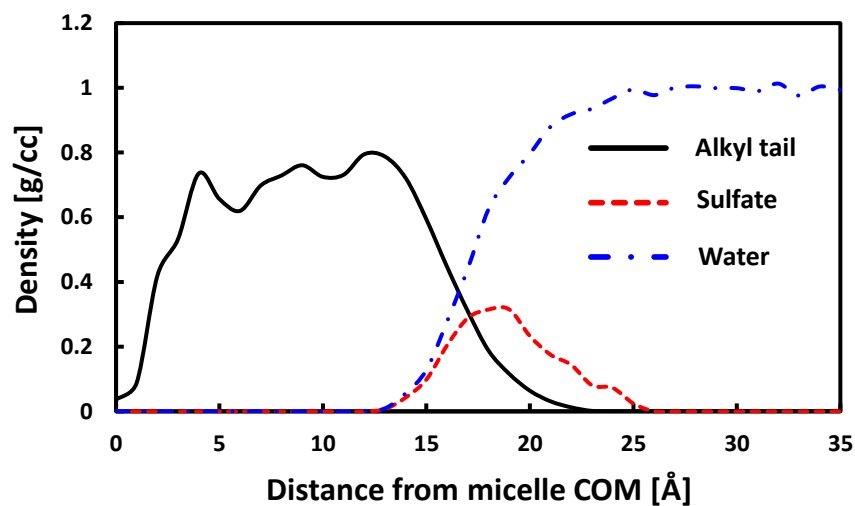
Figure 4.5. Radial density distribution from the center of micelle. The black, red, and blue colors denote the density of hydrocarbon, sulfate group, and water, respectively.

An interesting observation in Figures 4.2b and 4.2c is that a number of the sulfate functional groups are not enough to cover the entire surface of micelle, meaning that a significant portion of the surface would be occupied by hydrophobic alkyl tails. Indeed, the radial density profile in Figure 4.5 reveals that the alkyl tails contacts water phase directly to a certain extent. To characterize the micelle surface quantitatively, we performed the Connolly surface analysis with the probe radius of 1.4 Å. Through the equilibrium state of the simulation, the total surface area, hydrophilic surface area (occupied by sulfate groups), hydrophobic surface area (occupied by alkyl tails) were calculated as 9854.9 ± 207.3 Å^2, 4176.9 ± 31.2 Å^2, 5679.7 ± 201.1 Å^2, respectively, indicating that ~58 % of the micelle surface is occupied by alkyl tails. Therefore, it is confirmed that the 60 sulfate groups do not cover the entire micelle surface, which allow the direct contact between water phase and hydrophobic alkyl tail phase of the micelle.

Next, the dimension of micelle was evaluated by the geometric radius (R) (Equation (3))[35, 41, 80, 82] since the radius of gyration (R_g) does not necessarily represent the

apparent size of micelle since it has been known that R_g is highly dependent on the mass distribution within the object. The geometric radius of micelle is frequently calculated from its correlation with R_g as defined in Equation (3):

$$R = \sqrt{\frac{5}{3}} R_g \qquad (3)$$

The geometric radius is physically the radius of a sphere with a uniform density. From our simulations, the values of R_g and R for SDS micelle were calculated as ~16 Å and ~21 Å, respectively (Table 4.2). Although the experimental value of R_g for SDS micelle has not been found in literature, our R_g value is in a good agreement with that obtained from other simulation study[34, 35, 41], while R value is also in accordance with the experimental value [30]. Please note that the micelle surface area calculated using the geometric radius (R) is 5661.9 Å^2 that is ~57.5 % of the micelle surface calculated from the Connolly surface analysis. It is clearly due to the ruggedness of the micelle surface at molecular level.

Table 4.2. Dimension of simulated micelle in comparison with experimental data

		Radius of Gyration (Å)	Geometric Radius of Micelle (Å)
Simulation	Our work	16.4±0.04	21.2±0.05
	MacKerell[34]	16.02±0.06	N/A
	Bruce et al.[35]	16.2±0.12	20.9±0.15
	Jalili et al.[41]	15.7±0.2	20.3±0.3
Experiment	Itri et al.[30]	N/A	22.0-22.3

We also analyzed the conformations of individual SDS molecules in the micelle. Previously, Shelley et al.[33] and MacKerell[34] reported the gauche population of alkyl tails

for the micelle: 30 % and 20 %, respectively. Although the values were different in those two references, these two studies commonly observed the bent conformations. From our simulations, the gauche population is 15 %, which is less than those reported from the previous studies.[33, 34] However, it is also observed that the conformations of SDS molecules are significantly bent in equilibrium state as presented in Figure 4.6. In this analysis, we define two vectors and two angles. $\vec{r}_1$ is the vector from the center-of-mass (COM) of micelle to the head (sulfur, S in Figure 4.1) while $\vec{r}_2$ is the vector from the COM to the tail (carbon, C_1 in Figure 4.1). $\vec{r}_3$ is the tail-to-head vector of SDS. θ_1 is the angles between two segments (C_1-C_8 and C_8-S in Figure 4.1) in the alkyl tail and θ_2 is the angle between the tail-to-head vector and the COM-to-head vector ($\vec{r}_1$). Their measured values are summarized in Table 4.3.

Table 4.3. Results of geometry analysis. The symbols are corresponding to Figure 4.6.

$|\vec{r}_1|$	$|\vec{r}_2|$	θ_1	θ_2	**Free Volume**
20.12 ± 2.25 Å	11.41 ± 4.43 Å	$146.73 \pm 22.64°$	$67.60 \pm 3.83°$	138.98 ± 40.98 Å³

From this analysis, it is found that the length of the COM-to-head vector ($\vec{r}_1$) is ~20.1 Å, which is consistent with the geometric radius of the micelle (~21 Å in Table 4.3). This seems to be reasonable since the outermost part of the SDS micelle consists of ionic sulfate groups. On the other hand, the analysis of the COM-to-tail vector ($\vec{r}_2$) resulted in an unexpected feature of the micelle: the alkyl tails are not necessarily pointing towards the COM of micelle. From the length of $\vec{r}_2$ (~11.4 Å in Table 4.2), it is thought that the alkyl tail is significantly bent as presented in Figure 4.6. The analysis of the angle θ_1 confirms the bent conformation of SDS molecule, which makes the tail-to-head vector ($\vec{r}_3$) deviate from the vector $\vec{r}_1$. Actually, we believe that this conformational analysis is consistent with the analysis of the micelle surface (Figure 4.2c). Under the condition that

the hydrophilic sulfate groups do not cover the micelle surface, the alkyl tails should form a condensed phase in the micelle by bending their conformations to minimize the direct contact with water phase. If the SDS molecules kept their straight conformation, the micelle would not retain a stable spherical shape.
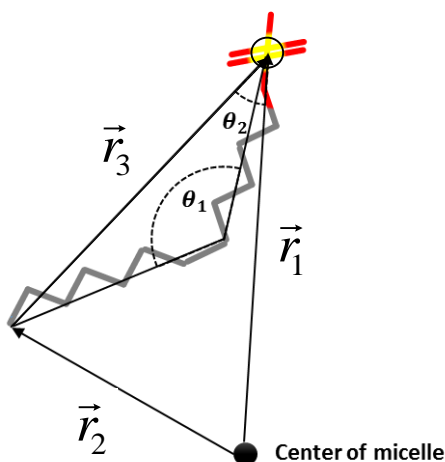
Figure 4.6. Geometry analysis of SDS molecule. The grey, yellow, and red colors denote carbon, sulfur, and oxygen, respectively. Hydrogens are omitted.

To investigate the packing of alkyl tails in the micelle, we evaluated the free volume within the micelle using the free volume analysis in Cerius2 molecular modeling software[83] with the probe radius of 1.4 Å. As a result, the evaluated internal free volume is ~139 Å³ (Table 4.2) that is equivalent to the volume of sphere with a radius of ~ 3.2 Å. The measured free volume corresponds to ~0.35 % of the micelle volume with the geometric radius (Table 4.3). Please note that this amount of free volume is dispersed throughout the micelle during our simulations. Since two or three water molecules with the radius of 1.4 Å are barely accommodated in such free volume if the free volumes are gathered together, it seems that the SDS micelle has a well packed hydrophobic core. Indeed, during our simulation time (20ns), we have not seen even single water molecule in the micelle.

The evolution of the shape of micelle during the simulation was characterized by examining the eccentricity (e) (Figure 4.7) via the following definition[35]:

$$e = 1 - \frac{I_{min}}{I_{avg}} \qquad (5)$$

where I_{min} and I_{avg} are the minimum moment of inertia and the averaged moment of inertia along with the x, y, or z axis. The zero value of the eccentricity means that the micelle is a perfect sphere.[35] The averaged eccentricity of the simulated micelle was measured to be 0.057, indicating that the micelle has nearly spherical shape.
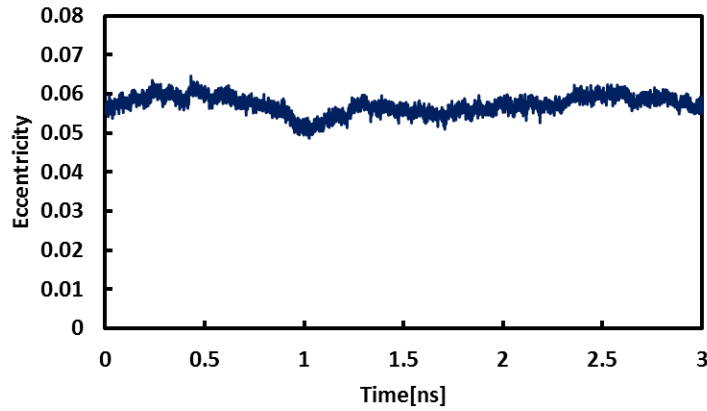
Figure 4.7. Change of Eccentricity of the micelle over the last 1 ns of the simulation

After 20 ns of the equilibration process, we obtained the formation energy ($\Delta E_{Formation}$) of SDS micelle (Figure 4.2c) was calculated by following equation:

$$\Delta E_{Formation} = E_{system} - n_{SDS} \times E_{SDS} - n_{water} \times E_{water} \qquad (6)$$

where E_{system}, E_{SDS}, E_{water}, n_{SDS} and n_{water} denote the potential energies of total system, single SDS molecule, single water molecule, the number of SDS molecules, and the number of water molecules in the system, respectively. The formation energies of the SDS micelle in vacuum and in water phase were calculated to be 7.07×10^3 kcal/mol and -222.88 kcal/mol, respectively. Considering that the formation energy is a measure of the stability of the system, such a highly positive formation energy of the micelle in vacuum means that the ordinary micelle structure consisting of hydrophobic core and hydrophilic shell is not energetically stable in vacuum, whereas the negative value of the formation energy in water phase indicates that the micelle in water phase is favorable. Therefore, it is clear that the micellization of SDS is not driven by the SDS-SDS interaction, but rather by the favorable water solvation of ionic head of SDS molecule.

4.3.2. Potential of Mean Force via Steered Molecular Dynamics Simulations

4.3.2.1. Water Permeation into Micelle.

In order to assess the cohesiveness of the micelle core consisting of hydrophobic tails, the PMF was calculated by dragging a single water molecule into the core of SDS micelle from the surrounding water phase using SMD simulation method. The results of PMF calculation (Figure 4.8) demonstrates that the PMF increases as water molecule diffuses into the core of micelle. It is evident that the change of PMF has two distinct stages: stage 1 is the region from 0 Å to 16 Å and stage 2 is the region from 16 Å to 35 Å. First, while the water molecule is dragged towards the micelle in the stage 2, the PMF increases mildly by ~1 kcal/mol since the water molecule diffuses through water phase without significant resistance. However, as seen in the radial density profile (Figure 4.5), the water phase disappears at 13 Å ~ 20 Å from the COM of the micelle, in which the increase of PMF becomes more rapidly in the stage 1 due to the unfavorable interaction of the dragged water molecule with the hydrophobic alkyl tails in the micelle. Therefore, the overall PMF

change is measured as ~10 kcal/mol. Since the PMF increases by ~1 kcal/mol in the stage 2, the PMF increment in the stage 1 is ~9 kcal/mol. According to the study done by Yoshii and his coworker[39], the free energy of water permeation into the hydrophobic core of SDS micelle was also calculated to be ~7 kcal/mol by the thermodynamic integration (TI) method, indicating that the magnitude of PMF change from SMD simulation is in a good agreement with the TI value although the theoretical foundation of each method is different. From this investigation, it is concluded that water molecules would not be able to diffuse in and out of the SDS micelle core.
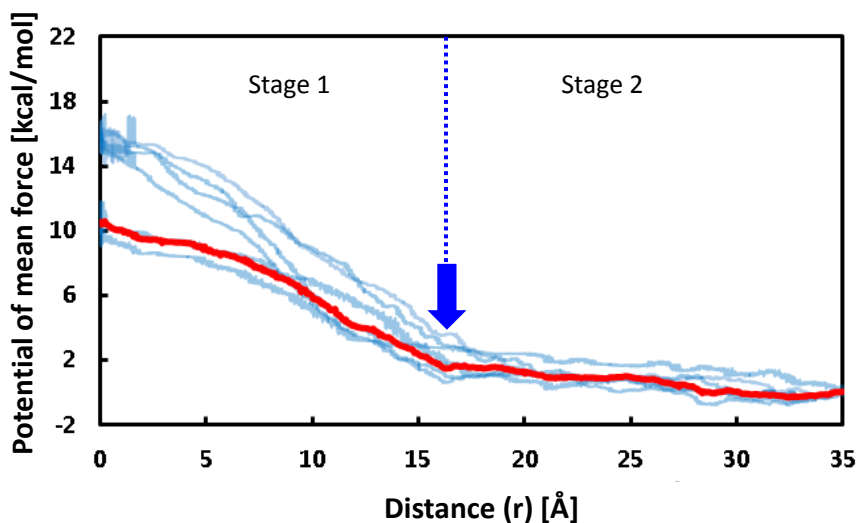
Figure 4.8. Change of potential of mean force as a function of the distance of water molecule from the center-of-mass of the micelle. Red colored curve denotes the PMF averaged over six simulated values displayed by light blue color.

4.3.2.2. Dissociation of SDS from Micelle.

The second set of SMD simulations was performed to calculate the PMF change to dissociate a single SDS molecule from the micelle. The PMF increment was approximately ~13 kcal/mol. It is clearly shown in Figure 4.9 that the PMF increased monotonously as the SDS molecule was pulled out of the micelle. The origin represents the initial position

of the sulfate group of SDS. Considering the length of SDS molecule (~16 Å), the end of the alkyl tail would be almost dissociated from the micelle when the SDS is displaced from the initial position by ~ 15 Å. When the SDS molecule is pulled, the conformation is linear but becomes more folded when it is completely dissociated from the micelle. Therefore, it is thought that larger slope of PMF curve up to ~ 15 Å means that PMF is increased mainly due to the destabilizing dissociation of the alkyl tail from the SDS molecule.
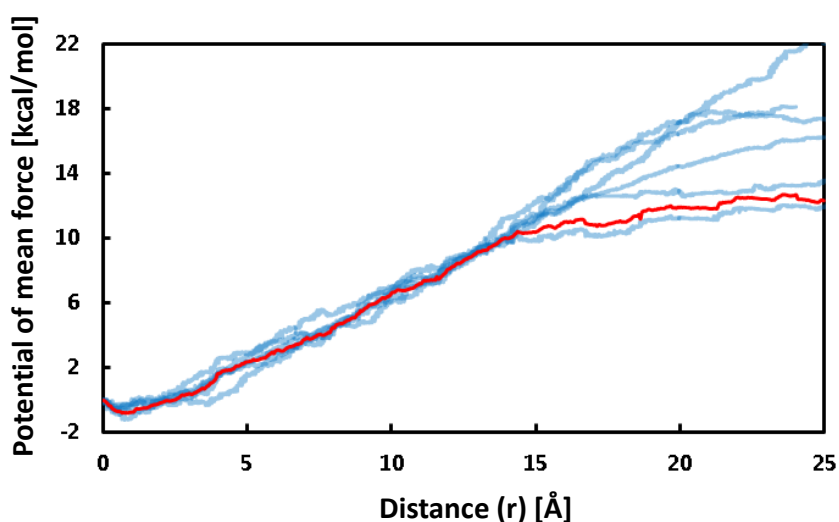
Figure 4.9. Change of potential of mean force as a function of the distance of a SDS molecule from micelle. The origin represents the initial position of sulfate group of SDS molecule. Red colored curve denotes the PMF averaged over six simulated values displayed by light blue color.

Considering that the phase of the hydrophobic alkyl tail is immiscible with water phase, this result is consistent with that of the first set of SMD simulations for the water diffusion-in. Accordingly, it is concluded that the SDS molecule would not be dissociated from the micelle unless an external energy more than ~13 kcal/mol is applied for SDS micelles. Overall, the increase of PMF in the direction of pulling in both cases well demonstrates the strong segregation between hydrocarbon and water phases. Here, it should be noted that the steering rate (2.0×10^{-5} Å/fs) employed in our SMD simulation

was determined to have no significant steering rate dependency in comparison with lower steering rate (1.0×10^{-5} Å/fs). Therefore, we believe that our SMD simulation condition would be able to produce approximate free energy difference efficiently although it should be admitted that the absolute quasistatic condition is not guaranteed.

4.4. Summary

A micelle consisting of 60 SDS molecules was investigated using molecular dynamics simulation method to elucidate the structure and stability in the presence of water phase. The formation energy of micelle was calculated as 7.07×10^3 kcal/mol and -222.88 kcal/mol in vacuum and water phase, respectively, which means that the stability of SDS micelle is achieved in water phase. The dimension was evaluated as ~16 Å and ~21 Å for radius of gyration and geometric radius, respectively, which are well agreed with the previous studies. Via Connolly surface analysis, it was found that ~58% of the micelle surface is occupied by the hydrophobic alkyl tails of SDS molecules.

By analyzing the conformations of SDS molecules in the micelle, it was found that the tail-to-head vectors of SDS molecules have ~68° in average from the radial direction, indicating that the SDS molecules have significantly bent conformation. However, it was also found from the free volume analysis that the SDS micelle has a well-packed structure with a free volume of ~139 $Å^3$ that is ~0.35 % of the micelle volume.

As a measure of the micelle stability in water phase, we performed SMD simulations in attempt to evaluate the PMF for the water diffusion into the center of micelle, resulting in ~10 kcal/mol. This result is due to the unfavorable interaction between water molecule and hydrophobic alkyl tails in the core of micelle. We also performed another set of SMD simulations to evaluate the PMF related to the molecular dissociation of a SDS molecule from the micelle. The magnitude of PMF change was ~13 kcal/mol. We think that such positive PMF change is caused by the undesirable interaction between the hydrophobic alkyl tail of the surfactant and water phase. Overall, the PMF analysis via two

sets of SMD simulations demonstrates that the micellization is driven by minimizing the

undesirable interaction of hydrophobic alkyl tail of SDS molecule with water phase.

4.5. References

[1]   Prince, L.M. *J. Colloid Interface Sci.* **1975**, *52*, 182.

[2]   Israelachvili, J.N.; Mitchell, D.J.;Ninham, B.W. *J. Chem. Soc. Faraday Trans. 2* **1976**, *72*, 1525.

[3]   Tanford, C. *Micellization, Solubilization and Microemulsions*; Plenum Press, **1977**.

[4]   Tanford, C. *The Hydrophobic Effect*; Wiley, **1980**.

[5]   Hunter, R.J. *Foundations of Colloid Science*; Clarendon Press, **1986**.

[6]   Hiemenz, P.C. *Principles of Colloid and Surface Chemistry*; Marcell Dekker, INC., **1986**.

[7]   Langevin, D. *Annu. Rev. Phys. Chem.* **1992**, *43*, 341.

[8]   Lavasanifar, A.; Samuel, J.;Kwon, G.S. *Adv. Drug Del. Rev.* **2002**, *54*, 169.

[9]   Zhang, H.;Annunziata, O. *Langmuir* **2009**, *25*, 3425.

[10]   Vuković, L.; Khatib, F.A.; Drake, S.P.; Madriaga, A.; Brandenburg, K.S.; Král, P.;Onyuksel, H. *J. Am. Chem. Soc.* **2011**, *133*, 13481.

[11]   Gröschel, A.H.; Schacher, F.H.; Schmalz, H.; Borisov, O.V.; Zhulina, E.B.; Walther, A.;Müller, A.H.E. *Nat. Commun.* **2012**, *3*, 710.

[12]   Guo, X.D.; Qian, Y.; Zhang, C.Y.; Nie, S.Y.;Zhang, L.J. *Soft Matter* **2012**, *8*, 9989.

[13]   Liu, Y.; Wang, Y.; Wang, Y.; Lu, J.; Piñón, V.;Weck, M. *J. Am. Chem. Soc.* **2011**, *133*, 14260.

[14]   Cotanda, P.;O'Reilly, R.K. *Chem. Commun.* **2012**, *48*, 10280.

[15]   Cotanda, P.; Lu, A.; Patterson, J.P.; Petzetakis, N.;O'Reilly, R.K. *Macromolecules* **2012**, *45*, 2377.

[16]   Lu, A.;O'Reilly, R.K. *Curr. Opin. Biotechnol.* **2013**, *24*, 639.

[17]   Reiss-Husson, F.;Luzzati, V. *J. Phys. Chem.* **1964**, *68*, 3504.

[18]   Mazer, N.A.; Benedek, G.B.;Carey, M.C. *J. Phys. Chem.* **1976**, *80*, 1075.

[19]   Young, C.Y.; Missel, P.J.; Mazer, N.A.; Benedek, G.B.;Carey, M.C. *J. Phys. Chem.* **1978**, *82*, 1375.

[20]   Rohde, A.;Sackmann, E. *J. Colloid Interface Sci.* **1979**, *70*, 494.

[21] Missel, P.J.; Mazer, N.A.; Benedek, G.B.; Young, C.Y.;Carey, M.C. *J. Phys. Chem.* **1980**, *84*, 1044.

[22] Ikeda, S.; Ozeki, S.;Hayashi, S. *Biophys. Chem.* **1980**, *11*, 417.

[23] Lianos, P.;Zana, R. *J. Colloid Interface Sci.* **1981**, *84*, 100.

[24] Lianos, P.; Lang, J.; Strazielle, C.;Zana, R. *J. Phys. Chem.* **1982**, *86*, 1019.

[25] Bendedouch, D.; Chen, S.H.;Koehler, W.C. *J. Phys. Chem.* **1983**, *87*, 153.

[26] Hayter, J.B.;Penfold, J. *Colloid. Polym. Sci.* **1983**, *261*, 1022.

[27] Croonen, Y.; Gelade, E.; Vanderzegel, M.; Vanderauweraer, M.; Vandendriessche, H.; Deschryver, F.C.;Almgren, M. *J. Phys. Chem.* **1983**, *87*, 1426.

[28] Chen, J.M.; Su, T.M.;Mou, C.Y. *J. Phys. Chem.* **1986**, *90*, 2418.

[29] Nagarajan, R.;Ruckenstein, E. *Langmuir* **1991**, *7*, 2934.

[30] Itri, R.;Amaral, L.Q. *J. Phys. Chem.* **1991**, *95*, 423.

[31] Moroi, Y.;Yoshida, N. *Langmuir* **1997**, *13*, 3909.

[32] Shirota, H.; Tamoto, Y.;Segawa, H. *J. Phys. Chem. A* **2004**, *108*, 3244.

[33] Shelley, J.; Watanabe, K.;Klein, M.L. *Int. J. Quantum Chem* **1990**, *38*, 103.

[34] Mackerell, A.D. *J. Phys. Chem.* **1995**, *99*, 1846.

[35] Bruce, C.D.; Berkowitz, M.L.; Perera, L.; Forbes, M.D.E.; Hill, C.;Carolina, N. *J. Phys. Chem. B* **2002**, *106*, 3788.

[36] Bruce, C.D.; Senapati, S.; Berkowitz, M.L.; Perera, L.; Forbes, M.D.E.; Hill, C.;Carolina, N. *J. Phys. Chem. B* **2002**, *106*, 10902.

[37] Yoshii, N.; Iwahashi, K.;Okazaki, S. *J. Chem. Phys.* **2006**, *124*, 184901.

[38] Yoshii, N.;Okazaki, S. *Condens. Matter Phys.* **2007**, *10*, 573.

[39] Yoshii, N.;Okazaki, S. *J. Chem. Phys.* **2007**, *126*, 096101.

[40] Shang, B.Z.; Wang, Z.;Larson, R.G. *J. Phys. Chem. B* **2008**, *112*, 2888.

[41] Jalili, S.;Akhavan, M. *Colloids Surf. Physicochem. Eng. Aspects* **2009**, *352*, 99.

[42] Palazzesi, F.; Calvaresi, M.;Zerbetto, F. *Soft Matter* **2011**, *7*, 9148.

[43]   Storm, S.; Jakobtorweihen, S.; Smirnova, I.;Panagiotopoulos, A.Z. *Langmuir* **2013**, *29*, 11582.

[44]   Tang, X.; Koenig, P.H.;Larson, R.G. *J. Phys. Chem. B* **2014**, *118*, 3864.

[45]   Bast, T.;Hentschke, R. *J. Mol. Model.* **1996**, *2*, 330.

[46]   Marrink, S.J.; Tieleman, D.P.;Mark, A.E. *J. Phys. Chem. B* **2000**, *104*, 12165.

[47]   Ferrara, P.; Apostolakis, J.;Caflisch, A. *Proteins* **2002**, *46*, 24.

[48]   Abel, S.; Sterpone, F.; Bandyopadhyay, S.;Marchi, M. *J. Phys. Chem. B* **2004**, *108*, 19458.

[49]   Moura, A.F.d.;Freitas, L.C.G. *Braz. J. Phys.* **2004**, *34*, 64.

[50]   Konidala, P.; He, L.;Niemeyer, B. *J. Mol. Graphics Modell.* **2006**, *25*, 77.

[51]   Pomata, M.H.H.; Laria, D.; Skaf, M.S.;Elola, M.D. *J. Chem. Phys.* **2008**, *129*, 244503.

[52]   Li, X.; Pivkin, I.V.; Liang, H.;Karniadakis, G.E. *Macromolecules* **2009**, *42*, 3195.

[53]   Kuramochi, H.; Andoh, Y.; Yoshii, N.;Okazaki, S. *J. Chem. Phys. B* **2009**, *113*, 15181.

[54]   Amani, A.; York, P.; de Waard, H.;Anwar, J. *Soft Matter* **2011**, *7*, 2900.

[55]   Lee, O.-S.; Stupp, S.I.;Schatz, G.C. *J. Am. Chem. Soc.* **2011**, *133*, 3677.

[56]   Barone, V.; Casarin, M.; Forrer, D.; Monti, S.;Prampolini, G. *J. Phys. Chem. C* **2011**, *115*, 18434.

[57]   Wang, Y.; Wallace, J.a.; Koenig, P.H.;Shen, J.K. *J. Comput. Chem.* **2011**, *32*, 2348.

[58]   Karjiban, R.A.; Basri, M.; Rahman, M.B.A.;Salleh, A.B. *Int. J. Mol. Sci.* **2012**, *13*, 9572.

[59]   Abel, S.; Dupradeau, F.-Y.;Marchi, M. *J. Chem. Theory Comput.* **2012**, *8*, 4610.

[60]   Guchhait, B.; Biswas, R.;Ghorai, P.K. *J. Phys. Chem. B* **2013**, *117*, 3345.

[61]   Thota, N.; Luo, Z.; Hu, Z.;Jiang, J. *J. Phys. Chem. B* **2013**, *117*, 9690.

[62]   Ingram, T.; Storm, S.; Kloss, L.; Mehling, T.; Jakobtorweihen, S.;Smirnova, I. *Langmuir* **2013**, *29*, 3527.

[63]   Bernardino, K.;de Moura, A.F. *J. Phys. Chem. B* **2013**, *117*, 7324.

[64]   Loverde, S.M. *J. Phys. Chem. Lett.* **2014**, *5*, 1659.

[65]   Emamyari, S.;Fazli, H. *Soft Matter* **2014**, *10*, 4248.

[66]   Bruce, C.D.; Senapati, S.; Berkowitz, M.L.; Perera, L.; Forbes, M.D.E.; Hill, C.;Carolina, N. *J. Phys. Chem. B* **2002**, *106*,

[67]   Brooks, B.R.; Bruccoleri, R.E.; Olafson, B.D.; States, D.J.; Swaminathan, S.;Karplus, M. *J. Comput. Chem.* **1983**, *4*, 187.

[68]   Jorgensen, W.L.; Chandrasekhar, J.; Madura, J.D.; Impey, R.W.;Klein, M.L. *J. Chem. Phys.* **1983**, *79*, 926.

[69]   Wang, J.; Wolf, R.M.; Caldwell, J.W.; Kollman, P.A.;Case, D.A. *J. Comput. Chem.* **2004**, *25*, 1157.

[70]   Marrink, S.J.; Risselada, H.J.; Yefimov, S.; Tieleman, D.P.;de Vries, A.H. *J. Phys. Chem. B* **2007**, *111*, 7812.

[71]   Mayo, S.L.; Olafson, B.D.;Goddard, W.A. *J. Phys. Chem.* **1990**, *94*, 8897.

[72]   Mulliken, R.S. *J. Chem. Phys.* **1955**, *23*, 1883.

[73]   Bochevarov, A.D.; Harder, E.; Hughes, T.F.; Greenwood, J.R.; Braden, D.A.; Philipp, D.M.; Rinaldo, D.; Halls, M.D.; Zhang, J.;Friesner, R.A. *Int. J. Quantum Chem* **2013**, *113*, 2110.

[74]   Levitt, M.; Hirshberg, M.; Sharon, R.; Laidig, K.E.;Daggett, V. *J. Phys. Chem. B* **1997**, *101*, 5051.

[75]   Nosé, S. *J. Chem. Phys.* **1984**, *81*, 511.

[76]   Hoover, W.G. *Phys. Rev. A* **1985**, *31*, 1695.

[77]   Hockney, R.W.;Eastwood, J.W. *Computer Simulation Using Particles*; Taylor & Francis, Inc., **1988**.

[78]   Swope, W.C.; Andersen, H.C.; Berens, P.H.;Wilson, K.R. *J. Chem. Phys.* **1982**, *76*, 637.

[79]   Plimpton, S. *J. Comput. Phys.* **1995**, *117*, 1.

[80]   Lobanov, M.Y.; Bogatyreva, N.S.;Galzitskaya, O.V. *Mol. Biol.* **2008**, *42*, 623.

[81]   Park, S.;Schulten, K. *J. Chem. Phys.* **2004**, *120*, 5946.

[82]   Bogusz, S.; Venable, R.M.;Pastor, R.W. *J. Phys. Chem. B* **2000**, *104*, 5462.

[83]   *Cerius2 Modeling Environment, Release 4.0*. 1999, Accelrys Inc.: San Diego.

CHAPTER 5

CHARACTERIZATION OF MOLECULAR ASSOCIATION OF POLY(2-OXAZOLINE)S-BASED MICELLES WITH VARIOUS EPOXIDES AND DIOLS VIA THE FLORY-HUGGINS THEORY: A MOLECULAR DYNAMICS SIMULATION APPROACH*

5.1. Introduction

Micelles consisting of poly(2-oxazoline)s (POXs) block copolymers have been extensively studied due to their potential for a variety of applications[1, 2] including drug delivery,[3, 4] pharmaceutical applications,[5, 6] and catalysis.[7-9] This variety of applications is attributed to the two aspects of POXs block copolymers: 1) the micelle properties that can be easily tuned by designing polymer blocks[1, 2, 10] and 2) the chain architectures of POXs block copolymer that can be tailor-made using living cationic ring-opening polymerization.[1, 2, 11-19]

Among the applications mentioned above, we focus on micellar catalysis.[2, 7, 9, 20, 21] An exceptional catalytic environment within a micelle structure can be created via well-defined phase-segregated internal structure of the micelle assemblies.[7-9] Commonly, the embedding of a catalyst into the core compartment of the micelle forms a high concentration of catalysts within the given volume of the micelle core, which provides a favorable condition for catalytic reactions.[8, 9] This idea can be expanded further to obtain consecutive reactions through the neighboring compartments in a micelle or through the combination of multiple micelles.[8]

We have reported that the hydrolytic kinetic resolution (HKR) of epoxides can be performed in nanoreactors consisting of POXs-based shell cross-linked multicompartment

micelle (SCM) and Co (III)-salen complex.[8] Kinetic resolution is a process in which one enantiomer reacts significantly faster than the other, leading to an accumulation of the less reactive enantiomer.[22, 23] By this, diol product will be produced from epoxide reactant due to the decisive difference in reaction kinetics. In this study, our simulation will focus on the diol molecule only because it is the main product. The core domain of the micelles containing Co (III)-salen is a highly reactive site due to its high catalyst concentration. The epoxide of interest (reactant) diffuses into the micelle core due to its hydrophobicity, while the hydrophilic diol product from HKR is released into the surrounding aqueous phase due to its hydrophilicity. Despite our success in developing a highly efficient micelle-based nanoreactor, we were not able to explain why the HKR for certain types of epoxide (e.g., epichlorohydrin) in the SCM does not occur or is very slow in comparison to the HKR in the bulk phase.[24] This contribution investigates the relationship of the properties for reactant/product with the characteristics of HKR catalyzed by the SCM nanoreactor.

Molecular simulation methods have been widely applied to investigate molecular properties based on their chemical structures.[25, 26] Particularly, molecular simulations have been extensively performed to study drug-polymer compatibility[27-31] and the drug release properties of drug carriers:[32-37] the former is determined by obtaining the thermodynamic properties such as free energy, whereas the latter describes kinetic properties related to molecular transport with energy barriers.

The focus of the present study is to predict the compatibility of reactant/product molecules with a POX-based block copolymer. In the aforementioned studies on the drug-polymer compatibility,[27-30, 38] the quantitative evaluation of such compatibility was attempted by employing the Flory-Huggins interaction parameters (χ). Patel and his coworkers[23] reported molecular dynamics (MD) simulations investigating the compatibility between water-insoluble drugs and self-associating PEO-b-PCL block copolymers. Kasimova *et al.*[39] performed MD simulations of lipophlilic drug molecules in polymeric micelles, which was validated by experiments. Both studies employed the χ

parameters as a descriptor for phase segregation or miscibility, which could establish a systematic design guide in efficiently developing new drugs with less use of resources.

We have reported that the reaction kinetics of HKR of epoxides depend on the chemical structure of reactant and product in the POXs block copolymer micelles.[8] Based on these results, we hypothesize that the compatibility of reactant/product with the POXs-based block copolymer has a significant influence on the kinetics through the molecular transport since the reactant may not enter the micelle if the compatibility is low, and similarly, the product will stay in the micellar core if the compatibility is high.

In this study, we characterize the compatibility of various reactant/product molecules with each block of POXs-based block copolymer by calculating the χ parameter from MD simulations, in order to investigate the effect of the compatibility on the reaction. Our simulation results are compared to the corresponding experimental observation.

5.2. Materials and Simulation Methods

5.2.1. Simulated Materials

The crosslinked micelle is formed from amphiphilic ABC-triblock copolymers based on poly(2-oxazoline)s. The polymer has a hydrophilic block (A) and a hydrophobic block (C). To stabilize the micelle, a crosslinking block (B) is introduced into the middle layer of the polymer. Monomer C was synthesized following the literature procedure[40] while monomer B was synthesized by a two-step one-pot reaction with a yield of 72% (see SI). Poly(2-oxazoline) triblock copolymers were synthesized via cationic ring-opening polymerization using methyl triflate as the initiator. The polymerization process was monitored by ^{1}H NMR spectroscopy and gel-permeation chromatography (GPC). The dispersity (Đ) and apparent molecular weight (M_n^{app}) of the final triblock copolymer **1** are 1.23 and 7,700 g mol^{-1} respectively, as determined by gel-permeation chromatography using poly(styrene) standards (see Appendix B). ^{1}H NMR spectrum of **1** showed degrees of polymerization of the individual blocks of a:b:c=62.1:6.7:8.3 (see Appendix B). The

ester end groups in the side-chain of hydrophobic block C were deprotected into carboxylic acids and served as a functional handle to attach the hydroxyl-functionalized salen ligand. The MALDI-TOF spectrum indicated that four salen ligands were attached in the hydrophobic block of polymer **2** (see Appendix B). Micelle formation was induced by dissolving polymer **3** in water (5 mg/mL) and was proved by dynamic light scattering (DLS) analysis. The thiol-yne reaction was chosen for the micelle crosslinking step between a dithiol linker and the carbon-carbon triple bonds in block B. The stable hydrodynamic radius from DLS analysis in different solvents proved the success of crosslinking. The SCMs were metalated with cobalt(II) acetate in a glovebox and then oxidized in air to produce the active Co(III)-salen micelles **5** (Figure 5.1). The hydrodynamic radius of **5**, determined by DLS, was 47 ± 5 nm, consistent with the radius of 50 ± 10 nm obtained by SEM (see SI). We studied the use of **5** as catalyst for the HKR of epoxides. Table 5.1 shows the reactants and corresponding products for the HKR using **5** with detailed information on reaction times and conversions. The conversion of HKR reaction was determined by chiral GC measurement. The chirality of the salen ligand only allows one enantiomer to reach the cobalt metal while the other enantiomer cannot be catalyzed due to the steric hindrance. Therefore, the highest conversion of a kinetic resolution reaction is 50 %. After 24 h, epichlorohydrin (entry 1) was less than 4% converted with an *ee* of 5%. Stryene oxide (entry 2) reached 48% conversion and 92% *ee* after twelve hours. Epoxyhexane (entry 3) with a longer side chain was completed in twelve hours with 96% *ee*. Phenyl glycidyl ether was resolved in five hours with 95% *ee*. These catalytic results using **5** were in agreement with our previous reported SCM catalysts.[8] Figure 5.3 shows the structures of reactants and products.
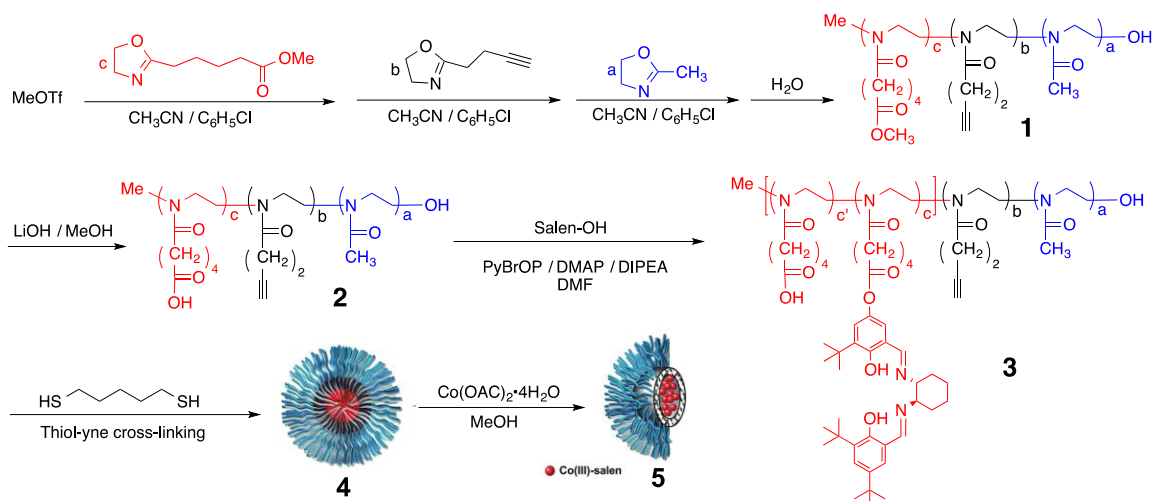
Figure 5.1. Schematic representation of the synthesis of poly(2-oxazoline) SCM with Co(III)-salen in the micelle core.

Table 5.1. Summary of the HKR of epoxides and experimental results using SCM catalyst **5**

Entry[a]	Reactant (epoxide)	Product (diol)	R	Time (h)[b]	Conv. (%)
1	Epichlorohydrin (Reac-Cl)	Chloropropane diol (Pro-Cl)	CH_2Cl	24	4
2	Styrene oxide (Reac-Ph)	Phenylethane diol (Pro-Ph)	Ph	12	48
3	Epoxyhexane (Reac-C4)	Hexane diol (Pro-C4)	*n*-butyl	8	50
4	Phenyl glycidyl ether (Reac-OPh)	Phenol glycerol ether (Pro-OPh)	CH_2OPh	5	49

[a] The reactions were carried out at room temperature using SCM catalyst **5** with a 0.1 mol% catalyst loading.
[b] The time required to complete the HKR of epoxide.

For the computations, we investigate three polymer blocks: poly(2-methyl-2-oxazoline) (PMOX), poly(2-(3-butinyl)-2-oxazoline) (PBOX), and poly(methyl-3-oxazol-2-yl) pentanoate with Co(III)-salen (PSCoX) as shown in Figures 5.2a, 5.2b and 5.2c, respectively. The POXs block copolymers containing these blocks form micelles in aqueous condition, as observed experimentally. Co-Salen in Figure 5.2c is Co(III)-salen (Figure 5.2d). To obtain the compatibility of reactants/products with each block, we modeled each block separately without other blocks, meaning that we performed MD simulations of the three types of homopolymers to investigate their molecular miscibility with the reactants and products in HKR.

(a)

(b)

(c)

(d)
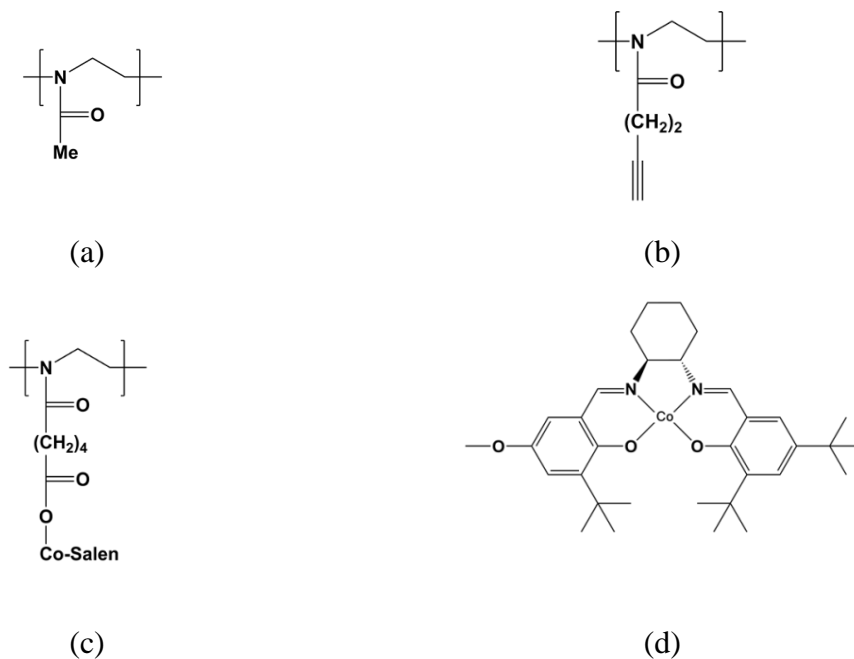
Figure 5.2. Monomers used in this study: (a) poly(2-methyl-2-oxazoline) (PMOX); (b) poly(2-(3-butinyl)-2-oxazoline) (PBOX); and (c) poly(methyl-3-oxazol-2-yl) pentanoate with (d) Co(III)-salen (PSCoX).
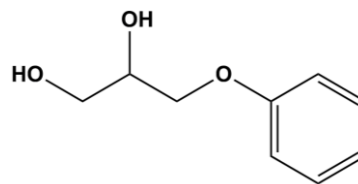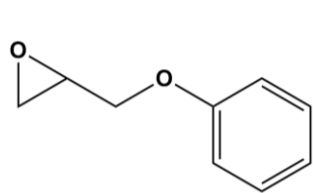
(a)
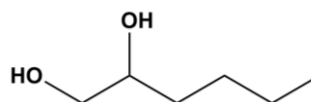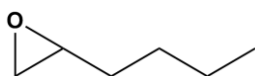
(b)
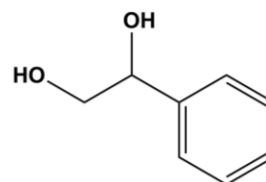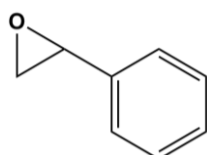
(c)
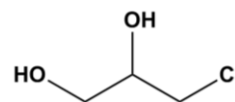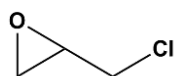
(d)

Figure 5.3. Chemical structures of the tested reactants and products. The left side of the figure contains the chemical structures of the reactants while the products are listed on the right side. (a) phenyl glycidyle ether and phenol glycerol ether (R-OPh and P-OPh) (b) epoxyhexane and hexane diol (R-C4 and P-C4) (c) styrene oxide and phenylethane diol (R-Ph and P-Ph) (d) epichlorohydrine and chloropropane diol (R-Cl and P-Cl).

5.2.2. Flory-Huggins Interaction Parameter (χ_{FH}) for Molecule-Polymer Interactions

The Flory-Huggins (FH) interaction parameter (χ_{FH}) is employed to evaluate the miscibility of reactants and products with each block, which is defined by the following equation:[29]

$$\chi_{FH} = \frac{V_{ref} \Delta H_{mix}}{RT} \qquad (1)$$

where V_{ref} is the molar volume of molecules in the mixture systems and ΔH_{mix} denotes the enthalpy of mixing, a measure of the molecular interaction.

In numerous studies,[28-30, 38] χ_{FH} has been used to characterize the interactions in drug-polymer binary systems. Originally, the FH theory was developed based on the lattice system to investigate the mixing of polymeric binary system using the Gibbs free energy change:[25]

$$\Delta G_{mix} = RT[n_1 \ln \phi_1 + n_2 \ln \phi_2 + n_1 \phi_2 \chi_{FH}] \qquad (2)$$

where R is the gas constant, T is the absolute temperature (K), and n_i and φ_i denote the number of moles and the volume fraction, respectively. The first two terms express the entropy of mixing while the last term describes the enthalpy of mixing. The dimensionless χ_{FH} parameter describes the interaction between reactant/product and polymer.

Recently, there have been several studies[28-30, 38] presenting the calculation of χ_{FH} through MD simulations. We calculated ΔE_{mix} from the energy of binding (ΔE_{bind}) of pure molecules (component 1), pure polymers (component 2), and molecule-polymer mixture (component 1-2) as Kasimova *et al.*[29] implemented in their work:

$$\Delta E_{mix} = \varphi_1 \left(\frac{\Delta E_{bind}}{V} \right)_1 + \varphi_2 \left(\frac{\Delta E_{bind}}{V} \right)_2 - \left(\frac{\Delta E_{bind}}{V} \right)_{1-2} \qquad (3)$$

where φ_1 and φ_2 are the volume fractions of components 1 and 2 in the mixture, V is the total volume of the system. Accordingly, the energy of mixing is dependent of the volume fraction of components in the mixture system, meaning that three systems should be simulated independently to calculate one χ_{FH} for a molecule-polymer pair. All the parameters in Equation (3) are directly taken from the trajectory of MD simulation.

5.2.3. DFT and MD Simulation Approach

The POX homopolymers were simulated using a full-atomistic model with the Dreiding force field.[41] The atomic partial charges for the repeating units were calculated using Mulliken population[42] with B3LYP/6-31G** in Jaguar.[43]

The temperature was maintained using Nosé-Hoover thermostat.[44, 45] The particle-particle particle-mesh (PPPM) method was used for the long-range electrostatic interaction calculation.[46] The equation of motion was integrated using velocity-Verlet algorithm with a time step of 1 fs.[47] A periodic boundary condition was imposed in all directions. The LAMMPS (large-scale atomic/molecular massively parallel simulator) code developed by Sandia National Laboratories was employed to perform MD simulations.[48]

5.3. Results and Discussion

5.3.1. Evaluation of Hydrophilicity and Hydrophobicity

The solvation free energy of each block was estimated via DFT calculation, which represents the extent of solvation in water. It is noted that the DFT-based solvation free energy has been widely used to indirectly evaluate the solubility of various molecules in a certain implicit solvent phase with a very dilute condition.[24]

On the other hand, MD simulation can describe relatively high concentration conditions using explicit solvent method, and thereby take into account the effect of other molecules including the solvent molecules on the molecular structure and dynamics. Thus, the molecular aggregate in water may undergo structural change over a certain period of the simulation time, depending on the molecular interaction with water phase, which cannot be fully considered in the implicit solvent method. We presume that, if we start MD simulation of molecular aggregate in water phase, the hydrophilic molecular aggregate would become dispersed, whereas the hydrophobic molecular aggregate would be maintained to minimize the contact with the aqueous phase. Based on this, the proposed work was performed in an attempt to assess a relative degree of hydrophobicity of blocks through the structural evolution in water phase in MD simulation.

5.3.1.1. Solvation Free Energy from DFT Calculations.

We used oligomers to model each block as shown in Figure 5.4 although each block has much longer length with higher degree of polymerization in the experimental work. Here, for fair comparison, we need to adjust the degree of polymerization (DP) to have similar molecular surface area that determines the amount of interaction with the surrounding water molecules. The Co(III)-salen attached with methyl 3-(oxazol-2-yl) pentanoate (hereinafter SCoX) has a molecular surface area of 262.45 Å^2, so that an octamer of 2-methyl-2-oxazoline (hereinafter MOX) and a tetramer of 2-(-3-butinyl)-2-oxazoline (hereinafter BOX) were prepared to have the molecular surface area of 238.35 Å^2 and 237.49 Å^2, respectively, as summarized in Table 5.2 and Figure 5.4, in order to eliminate the effect of molecular surface area.

Table 5.2. Specifications of simulated models in DFT calculation

Species	DP*	Surface Area (Å²)	
		Monomer	**Oligomer**
Octamer of 2-methyl-2-oxazoline (MOX)	8	62.70	238.35
Tetramer of 2-(3-butinyl)-2-oxazoline (BOX)	4	89.65	237.49
Co(III)-salen (SCoX) attached with methyl-3-(oxazol-2-yl)pentanoate	1	262.45	-

*DP denotes the degree of polymerization or number of repeating units in oligomer

(a)　　　　　　　　　(b)　　　　　　　　　(c)
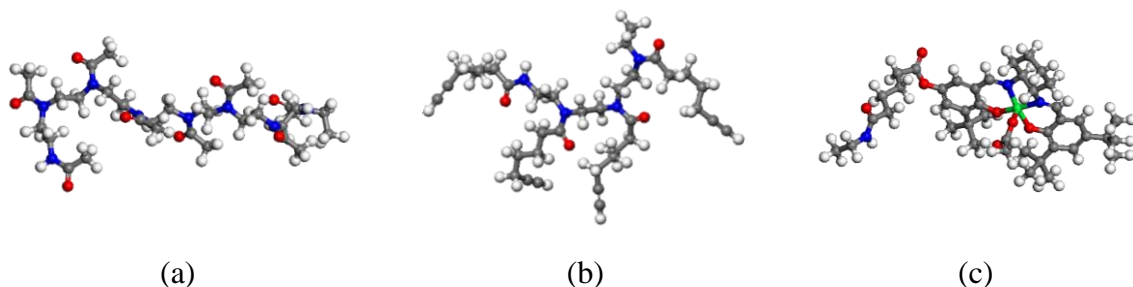
Figure 5.4. Molecules used in the DFT calculation: (a) octamer of 2-methyl-2-oxazoline; (b) tetramer of 2-(3-butinyl)-2-oxazoline; (c) Co(III)-salen attached with methyl-3-(oxazol-2-yl)pentanoate.

The solvation free energy of an octamer of MOX, tetramer of BOX, and SCoX were estimated to be -50.28 kcal/mol, -42.60 kcal/mol, and -32.96 kcal/mol, respectively, via DFT calculation. The results showed that the octamer of MOX is the most soluble in water whereas the organic complex of SCoX is the least soluble. This assessment agrees with the expectation of the hydrophilicity rank along the block copolymer for micelle formation in the experiment, which consists of PMOX, PBOX, and PSCoX for corona block, intermediate block, and core block, respectively (hereinafter PMOX, PBOX, and PSCoX) .

5.3.1.2. Change in Radius of Gyration from Molecular Dynamics Simulations

The clusters of homo-oligomers in water phase were monitored during equilibration at 300 K and 1 atm via NPT-MD simulation. As performed in the DFT calculation, since the size of two monomers, MOX and BOX, is far smaller than the size of SCoX, decamers of MOX and BOX were built to prepare clusters while a single unit of SCoX was used to prepare its cluster. The details of the simulation conditions are introduced in Table 5.3. The initial aggregates were prepared in vacuum, and then the rest of the space in the simulation box was filled with water molecules. In the beginning of the simulation, the restrained MD simulations were performed for 2 ns in order to relax the system, especially the aggregates-water interface as well as the water phase. Then, the MD simulations were performed to investigate the change in the radius of gyration (R_g) of the aggregates. Figure 5.5 shows that the radius of gyration of the MOX-decamer aggregate (Figure 5.6a) was gradually increased as a function of time, while BOX-decamer aggregate (Figure 5.6b) and SCoX aggregate (Figure 5.6c) were not changed significantly. In addition, these two models revealed that the size of aggregates was either sustained or contracted compared to their initial structures.
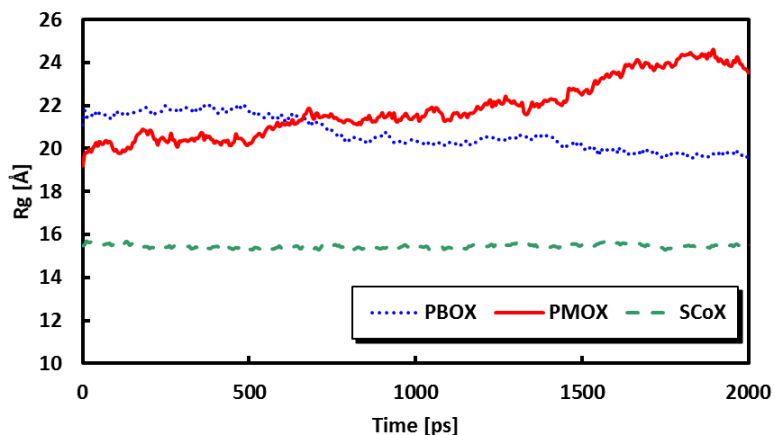
Figure 5.5. Change in the radius of gyration of molecular aggregates during 2 ns of NPT-MD simulation.

Initial   Final

(a)

Initial   Final

(b)

Initial   Final

(c)
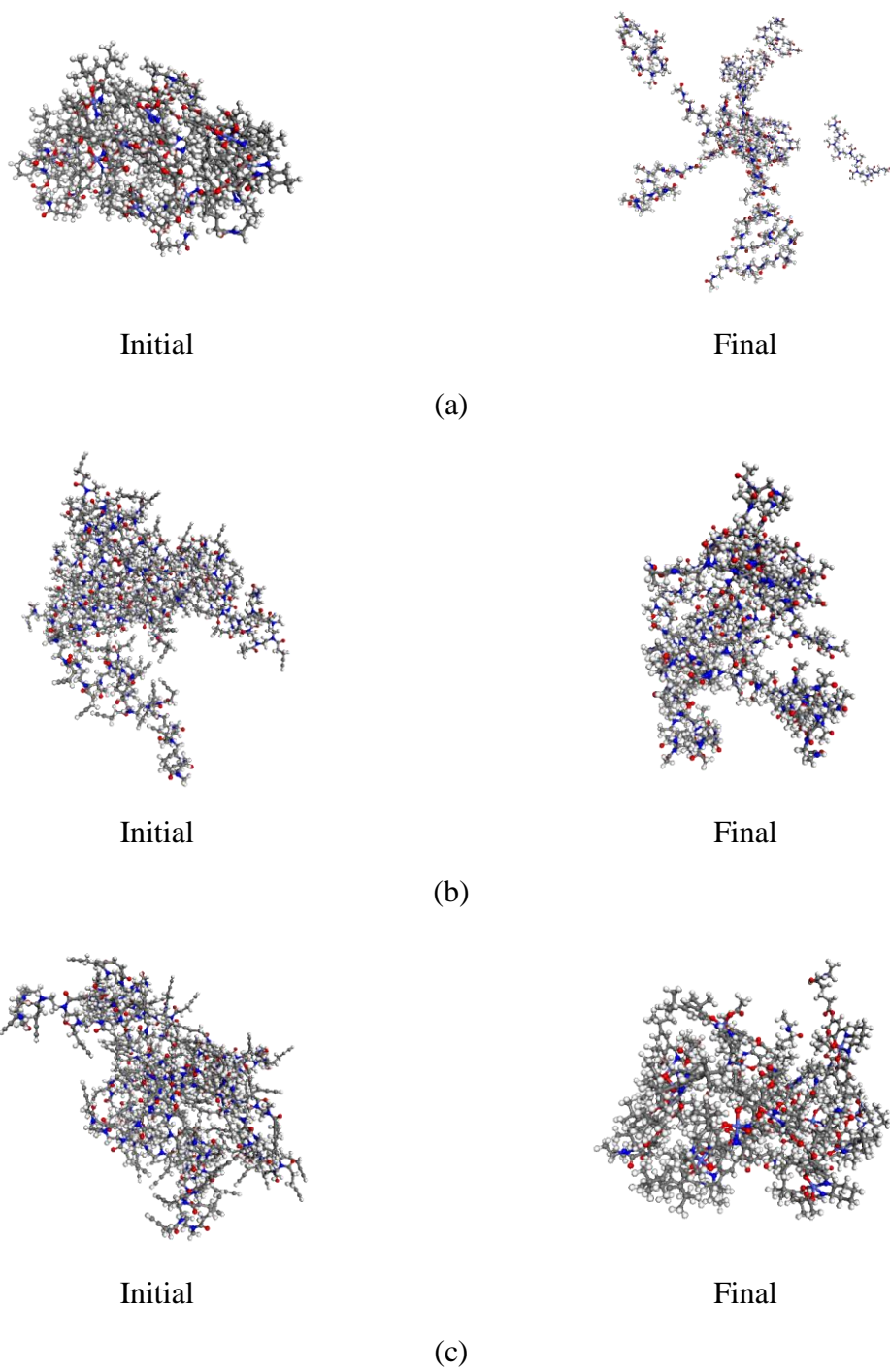
Figure 5.6. Snapshot of the cluster structures via 2ns-NPT MD simulations: (a) PMOX; (b) PBOX; (c) SCoX. The water molecules are invisible for clear view.

We found that our MD simulation results (Figures 5.5 and 5.6) are in a good accordance with the solvation free energy analysis using DFT calculation, confirming that the rank of hydrophilicity is MOX > BOX > SCoX. Please note that the branch groups determines the hydrophilicity since the backbone is all commonly 2-oxazoline. In addition, from this study, it is inferred that our MD simulation method is able to describe the molecular interactions and corresponding behavior well for further investigation.

Table 5.3. Conditions of the MD simulation for the cluster of oligomers in the water phase

	MOX	**BOX**	**SCoX**
Final Density of System	1.002±0.002	1.001±0.001	1.001±0.002
Weight Fraction of Solute	5.3 wt%	3.7 wt%	3.8 wt%
Number of oligomers per Cluster		15	

5.3.2. Flory-Huggins Interaction Parameter

The miscibilities of reactants and products with blocks such as PMOX, PBOX, and PSCoX are assumed to play key roles for implementing the HKR in SCM nanoreactor. The permeation of reactant/product through the micelle consisting of block copolymer chains is affected not only by the miscibility but also by various factors such as the density in the micelle, the concentration gradient and so on. Though, the miscibility as the result of molecular interaction of reactant/product with each block should be carefully investigated to understand the HKR in SCM nanoreactors. For instance, the high solubility of reactants in the polymer phase indicates the high miscibility between two components, meaning that the reactants have enhanced permeation into the micellar structure. Based on this hypothesis, χ_{AB} was calculated to assess the molecular interactions of reactants/products with blocks in the micelle in order to understand the experimental results for the HKR in a micelle consisting of block copolymers.[8, 36]

For this calculation, the 2-oxazoline derivatives such as MOX and BOX were polymerized to have 100 repeating units, while SCoX was polymerized to have 30

repeating units, which is due to the relatively small block length of SCoX compared to other two blocks in a micelle as used in the experimental study.[8] Then, mixtures of polymer-reactant and polymer-product were prepared with various compositions of reactants and products (15 wt%, 45 wt%, and 70 wt%).

The interaction parameters as a function of the weight fractions of reactants or products were used to thoroughly investigate the characteristics of phase segregation with various mixture compositions. As a result, 72 sets of simulations were performed to characterize the compatibility of four reactants and their corresponding products with three polymer blocks. The corresponding number of molecules for each mixture model is listed in Table 5.4.

Table 5.4. Content information of reactants and products in the mixture

Polymer Block	Terminal*	Cl (Cl)		Phenyl (Ph)		C_4H_9 (C4)		CH_2OPh	
	Weight Fraction	Reac[†]	Pro[⊥]	Reac	Pro	Reac	Pro	Reac	Pro
PSCoX	15%	100(17)	68(7)	80(11)	55(7)	55(7)	50(8)	68(7)	60(6)
	45%	400(46)	317(39)	380(50)	254(39)	254(39)	227(38)	317(39)	276(37)
	70%	1200(69)	900(68)	1080(73)	723(69)	723(69)	380(68)	900(68)	790(67)
PMOX	15%	16(15)	12(11)	15(15)	10(11)	10(11)	9(10)	12(11)	11(10)
	45%	75(45)	58(42)	70(52)	47(42)	47(42)	41(40)	58(42)	50(40)
	70%	220(68)	165(69)	200(76)	132(68)	132(68)	120(68)	165(69)	144(67)
PBOX	15%	24(15)	18(13)	20(16)	15(13)	15(13)	15(14)	18(13)	16(11)
	45%	110(44)	84(44)	100(52)	67(43)	67(43)	60(42)	84(44)	73(42)
	70%	310(66)	240(70)	290(77)	191(69)	191(69)	170(54)	240(70)	208(69)

The header "Number of Molecules in the Mixture with Polymer (corresponding volume fraction in %)" spans across the Cl, Phenyl, C4, and CH2OPh columns.

* R in Table 5.1; [†] Reac denotes Reactant; [⊥] Pro denotes Product

Once the initial structures were constructed, first, we ran annealing MD simulations for 8.5 ns, which consists of the heating and cooling processes, to achieve the relaxation of highly strained local structures. The details of the annealing MD simulation is found in the previous publications.[49] Then, an additional 2-ns NVT MD simulation and a subsequent 5-ns NPT MD simulation were performed at 1atm and 300K for equilibration. From the equilibrated systems, the cohesive energy ($\Delta E_{Cohesive}$) was calculated by following equation:

$$\Delta E_{Cohesive} = E_{System} - \sum_{i} n_i E_i \qquad (4)$$

where E_{System}, n_i, and E_i denote the energy of the system, the number of component molecule, and the energy of a single component molecule, respectively. After converting the weight fraction to the volume fraction, all the variables are substituted into Equation (3) to calculate the Flory-Huggins interaction parameter.

5.3.2.1. Reac-Cl and Pro-Cl

Figures 5.7a and 5.7b shows a series of the χ as a function of the weight fraction of reactant (Reac-Cl) and product (Pro-Cl), respectively. Figure 5.7a presents that the Reac-Cl has the largest χ value for the corona (PMOX) which keeps increasing with increasing weight fraction of reactant, indicating that that the Reac-Cl would not be well associated with corona (PMOX) of the micelle. Therefore, it is inferred that Reac-Cl would have very poor conversion in this micelle system due to the large χ parameter estimation predicting. Since the χ parameters with PBOX and PSCoX are smaller than that with PMOX, it is anticipated that the Reac-Cl in the corona (PMOX) might have a tendency to move toward to the inner regions of the micelle for better thermodynamic stability.

On the other hand, it is found from Figure 5.7b that the corresponding product, Pro-Cl has small χ parameter with the core (PSCoX), indicating that the Pro-Cl could stay

within the core for a while. However, as the concentration of Pro-Cl increases beyond the weight fraction of 0.6, its χ parameter becomes similar to that in PBOX. Thus, the Pro-Cl would be pushed out of the core. Overall, the reactant would not be able to enter the micelle well and the product would stay long in the micelle, implying that the reaction rate would be low.

(a)   (b)

Figure 5.7. Change of $\chi_{molecule-block}$ calculated from mixture of block with (a) Reac-Cl and (b) Pro-Cl with blocks, as a function of weight fraction of molecules.

5.3.2.2. Reac-Ph and Pro-Ph

As Figure 5.8a and 7b, the change of χ parameters for Reac-Ph and Pro-Ph are very similar with the previous case for Reac-Cl and Pro-Cl: it is not easy thermodynamically that the reactant, Reac-Ph gets into the corona of the micelle. Please note in Figure 5.8a that the χ parameters with the core is relatively small compared to that in the corona, so that the insertion of Reac-Ph into the micelle core seems much easier than that for the case of Reac-Cl. For the Pro-Ph shown in Figure 5.8b, the curves have similar behavior with those in Figure 5.7b. Therefore, it is expected that the association of Reac-Ph into the micelle is not thermodynamically easy, which is similar to the case of Reac-Cl. However, the incorporation of reactant into the micelle core would be greater for Reac-Ph than Reac-Cl due to the higher miscibility (smaller χ parameter) with the core.

84

Figure 5.8. Change of $\chi_{molecule\text{-}block}$ calculated from mixture of block with (a) Reac-Ph and (b) Pro-Ph with blocks, as a function of weight fraction of molecules.

5.3.2.3. Reac-C4 and Pro-C4

As can be seen in Figures 5.9a and 5.9b, the χ_{AB} parameters of both Reac-C4 and Pro-C4 are smaller than the previous two cases. This means that Reac-C4 and Pro-C4 would be relatively well associated with the blocks in the micelle. Especially, at the weight fraction of ~ 0.45, the solubility of Reac-C4 in each polymer is expected to be relatively favorable for the permeation. Therefore, it is anticipated that the favorable mixing thermodynamics for the reactant-polymer pair would enhance the HKR, which is clearly in a good agreement with the values in Table 5.1: the time required to complete the HKR is much shorter than the previous two cases. Now, we have one more case: according to the experimental results reported in Table 5.1, this last reactant has the best HKR efficiency. We see whether or not the rationalization based on χ_{AB} parameters would be valid.
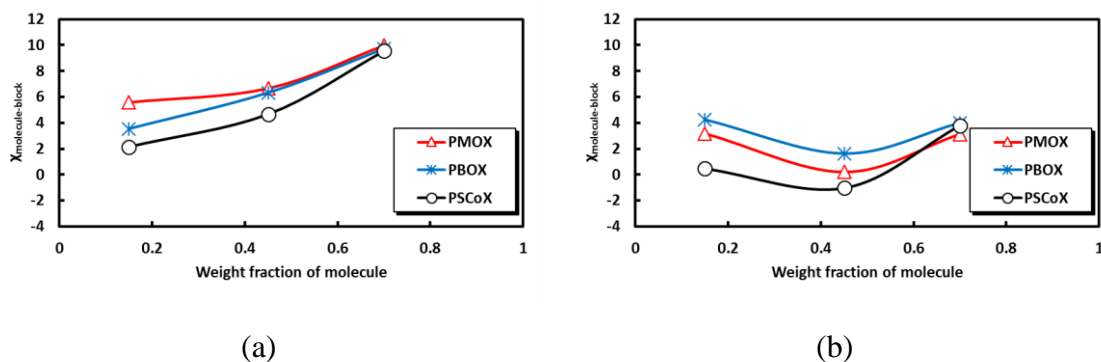
(a)   (b)

Figure 5.9. Change of $\chi_{molecule\text{-}block}$ calculated from mixture of block with (a) Reac-C4 and (b) Pro-C4 with blocks, as a function of weight fraction of molecules.

5.3.2.4. Reac-OPh and Pro-OPh

First, the χ_{AB} parameter of Reac-OPh with the corona (PMOX) is the lowest among the reactants simulated in this study, which facilitates the entrance of Reac-OPh into the micelle. Although the χ_{AB} parameter of Reac-OPh with the PBOX is slightly higher than that of Reac-C4 with the PBOX, the portion of PBOX block in the block copolymer in the experiment[8] is relatively insignificant compared to the portion of PMOX. It should also be noted that the χ_{AB} parameter with the core (PSCoX) is the lowest among the reactants. From the overall observations from the χ_{AB} parameters, it seems that Reac-OPh would have the most supportive environment in the micelle for the HKR. Furthermore, the miscibility of Pro-OPh with the core is slightly less than those of other products, meaning that, once the HKR reaction occurs, the Pro-OPh would be released out well compared to other products. Indeed, our χ_{AB} parameters for Reac-OPh and Pro-OPh rationalize why the HKR of Reac-OPh proceeds the best compared to other cases.

86

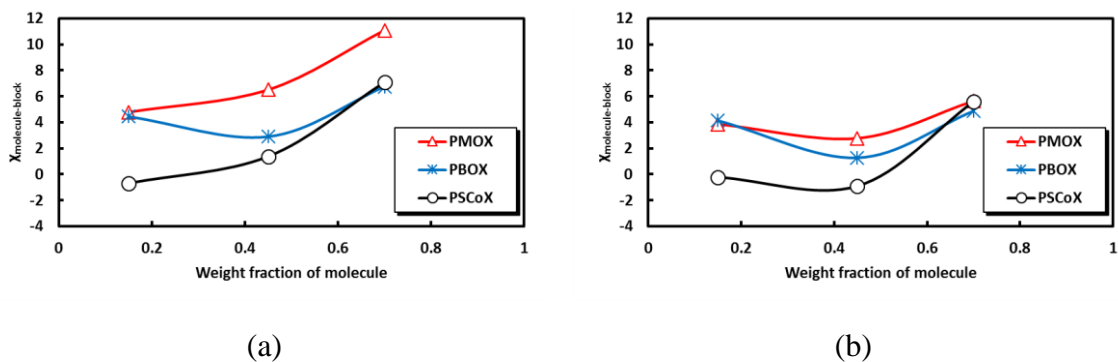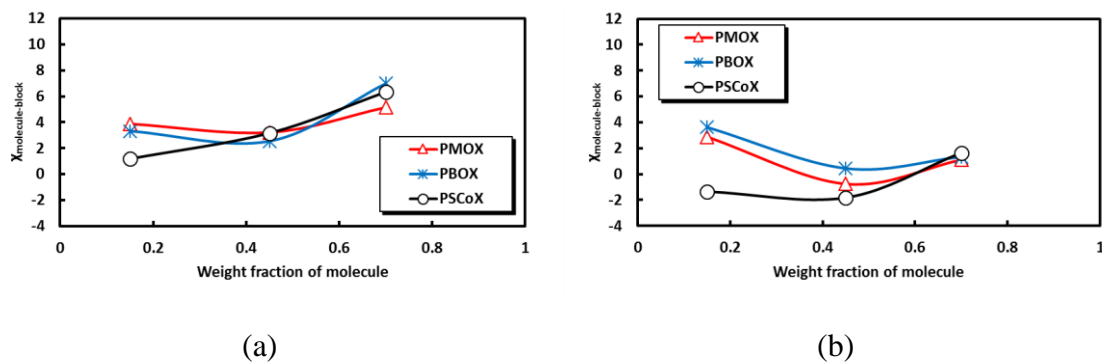(a)   (b)
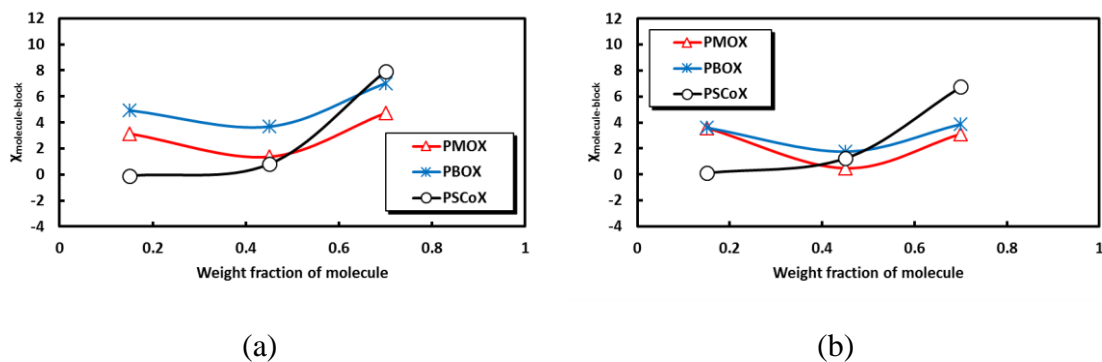
Figure 5.10. Change of $\chi_{molecule-block}$ calculated from mixture of block with (a) Reac-OPh and (b) Pro-OPh with blocks, as a function of weight fraction of molecules.

5.3.3. Potnetial of Mean Force Analysis

In this study, to validate the conclusions obtained in the previous section, we performed the potential of mean force analysis using steered molecular dynamics (SMD) that canestimate the free energy change as molecule is displaced from solvent phase to polymer phase. Therefore, it was intended that this SMD simulation confirms that the miscibility of the reactant/product with polymers has strong correlation with the reaction rate of HKR.

To calculate the potentials of mean force (PMF), the molecule was displaced through the quasi-static states.[50] For the robust calculation of the PMF, eight sets of SMD simulation were performed independently to obtain an ensemble average of the PMF results by the following definition:

$$PMF(r) = -RT \ln \left[\frac{1}{n} \sum_{i=1}^{n} \exp \left(\frac{-PMF_i(r)}{RT} \right) \right] \qquad (5)$$

where R, T, n and r denote the gas constant, temperature, number of trajectories, and displacement coordinate, respectively. Through this procedure, the PMFs were averaged as introduced from the Jarzynski equality that is most frequently used to calculate

approximate free energy change over a given irreversible paths. The free energy change is estimated by taking difference in values of PMF between point A and B.

In this study, a single reactant molecule was displaced at the rate of 10^{-5} Å/fs from the water phase to the center of polymer phase (Figure 5.11). To construct the polymer phase in a slab structure, we prepared the bulk phases of PMOX with the degree of polymerization (DP) of 50 and PSCoX with DP of 15 using NPT MD simulations at 300 K for 3 ns, and then extended one axis direction to make a slab. For this PMF analysis, we chose Reac-Cl and Reac-OPh because Reac-Cl and Reac-OPh show the least and most miscibility with the PMOX and PSCoX in the previous χ parameter analysis results. The reactant molecule was initially positioned approximately 10~15 Å above from the surface of polymer slab.

The results of the SMD simulations are displayed in Figure 5.21. According to the profile of PMF and density of polymer in the system, the PMF curves show a noticeable change along the direction of molecule displacement, especially when the reactants enter the polymer phase from the water phase. For both reactant molecules, it is commonly observed that the values of PMF drop at the surface of polymer slab. It is because the reactant molecules are more stable in the polymer phase compared to the water phase. It is also found that the PMF drop for Reac-OPh is ~1.2 kcal/mol and ~1.5 kcal/mol in PMOX (Figure 5.12a) and PSCoX (Figure 5.12b), respectively, while that for Reac-Cl is ~0.4 kcal/mol for both polymer phases (Figures 5.12a and 5.12b), which means that the free energy stabilization for Reac-OPh is greater when it enters the polymer phase in comparison to Reac-Cl. It is thought that the PMF change of reactants such as Reac-Cl and Reac-OPh is in a good agreement with the conclusion from the χ parameter-based miscibility, confirming that the χ parameter-based miscibility has strong correlation with the reaction rate of HKR.

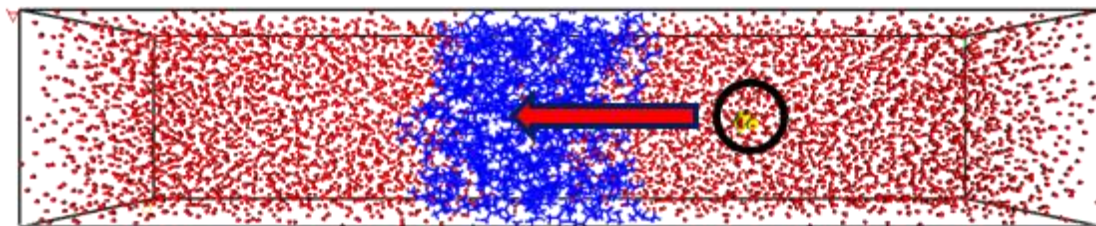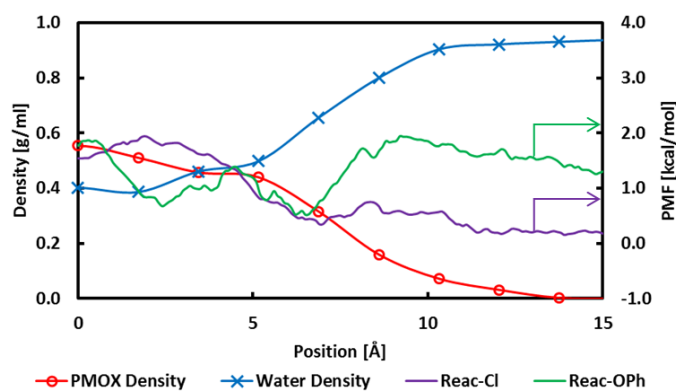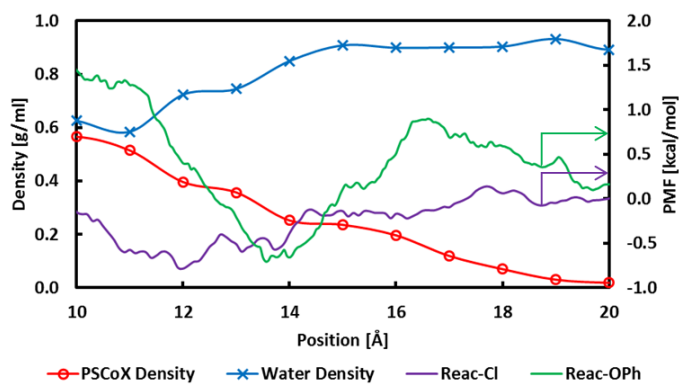**Figure 5.11.** Scheme of steered molecular dynamics simulation. Black circle and red arrow indicate the initial position of reactant molecule and the direction of the displacement, respectively. Red and blue color denote the water molecules and polymers, respectively.

(a)

(b)

Figure 5.12. Profiles of density and potentials of mean force as a function of position: Polymer slabs are (a) PMOX and (b) PSCoX.

5.4. Conclusions

The mixture systems of epoxides and diols with 2-oxazoline-based homopolymers were investigated using MD simulation method, from which the Flory-Huggins interaction parameters (χ) for each system were obtained to evaluate the miscibility of reactant/product with blocks in a micelle. Using these χ parameters, it was found that the molecular miscibility has strong correlation with the reaction rate of HKR in multicompartment micelle. To validate the scheme of the employed MD simulation, the solvation of blocks via MD simulation were compared to the solvation free energy calculated using DFT method with COSMO solvation method. According to the MD simulation results, it was observed that the PMOX oligomers are dispersed from the initial aggregate in water phase whereas the cluster of PBOX and PSCoX stayed as aggregated. The DFT solvation free energy of each block was in a good agreement with the MD simulation, confirming that the MD simulation can describe the interaction of blocks with solvent molecules.

To perform a thorough analysis based on the χ parameters, the blend systems were constructed with various compositions such as 15, 45 and 70 wt% of the reactant/product molecules with respect to the mixed polymers, indicating that the solubility of Reac-OPh in PMOX is the highest among others, followed by Reac-C4, Reac-Ph, and Reac-Cl. To validate these findings, the change of PMF during molecular displacement of Reac-Cl and Reac-OPh into polymer phases such as PMOX and PSCoX was calculated using SMD simulation. The results presented that the decrease of PMF for Reac-OPh is greater than that of Reac-Cl, meaning that the the incorporation of Reac-OPh is graeter than that of Reac-Cl. Overall, it was concluded from our χ parameter calculation that the better miscibility of the reactants with polymer blocks would enhance the higher reaction rate as long as the reactivity is the same.

In the future, the model micelle structure will be investigated to elucidate the radial density distribution of each block in order to quantitatively characterize the

reactant/product transport with the actual compositions of the micelle. We believe the spatial distribution of blocks through the micelle will provide more detailed information for molecular diffusion of reactants/products as well as their thermodynamic distributions.

5.5. References

[1]   Mittal, K.L. *Micellization, Solubilization, and Microemulsions*; Springer US, **1977**.

[2]   Hiemenz, P.C. *Principles of Colloid and Surface Chemistry*; Marcell Dekker, INC., **1986**.

[3]   Miyamoto, M.; Naka, K.; Shiozaki, M.; Chujo, Y.;Saegusa, T. *Macromolecules* **1990**, *23*, 3201.

[4]   Mero, A.; Pasut, G.; Via, L.D.; Fijten, M.W.M.; Schubert, U.S.; Hoogenboom, R.;Veronese, F.M. *J. Controlled Release* **2008**, *125*, 87.

[5]   Woodle, M.C.; Engbers, C.M.;Zalipsky, S. *Bioconj. Chem.* **1994**, *5*, 493.

[6]   Zalipsky, S.; Hansen, C.B.; Oaks, J.M.;Allen, T.M. *J. Pharm. Sci.* **1996**, *85*, 133.

[7]   Nuyken, O.; Persigehl, P.;Weberskirch, R. *Macromol. Symp.* **2002**, *177*, 163.

[8]   Liu, Y.; Wang, Y.; Wang, Y.; Lu, J.; Piñón, V.;Weck, M. *J. Am. Chem. Soc.* **2011**, *133*, 14260.

[9]   Liu, Y.; Pinon, V.;Weck, M. *Poly. Chem.* **2011**, *2*, 1964.

[10]   Hunter, R.J.;White, L.R. *Foundations of colloid science*; Clarendon Press, **1987**.

[11]   Reiss-Husson, F.;Luzzati, V. *J. Phys. Chem.* **1964**, *68*, 3504.

[12]   Mazer, N.A.; Benedek, G.B.;Carey, M.C. *J. Phys. Chem.* **1976**, *80*, 1075.

[13]   Young, C.Y.; Missel, P.J.; Mazer, N.A.; Benedek, G.B.;Carey, M.C. *J. Phys. Chem.* **1978**, *82*, 1375.

[14]   Rohde, A.;Sackmann, E. *J. Colloid Interface Sci.* **1979**, *70*, 494.

[15]   Missel, P.J.; Mazer, N.A.; Benedek, G.B.; Young, C.Y.;Carey, M.C. *J. Phys. Chem.* **1980**, *84*, 1044.

[16]   Hunter, R.J. *Foundations of Colloid Science*; Clarendon Press, **1986**.

[17]   Sfika, V.; Tsitsilianis, C.; Kiriy, A.; Gorodyska, G.;Stamm, M. *Macromolecules* **2004**, *37*, 9551.

[18]   Wiesbrock, F.; Hoogenboom, R.; Leenen, M.A.M.; Meier, M.A.R.;Schubert, U.S.

Macromolecules **2005**, *38*, 5025.

[19]   Schlaad, H.; Diehl, C.; Gress, A.; Meyer, M.; Demirel, A.L.; Nur, Y.;Bertin, A. *Macromol. Rapid Commun.* **2010**, *31*, 511.

[20]   Persigehl, P.; Jordan, R.;Nuyken, O. *Macromolecules* **2000**, *33*, 6977.

[21]   Kotre, T.; Zarka, M.T.; Krause, J.O.; Buchmeiser, M.R.; Weberskirch, R.;Nuyken, O. *Macromol. Symp.* **2004**, *217*, 203.

[22]   Tokunaga, M.; Larrow, J.F.; Kakiuchi, F.;Jacobsen, E.N. *Science* **1997**, *277*, 936.

[23]   Larrow, J.F.;Jacobsen, E.N. *Org. Synth.* **1998**, *75*, 1.

[24]   Klamt, A.;Schuurmann, G. *J. Chem. Soc., Perkin Trans. 2* **1993**799.

[25]   Fan, C.F.; Olafson, B.D.; Blanco, M.;Hsu, S.L. *Macromolecules* **1992**, *25*, 3667.

[26]   Doi, M. *Introduction to Polymer Physics*; Clarendon Press, **1996**.

[27]   Pajula, K.; Taskinen, M.; Lehto, V.-P.; Ketolainen, J.;Korhonen, O. *Mol. Pharm.* **2010**, *7*, 795.

[28]   Xiang, T.-X.;Anderson, B.D. *Mol. Pharm.* **2012**, *10*, 102.

[29]   Kasimova, A.O.; Pavan, G.M.; Danani, A.; Mondon, K.; Cristiani, A.; Scapozza, L.; Gurny, R.;Möller, M. *J. Phys. Chem. B* **2012**, *116*, 4338.

[30]   Thakral, S.;Thakral, N.K. *J. Pharm. Sci.* **2013**, *102*, 2254.

[31]   Patel, J.S.; Berteotti, A.; Ronsisvalle, S.; Rocchia, W.;Cavalli, A. *J. Chem. Inf. Model.* **2014**, *54*, 470.

[32]   Siepmann, J.; Lecomte, F.;Bodmeier, R. *J. Controlled Release* **1999**, *60*, 379.

[33]   Guo, X.D.; Tan, J.P.K.; Kim, S.H.; Zhang, L.J.; Zhang, Y.; Hedrick, J.L.; Yang, Y.Y.;Qian, Y. *Biomaterials* **2009**, *30*, 6556.

[34]   Vivcharuk, V.;Kaznessis, Y.N. *J. Phys. Chem. B* **2011**, *115*, 14704.

[35]   Guo, X.D.; Qian, Y.; Zhang, C.Y.; Nie, S.Y.;Zhang, L.J. *Soft Matter* **2012**, *8*, 9989.

[36]   Paloncýová, M.; Berka, K.;Otyepka, M. *Journal of Chemistry and Theory Computation* **2012**, *8*, 1200.

[37] Loverde, S.M. *J. Phys. Chem. Lett.* **2014**, *5*, 1659.

[38] Patel, S.; Lavasanifar, A.;Choi, P. *Biomacromolecules* **2008**, *9*, 3014.

[39] Kasimova, A.O.; Pavan, G.M.; Danani, A.; Mondon, K.; Cristiani, A.; Scapozza, L.; Gurny, R.;Möller, M. *J. Phys. Chem. B* **2012**, *116*,

[40] Zarka, M.T.; Nuyken, O.;Weberskirch, R. *Chem. Eur. J.* **2003**, *9*, 3228.

[41] Mayo, S.L.; Olafson, B.D.;Goddard, W.A. *J. Phys. Chem.* **1990**, *94*, 8897.

[42] Mulliken, R.S. *J. Chem. Phys.* **1955**, *23*, 1833.

[43] Bochevarov, A.D.; Harder, E.; Hughes, T.F.; Greenwood, J.R.; Braden, D.A.; Philipp, D.M.; Rinaldo, D.; Halls, M.D.; Zhang, J.;Friesner, R.A. *Int. J. Quantum Chem* **2013**, *113*, 2110.

[44] Nosé, S. *J. Chem. Phys.* **1984**, *81*, 511.

[45] Hoover, W.G. *Phys. Rev. A* **1985**, *31*, 1695.

[46] Hockney, R.W.;Eastwood, J.W. *Computer Simulation Using Particles*; Taylor & Francis, Inc., **1988**.

[47] Swope, W.C.; Andersen, H.C.; Berens, P.H.;Wilson, K.R. *J. Chem. Phys.* **1982**, *76*, 637.

[48] Plimpton, S. *J. Comput. Phys.* **1995**, *117*, 1.

[49] Jang, S.S.; Molinero, V.; Çağın, T.;Goddard, W.A. *J. Phys. Chem. B* **2004**, *108*, 3149.

[50] Park, S.;Schulten, K. *J. Chem. Phys.* **2004**, *120*, 5946.

CHAPTER 6

STUDY OF POLY(2-OXAZOLINE)S MULTICOMPARTMENT MICELLE NANOREACTOR FOR HYDROLYSIS KINETIC RESOLUTIONS OF EPOXIDES: DISSIPATIVE PARTICLE DYNAMICS SIMULATION APPROACH

6.1. Introduction

Multicompartment micelle nanoreactors have gained interest in recent catalysis chemistry.[1-8] These materials contain multiple well-defined regions with nanoscale structure, which has been shown potential for nanoreactor technology.[1-10] With advances made in polymer chemistry, the synthesis of well-defined polymeric blocks leads to a high degree of control over morphologies and functionalities of their aggregates.[6] In particular, the placement of reactive substrates or catalysts on the hydrophobic components results in achieving highly localized reactive sites in the micellar core in aqueous solvent environment.[4, 6, 9-11] Meanwhile, the hydrophilic shell can protect these sites from interacting with either solvent or impurities, which therefore prevents from degradation or deactivation.[2, 4, 7, 8, 11, 12]

In recent years, there are a number of studies using additional processes to improve the mechanical properties of micelles. One of the most common modifications is cross-linking of individual block copolymers that immobilized their micellar structure.[4, 9-11, 13-15] This results in substantially enhancing the structural stability of nanoparticles, which leads to the excellent recyclability of nanoreactors.[4, 9, 11] For instance, according to the results reported by O'Reilly and coworkers[3, 5, 16], by introducing functional groups in the process of polymer synthesis, they introduced the possibility of specific interactions such as

hydrogen bonding, ionic and hydrophobic interactions to produce a smart micelle nanoreactor, the selectivity and specificity of which are further improved.

As catalysts are highly localized and encapsulated by the shell of micelle, the accessibility of reactants to those reactive sites is recognized to be critical in micelle nanoreactor technology. For instance, Weck and coworkers[4, 11] have tested the performance of poly(2-oxazoline) (POX) based shell cross-liked multicompartment (SCM) micelles as nanoreactors for the hydrolysis kinetic resolution (HKR) of epoxides. Although the recyclability of catalysts was enhanced by immobilizing the micelle, the HKR of some epoxides via the SCM micelle nanoreactor occured with an unexpectedly slow rate, the cause of which may be from the presence of intermediate molecular structures before the reactive sites. Without a nanoreactor, the HKR of epichlorohydrin with Co(III)-salen (catalyst) was completed within 5 hours, however HKR in the nanoreactor was not completed even after 24 hours. This result indicated that the permeation of reactant through the shell encapsulating the reactive sites must play an important role for determining the rate of the HKR of epoxides.

To establish efficient methodologies for characterizing and enhancing the transport properties within the micellar nanoreactors, computational methods were employed and implemented in Chapter 5. To understand the limitations found in the work done by Weck and coworkers, their methods were used to determine whether or the micellar aggregate was capable of absorbing reactant molecules. In general, the permeation properties of polymeric materials are substantially governed by the structural characteristics of polymer architecture, which is related to permeability of materials, and the incorporation of permeate and media materials, which is the result of the gradient in chemical potentials of species. Using atomistic MD simulation, it is not be feasible to quantify the kinetics of diffusion whose rates are undetectably slow in nano- or micro-second scale simulations. For this reason, the incorporation of the selected reactants into the individual domains of the multicompartment micelle was targeted to predict the permeation of reactants in the

micelle structure using the Flory-Huggins interaction parameters (χ_{FH}) in Chapter 5. As a result, the poor solubility of reactant in the POX polymers was determined to be the cause of insufficient reaction rates.

In the following, we present the results of dissipative particle dynamics (DPD) simulation, a mesoscopic simulation developed by Hoogerbrugge and Koelman[17, 18], to study the micellar structure of POX based triblock copolymers and the association of its aggregates with the reactants and products. The recent DPD simulation modified by Groot and coworkers[19, 20] utilizes the characteristic nature of nanophase segregation among given components quantified by the Hildebrand Solubility parameter based χ_{FH} parameters. In 2000s, this kind of computer simulation has been successfully employed to analyze the microstructure and properties of polymers in the bulk state and in solvent.[21-28] Additionally, DPD simulations have been extensively employed to study the hydrodynamic behavior of complex fluids, the microphase separation of polymer mixtures, and the morphology and structure control of the multicompartment micelles from amphiphiplic polymers.[17-19] These studies have shown the structural details of the inner microphase-separated cores that are valuable understanding of multicompartment micelles.[29-34]

DPD simulations have demonstrated use for a number of practical applications. For instance, Liu and coworkers[30, 31, 35] performed the DPD simulations to study the self-assembly of two agents in the core-shell-corona multicompartment micelles of linear ABC triblock copolymers in selective solvent. They tested the equilibrated system of micelle with two agents, in which one agent was compatible with the core compartment and another agent was compatible with the shell compartment, and analyzed the distribution of these agents within the micellar structure. Inspired by these efforts, in this work, we implemented DPD simulations and characterized the structure of aggregates and the distribution of reactant/product molecules within the micellar nanoreactor. Next, the Hildebrand Solubility parameter based χ_{FH} parameters were evaluated by comparing with the χ_{FH} parameters obtained in Chapter 5.

6.2. Materials and Simulation Methods

6.2.1. Materials

In a DPD simulation, the atomistic details of polymer structure are replaced by a coarse-grained bead-spring model, each bead of which (i.e., the DPD particle) corresponds to a group of several atoms.[17-20] In this study, three POX derivatives were expressed using beads as shown in Figure 6.1. Similarly, the reactant and product molecules that were tested in the previous studies were coarse-grained as displayed in Table 6.1.
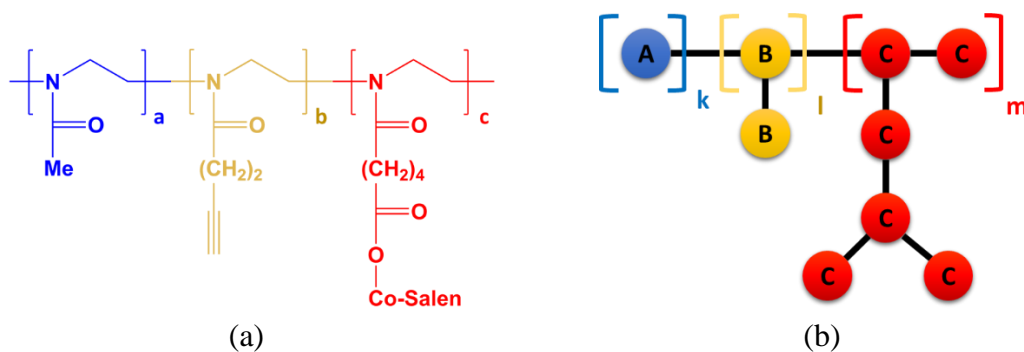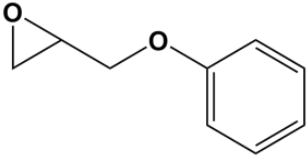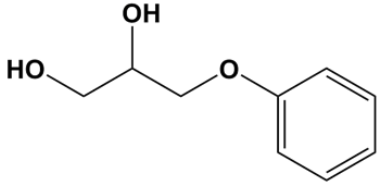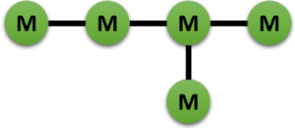

(a)   (b)
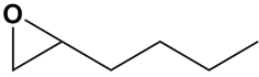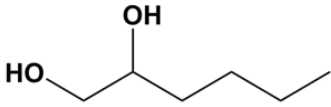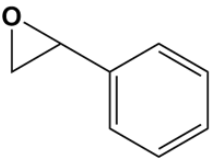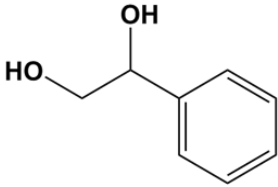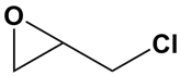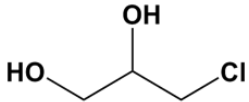
Figure 6.1. Atomistic expression of POX derivatives and their coarse-grained model in DPD simulation. Blue, yellow, and red colored structure in (a) represent poly(2-metyl-2-oxazoline), poly(2-(3-butinyl)-2-oxazoline), and poly(methyl-3-oxazol-2-yl) pentanoate with Co(III)-salen (hereafter, PMOX, PBOX, and PSCoX, respectively). Likewise, blue, yellow, and red colored beads in (b) denote the coarse-grained PMOX, PBOX, and PSCoX, respectively.

Table 6.1. Atomistic chemical structures of reactant and product molecules and their coarse-grained model in DPD simulation. Each water molecule was replaced with single bead in this simulation scheme.

Entry	Atomistic Chemical Structure		Coarse-Grained Model
1	Phenyl glycidyle ether (Reac-OPh)	Phenol glycerol ether (Pro-OPh)	
2	Epoxyhexane (Reac-C4)	Hexane diol (Pro-C4)	
3	Styrene oxide (Reac-Ph)	Phenylethane diol (Pro-Ph)	
4	Epichlorohydrine (Reac-Cl)	Chloropropane diol (Pro-Cl)	

6.2.2. DPD Simulation Details

The momenta and position vectors of the DPD particles are governed by Newton's equations of motion:[17, 18, 20]

$$\frac{d\vec{r}_i}{dt} = \vec{v}_i, \quad m_i \frac{d\vec{v}_i}{dt} = \vec{f}_i \tag{1}$$

where $\vec{r}_i, \vec{v}_i$ and m_i are the position, velocity, and mass of the ith particle, respectively. The force $\vec{f}_i$ acting on each particle in the DPD simulation consists of:

$$\vec{f}_i = \sum_{j \neq i} (F_{ij}^C + F_{ij}^D + F_{ij}^R) \tag{2}$$

where F_{ij}^C, F_{ij}^D, and F_{ij}^R are denoted for the conservative force, the dissipative force, and the random force. The three forces are considered within a certain cutoff radius r_c. The conservative force is a soft repulsion acting along the line of centers and is given by

$$F_{ij}^C = \begin{cases} a_{ij}(1 - r_{ij}/r_c)\hat{r}_{ij} \\ 0 \end{cases} \quad \vec{r}_{ij} = \vec{r}_j - \vec{r}_i \quad r_{ij} = |\vec{r}_{ij}| \quad \hat{r}_{ij} = \vec{r}_{ij}/|\vec{r}_{ij}| \quad \begin{matrix} (r_{ij} < r_c) \\ (r_{ij} \geq r_c) \end{matrix} \tag{3}$$

where a_{ij} is a maximum repulsion force between particles i and j. The parameters for repulsion between particles of different types are obtained as a function of the Flory-Huggins interaction parameter χ_{ij} calculated from the Hildebrand solubility parameter. In the case where the reduced density ρ is 3, the repulsive parameter is expressed as follows:[20]

$$a_{ij} = a_{ii} + 3.27\chi_{ij} \tag{4}$$

$$\chi_{ij} = \frac{V_m\left(\delta_i - \delta_j\right)^2}{RT} \tag{5}$$

where δ_i, V_m, R and T are the solubility parameter of particle i, the volume of individual particle, gas constant, and temperature (300 K). The dissipative force F^D and the random force F^R are expressed by:

$$F_{ij}^{\ D} = -\gamma\omega^D(r_{ij})(\hat{r}_{ij} \bullet v_{ij})\hat{r}_{ij} \qquad \vec{v}_{ij} = \vec{v}_j - \vec{v}_i, \tag{6}$$

$$F_{ij}^{\ R} = \sigma\omega^R(r_{ij})\theta_{ij}\hat{r}_{ij} \tag{7}$$

where ω^D and ω^R are weight functions vanishing for $r > r_c$, γ is the friction coefficient, σ is the noise amplitude, and θ_{ij} is a randomly fluctuating variable with Gaussian statistics. The two weight functions can be taken simply as

$$\omega^D(r) = [\omega^R(r)]^2 = \begin{cases} (1 - r_{ij}/r_c)^2 & (r_{ij} < r_c) \\ 0 & (r_{ij} \geq r_c) \end{cases} \tag{8}$$

$$\sigma^2 = 2\gamma k_B T \tag{9}$$

A simulated box size was fixed at $25\times25\times25$ r_c^3 with periodic boundary conditions. With the bead density of 3, the box contained about 47,000 DPD beads, 10% of which was used for the polymer molecules. The time step and the harmonic spring constant were taken

101

as 0.05 and 4. The simulation took a total of 2×10^5 DPD steps to equilibrate the system. Table 6.2 is the tabulated repulsive parameters used in this DPD simulation.

To quantitatively analyze the simulated micellar structures, radial distribution function (RDF) was utilized. The RDF, which is usually denoted by $g(r)$, is calculated by the following equation:

$$g_{center-particle}(r) = \left(\frac{n_{particle}}{4\pi r^2 \Delta r} \right) \bigg/ \left(\frac{N_{particle}}{V} \right) \tag{10}$$

where $n_{particle}$, V, and $N_{particle}$ denote the number of particle found in a shell shaped region $4\pi r^2 \Delta r$, the volume of system, and the number of particle in the system. The RDF in this study represents the radial position of particles from the center of micelle.

Table 6.2. Repulsive parameters among components in DPD simulation system. A, B, C, and W denote PMOX, PBOX, PSCoX and water solvent, respectively. Since only one type of reactant or product molecules was mixed with the polymer micelle, there is no parameter among reactant and product molecules.

	A (PMOX)	B (PBOX)	C (PSCoX)	W (Water)
A	25.00	-	-	-
B	25.01	25.00	-	-
C	26.60	26.34	25.00	-
W	83.57	85.23	104.56	25.00
Reac-OPh	25.84	26.17	32.93	136.35
Reac-C4	25.00	25.04	28.70	155.98
Reac-Ph	36.38	37.50	52.79	90.56
Reac-Cl	30.46	31.24	42.93	108.43
Pro-OPh	25.20	25.38	30.53	146.40
Pro-C4	26.26	25.92	25.60	183.55
Pro-Ph	28.81	29.47	39.83	115.60
Pro-Cl	25.30	25.50	30.97	144.39

6.3. Results and Discussion

The first task was to determine the composition of blocks in the polymeric structure that leads to the formation of micelle during the equilibration of the mixture system. The work flow chart exhibited in Figure 6.2 describes the process to determine the overall conditions to construct the micelle with the repulsive parameters introduced in Table 6.2. As introduced in the previous section, a number of beads used for the particle-spring structure of POX block copolymer are fixed. Thus, the modification of block compositions in the polymer depends on the overall fraction of polymer in this case.
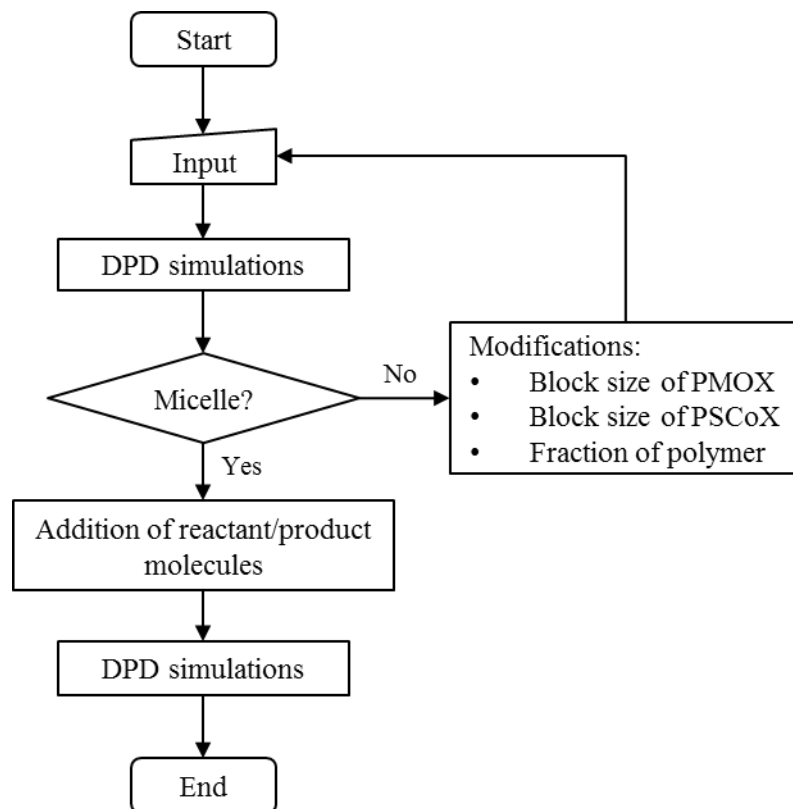
Figure 6.2. Flow chart to search for the block sequence of micelle building block copolymers in DPD simulation with a given set of repulsive parameters.

A total of 5 simulations were performed to search the most reasonable structure to test for the next step of simulation where the reactant and product molecules were added to the multicompartment micelle ($A_{15}B_4C_4$, $A_{15}B_8C_2$, $A_{30}B_4C_2$, $A_{30}B_4C_4$, and $A_{50}B_2C_2$). As a result, the block sequence of $A_{50}B_2C_2$, in which block A, B and C represent PMOX, PBOX and PSCoX, respectively, was determined to be the triblock copolymers whose assembly was used for further simulation due to its clear discontinuity between the core and shell domains.
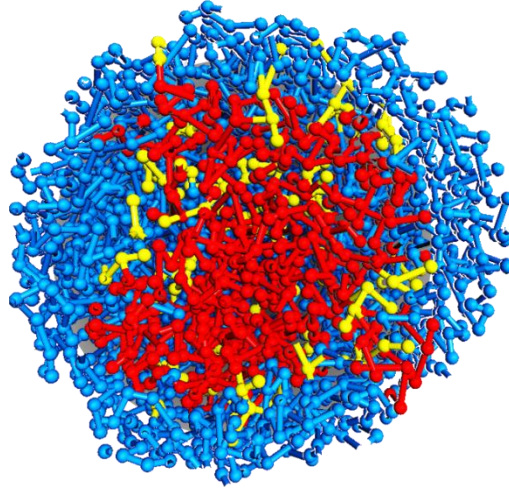
(a)
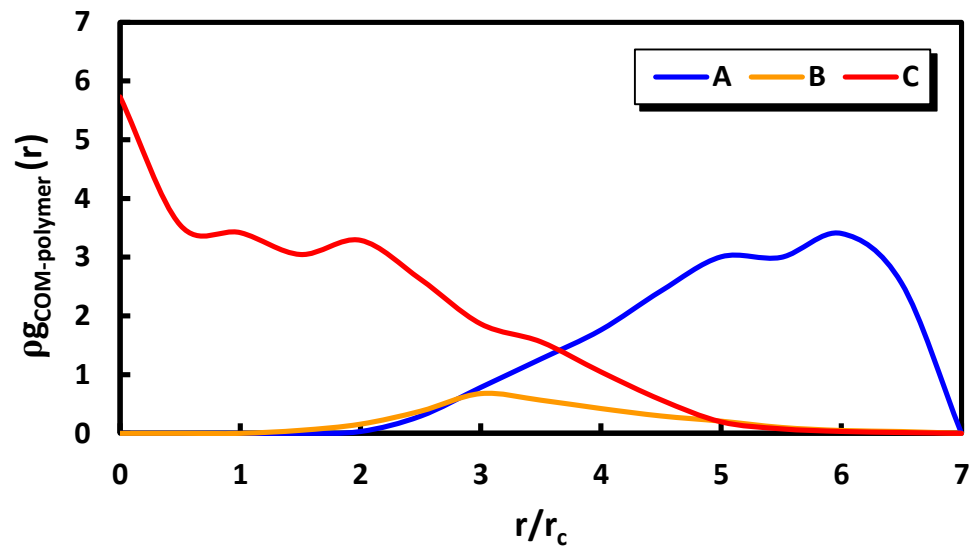
(b)

Figure 6.3. Results of DPD simulation. (a) is the cross-sectional view of micellar structure. Blue, yellow, and red colored regions indicate block A, B, and C (the coarse-grained PMOX, PBOX, and PSCoX blocks), respectively. (b) is the RDF plot of three components from the center of micellar structure.

As shown in Figure 6.3a, it was observed that the hydrophobic components formed the micelle core to minimize the interaction with solvent phase while the hydrophilic shell

was formed to shield the core from the external environment, which is as described in the definition of micelle structure. The plot in Figure 6.3b confirms the separation of each component within the structure. The core domain (block C) was located in between the radial positions of $(1 - 5)r_c$ from the center of micelle. On the other hand, the most of block A was detected in the outermost region, equivalent to the radial positions ranging from $(5 - 7)r_c$. Since each region is not evenly distributed in the radial direction from the center of structure, the overlapped regions from the plot may seem to be larger than displayed via the qualitative information in Figure 6.3a. The aggregation number in this simulation was found to be 71 (equivalent to 0.16 mol%). Overall, the DPD simulation demonstrated the distinct features of micellar structure. Therefore, it was assumed that the obtained structure would reflect the influence of individual block-molecule interaction on the incorporation of reactant and product molecules in the micellar structure.

The following results introduce the results of DPD simulations that display the distribution of reactant molecules in the micellar structure. In each case, a total of 450 molecules of reactant were added to the system (equivalent to 1.1 mol%). The corresponding products were also simulated with the micellar structure. However, the analysis of the simulation results with product molecules is not included in this following section. The related data can be found in Appendix C.

6.3.1. Reac-OPh and Reac-C4

In Figure 6.4a, due to the weak repulsion force between Reac-OPh molecules and polymer structure, numerous reactant molecules were clearly found in the hydrophilic domain (block A). In addition, some amount of reactant molecules were in the position near around the core domain. According to Figure 6.4b, it was determined that both the reactant and block A occupied the space in between the radial position of $(5 - 7)r_c$. There were few reactant molecules present within the hydrophobic domain including the region of block B. The thickness of the interphase with reactant phase were estimated to be 5, 2, and $1r_c$ in the phase of block A, block B, and block C, respectively. By estimating the area under the curves of reactant and block, an amount of molecules within the reactant – block C interphase are much less than a number of reactant molecules in the other interphases.

Figure 6.5a shows the well dispersion of Reac-C4 in the nanoparticle. In addition, its degree of dispersion was observed to be more significant than observed in the case of Reac-OPh. Accordingly, both cases demonstrated a strong evidence to claim that the high solubility of reactant molecules in the shell domain of micelle improves the accessibility of reactant to the reactive sites. From Figure 6.5b, the RDF plots of the reactant and block A were found to be overlapped since both components were extensively associated. As a result, the thickness of its interphase with block A was measured to be $5r_c$.

The important findings from these two simulations are that these reactants, whose rate of HKR was measured to be comparably faster than other cases,[4] were observed to be associated with the shell due to its high solubility in this domain. Although there are more to define in between the rate of the HKR in the micelle and the results obtained from this simulation, the incorporation of reactants in the nanoreactor can be considered as one of clinchers that govern the permeation of reactants into the reactive core.
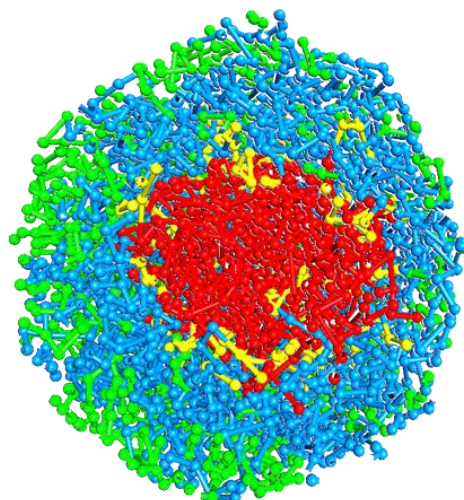
(a)
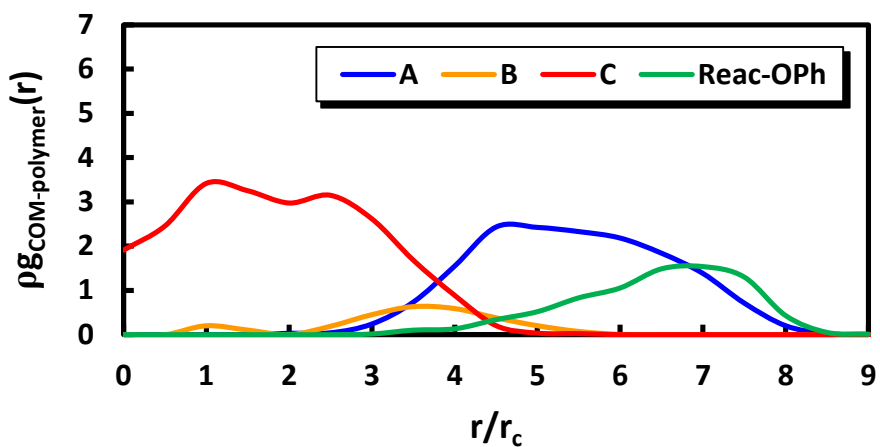
(b)

Figure 6.4. Results of DPD simulation with Reac-OPh. (a) is the cross-sectional view of micellar structure. Blue, yellow, red, and green colored regions indicate bead A, B, C (the coarse-grained PMOX, PBOX, and PSCoX blocks), and Reac-OPh, respectively. (b) is the RDF plot of four components from the center of micellar structure.
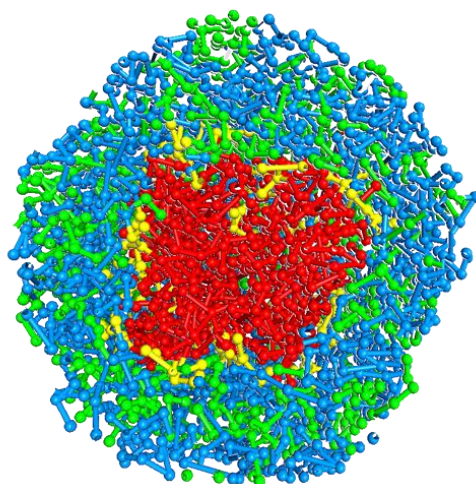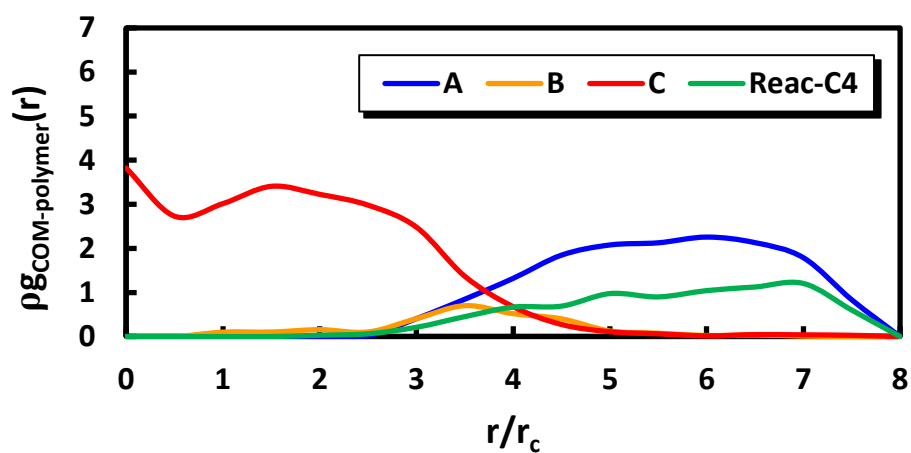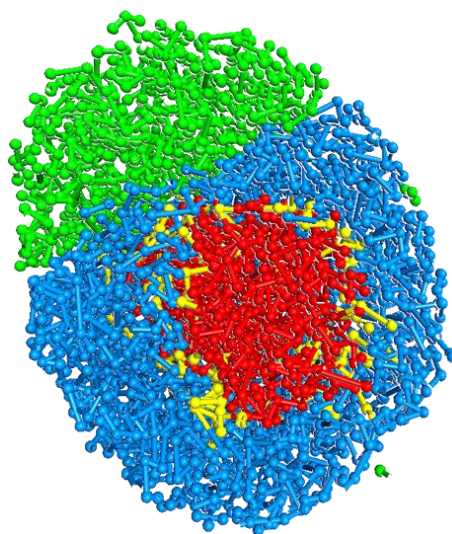
(a)

(b)

Figure 6.5. Results of DPD simulation with Reac-C4. (a) is the cross-sectional view of micellar structure. Blue, yellow, red, and green colored regions bead A, B, C (the coarse-grained PMOX, PBOX, and PSCoX blocks), and Reac-C4, respectively. (b) is the RDF plot of four components from the center of micellar structure.

6.3.2. Reac-Ph and Reac-Cl

Reac-Ph and Reac-Cl, the HKR of which was slow in the nanoreactor system[4], were characterized to be less miscible in the micelle structure than the first two reactants. This fact is illustrated in Figure 6.6 and 6.7. Figure 6.6a shows that a cluster of Reac-Ph molecules was formed as the result of the equilibration process. Since this reactant was rarely absorbed by the nanostructure, the independent domain of reactant appeared as minimizing the contact area with the solvent and polymers. The self-assembly of reactant aggregate appeared on the side of polymeric micelle. The shape of this aggregate can be concluded to be the most optimal regarding the thermodynamic stability because 1) the reactant molecules were incompatible with the selective solvent than the organic compounds and 2) the repulsive interaction between the reactant and micelle was too excessive to be associated The distribution plot exhibits a high peak of reactant molecules, which is positioned in between $(5 = 10.5)r_c$. Hence, the both qualitative and quantitative evidences lead to the conclusion that the nature of strong segregation between Reac-Ph and block copolymer would cause to slow the completion of the HKR.

Another reactant with the slow rate, Reac-Cl, exhibited the similarity to the Reac-Ph case. Figure 6.7a showed that only few number of reactant molecules were seen in the shell domain due to the strong segregation. Based on the comparison with the case of Reac-Ph, while Reac-Ph molecules minimized the contact with the micelle, Reac-Cl molecules were found to be radially spread on the surface of nanostructure as forming a thin interphase with block A. Additionally, some amount of Reac-Cl was observed in the internal structure of micelle; on the other hand, no molecule of Reac-Ph was found either in the shell or near the core. The RDF plots from the both cases lead to the same conclusion.

(a)

(b)

Figure 6.6. Results of DPD simulation with Reac-Ph. (a) is the cross-sectional view of micellar structure. Blue, yellow, red, and green colored regions indicate bead A, B, C (the coarse-grained PMOX, PBOX, and PSCoX blocks), and Reac-Ph, respectively. (b) is the RDF plot of four components from the center of micellar structure.
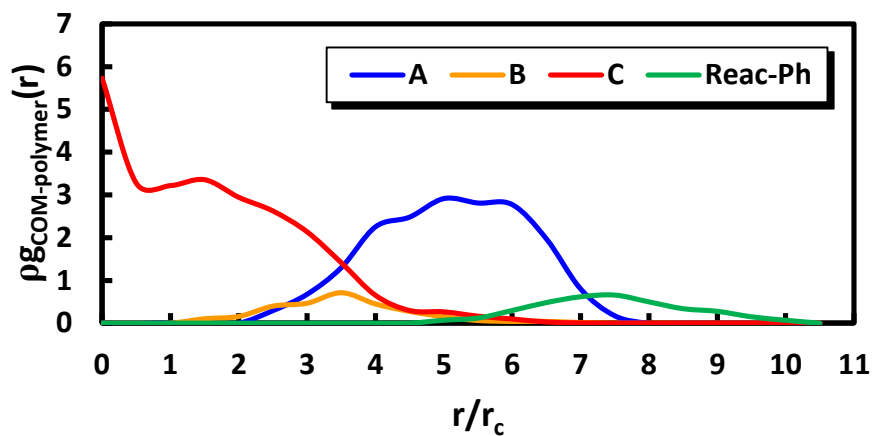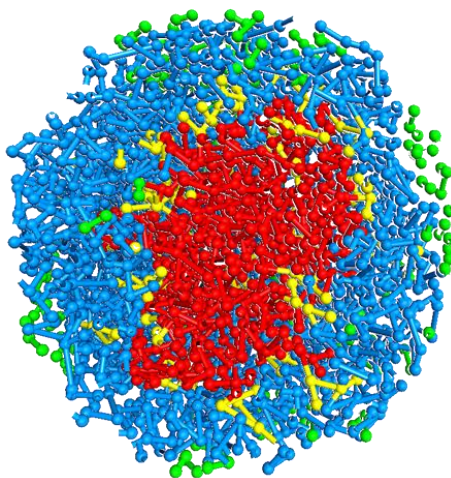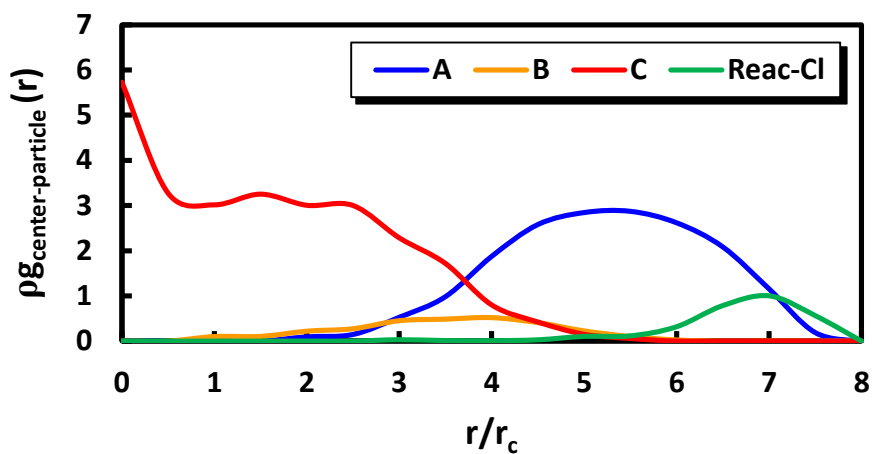
(a)

(b)

Figure 6.7. Results of DPD simulation with Reac-Cl. (a) is the cross-sectional view of micellar structure. Blue, yellow, red, and green colored regions indicate bead A, B, C (the coarse-grained PMOX, PBOX, and PSCoX blocks), and Reac-Cl, respectively. (b) is the RDF plot of four components from the center of micellar structure.

*6.3.3. Comparison with Previous χ_{FH} Parameters*

The previous χ_{FH} parameters were calculated as a function of compositions. Moreover, the energy of mixing was independently calculated using the mixture system. The details of this calculation were mentioned in Chapter 5. In contrast, the χ_{FH} parameters that are the basis of DPD repulsion parameters are calculated specifically using the Hildebrand Solubility parameters of each component. In this case, no mixture system was simulated to estimate the χ_{FH} parameters as expressed by Equation 5. Accordingly, as revealed from the description of calculation, the χ_{FH} parameters for DPD simulations are obtained via less complicated process, the cost of which is considered to be effective for the multicomponent mixture system. For this reason, it seems necessary to compare one set of parameters to another in order to identify any possible deficiency in the current scheme of χ_{FH} parameter calculation and solutions to improve the quality of parameters.

Figure 6.8 shows the trendlines of χ_{FH} parameter changes as a function of variety of reactant and variety of polymer. In the previous calculation, since the weight fraction of components was taken as one of variables in the calculation, there are three curves corresponding to weight fractions of reactant: 15 wt%, 45 wt%, and 70 wt%. In contrast, the χ_{FH} parameter based on the solubility parameter of components was independent from the weight fraction of components, which results in a single data point for each case.

Primarily, for the robust comparison between two sets of χ_{FH} parameters, it was necessary to select the curve with a specific weight fraction of reactants. The set of parameters with 70 wt% of reactant was assumed to be suitable data set for the comparison, specifically for the reactant-PMOX mixture. It was anticipated that an excessive amount of reactant molecules would surround the micellar structure due to their chemical affinity as organic compounds. The overall trend of both 70 wt% reactant and χ_{FH} parameters in DPD simulation look alike regardless of the true value of those parameters. For instance, the parameters for the Reac-C4 and Reac-OPh are calculated to be relatively smaller than the values from the case of Reac-Ph and Reac-Cl.
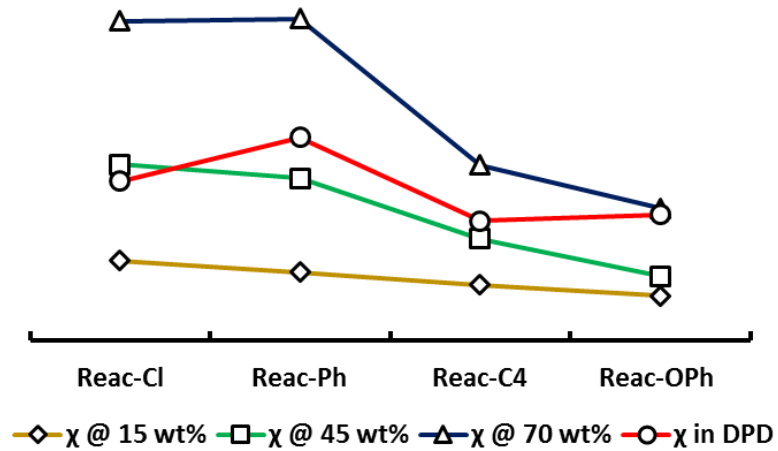
(a)
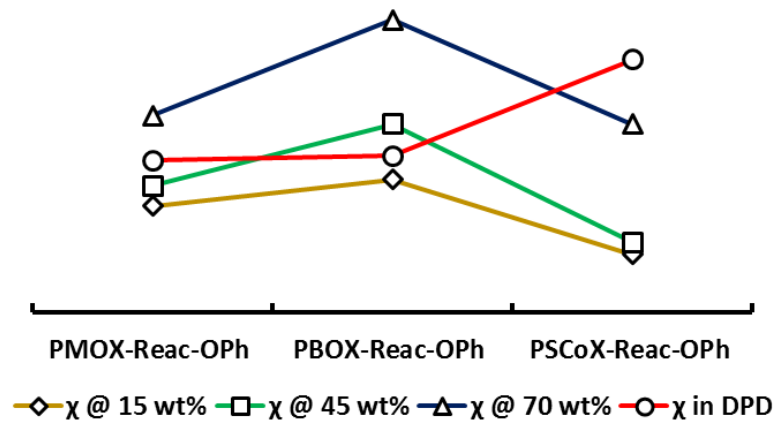
(b)

Figure 6.8. Line plots of χ_{FH} parameters. Lines display the trend of parameter changes along the x-axis in each case. Red colored line was specifically moved to the center of chart for fair comparison. Plot (a) displays the trends of parameters as a function of variety of reactant. Plot (b) displays the trends of parameters as a function of variety of polymer.

The noticeable difference based on the trendlines is that Reac-C4 was predicted to be more compatible with PMOX than Reac-OPh according to the Hildebrand Solubility

114

parameter based χ_{FH} parameters. Moreover, as shown in Figure 6.8b, the χ_{FH} parameters in DPD simulation were in the increasing trend, which means that the solubility of reactant in the micellar structure is deteriorated along the path from the solvent to the core. The same trend can be found from the other reactants, which are included in Appendix C with the numerical data. This result explains why almost no reactant molecule was found in the core domain from the DPD simulations.

In conclusion, it is suggested that the discrepancy between two calculations is evidently caused by different variables used in the calculation of χ_{FH} parameters. Specifically, the characterization in Chapter 5 reflected the particular interactions among functional groups; however, no inclusion of mixture system in scaling the degree of phase segregation was not able to do so. In order for enhancing the quality of DPD simulation, it is desired to develop computational methodologies to characterize and include the characteristic interactions among functional groups in the calculation of DPD repulsive parameters. Also, as χ_{FH} parameters in Chapter 5 were the composition dependency, the preparation of DPD parameters should take the effects of polymer size into account.

6.4. Conclusions

A series of DPD simulations were employed to study the association of reactant/product molecules with POX block copolymer based multicompartment micelle. Since the DPD parameters are converted from the χ_{FH} parameters that are based on the Hildebrand Solubility parameters of each components, it is important to check not only the versatility and efficiency of DPD simulation as a meso-scale simulation but also whether or not the nature of phase segregation characterized in this study is consistent with the information obtained in Chapter 5 for the further implementation of DPD simulation.

Via a number of attempts, the preliminary DPD simulation determined the block sequence of $A_{50}B_2C_2$ as a coarse-grained POX block copolymers whose assembly is determined to be micellar. The aggregation number was 71 in this model. Both the cross

section of the obtained aggregate and its RDF plot exhibited the structural features of micelle as described in the definition of micelle.

Next, the incorporation of reactant and product molecules in the micellar structure was investigated. The simulation showed that Reac-C4 and Reac-OPh molecules were well soluble in the nanoreactor, especially in the hydrophilic shell domain. On the other hand, Reac-Ph and Reac-Cl molecules were comparably insoluble in the nanostructure. These findings were consistent with the conclusions in Chapter 5 that the solubility of reactant in the nanoreactor is strongly correlated to the rate of HKR in the nanoreactor.

There are, however, two things that were inconsistent with the findings in Chapter 5. First, the miscibility of Reac-C4 in the PMOX shell domain was characterized to be more significant than the miscibility of Reac-OPh, which was observed to be the other way around in the previous study. Second, the increasing trend of χ_{FH} parameters as the reactant molecules is entering into the interior of micelle was not found in Chapter 5, as well. It is assumed that this inconsistency was caused by the involvement of different variables in the calculation scheme for the χ_{FH} parameters.

Using DPD simulation, macromolecular structure like multicompartment micelles is efficiently mimicked and analyzed. However, as stated, the loss of details is significant as coarse-graining the polymer structure. It will be valuable to develop a methodology to parameterize the specific interaction among functional groups to substantially enhance the quality of simulation.

6.6. References

[1]   Chandrawati, R.; Van Koeverden, M.P.; Lomas, H.;Caruso, F. *J. Phys. Chem. Lett.* **2011**, *2*, 2639.

[2]   Balasubramanian, V.; Onaca, O.; Ezhevskaya, M.; Van Doorslaer, S.; Sivasankaran, B.;Palivan, C.G. *Soft Matter* **2011**, *7*, 5595.

[3]   Cotanda, P.; Lu, A.; Patterson, J.P.; Petzetakis, N.;O'Reilly, R.K. *Macromolecules* **2012**, *45*, 2377.

[4]   Liu, Y.; Wang, Y.; Wang, Y.; Lu, J.; Piñón, V.;Weck, M. *J. Am. Chem. Soc.* **2011**, *133*, 14260.

[5]   Lu, A.; Cotanda, P.; Patterson, J.P.; Longbottom, D.A.;O'Reilly, R.K. *Chem. Commun.* **2012**, *48*, 9699.

[6]   Monteiro, M.J. *Macromolecules* **2010**, *43*, 1159.

[7]   Onaca, O.; Hughes, D.W.; Balasubramanian, V.; Grzelakowski, M.; Meier, W.;Palivan, C.G. *Macromol. Biosci.* **2010**, *10*, 531.

[8]   Renggli, K.; Baumann, P.; Langowska, K.; Onaca, O.; Bruns, N.;Meier, W. *Adv. Funct. Mater.* **2011**, *21*, 1241.

[9]   Lu, A.;O'Reilly, R.K. *Curr. Opin. Biotechnol.* **2013**, *24*, 639.

[10]   O'Reilly, R.K.; Hawker, C.J.;Wooley, K.L. *Chem. Soc. Rev.* **2006**, *35*, 1068.

[11]   Liu, Y.; Piñón, V.;Weck, M. *Polym. Chem.* **2011**, *2*, 1964.

[12]   Tanner, P.; Onaca, O.; Balasubramanian, V.; Meier, W.;Palivan, C.G. *Chem. Eur. J.* **2011**, *17*, 4552.

[13]   Rösler, A.; Vandermeulen, G.W.M.;Klok, H.-A. *Adv. Drug Del. Rev.* **2001**, *53*, 95.

[14]   Procházka, K.; Baloch, M.K.;Tuzar, Z. *Makromol. Chem.* **1979**, *180*, 2521.

[15]   Guo, A.; Liu, G.;Tao, J. *Macromolecules* **1996**, *29*, 2487.

[16]   Lu, A.; Smart, T.P.; Epps, T.H.; Longbottom, D.A.;O'Reilly, R.K. *Macromolecules* **2011**, *44*, 7223.

[17]   Hoogerbrugge, P.J.;Koelman, J.M.V.A. *Europhys. Lett.* **1992**, *19*, 155.

[18]   Koelman, J.;Hoogerbrugge, P.J. *Europhys. Lett.* **1993**, *21*, 363.

[19]   Groot, R.D. *J. Chem. Phys.* **2003**, *118*, 11265.

[20]   Groot, R.D.;Warren, P.B. *J. Chem. Phys.* **1997**, *107*, 4423.

[21]   Zhong, C.;Liu, D. *Macromol. Theory Simul.* **2007**, *16*, 141.

[22]   Huang, J.; Wang, Y.;Laradji, M. *Macromolecules* **2006**, *39*, 5546.

[23]   Symeonidis, V.; Em Karniadakis, G.;Caswell, B. *Phys. Rev. Lett.* **2005**, *95*, 076001.

[24]   Schulz, S.; Kuhn, H.; Schmid, G.; Mund, C.;Venzmer, J. *Colloid. Polym. Sci.* **2004**, *283*, 284.

[25]   Qian, H.-J.; Lu, Z.-Y.; Chen, L.-J.; Li, Z.-S.;Sun, C.-C. *Macromolecules* **2005**, *38*, 1395.

[26]   Liu, D.;Zhong, C. *Macromol. Rapid Commun.* **2006**, *27*, 458.

[27]   Liu, D.;Zhong, C. *Macromol. Rapid Commun.* **2005**, *26*, 1960.

[28]   Xu, Y.; Feng, J.; Liu, H.;Hu, Y. *Molecular Simulation* **2006**, *32*, 375.

[29]   Yamamoto, S.; Maruyama, Y.;Hyodo, S.-a. *J. Chem. Phys.* **2002**, *116*, 5842.

[30]   Tang, Y.; Liu, S.Y.; Armes, S.P.;Billingham, N.C. *Biomacromolecules* **2003**, *4*, 1636.

[31]   Underhill, R.S.;Liu, G. *Chem. Mater.* **2000**, *12*, 3633.

[32]   Li, X.; Pivkin, I.V.; Liang, H.;Karniadakis, G.E. *Macromolecules* **2009**, *42*, 3195.

[33]   Soddemann, T.; Dünweg, B.;Kremer, K. *Phys. Rev. E* **2003**, *68*,

[34]   Chen, S.; Guo, C.; Hu, G.-H.; Liu, H.-Z.; Liang, X.-F.; Wang, J.; Ma, J.-H.;Zheng, L. *Colloid. Polym. Sci.* **2007**, *285*, 1543.

[35]   Gohy, J.-F.; Willet, N.; Varshney, S.; Zhang, J.-X.;Jérôme, R. *Angew. Chem. Int. Ed.* **2001**, *40*, 3214.

CHAPTER 7

OUTLOOK

We utilized and implemented computational methodologies to study a supramolecular micellar structure and its application, nanoreactor. This task was done through rigorous scale-up procedure using both atomistic and mesoscopic simulations. Primarily, density functional theory (DFT) calculation was used to characterize the smallest unit of complex molecules in the multicomponent mixture system. The following step involved transferring the information achieved by DFT calculation to larger scale simulation, such as molecular dynamics (MD) simulation. Lastly, based on the atomistic simulation results, we performed a series of dissipative particle dynamics (DPD) simulations to study a full body of polymeric multicompartment micelle. In the course of research, we built a systematic procedure to minimize the complexity of computation and efficiently characterize macromolecular structures and its application.

The most well-known properties of amphiphilic materials are its possession of both hydrophilic and hydrophobic components in a single body. As included in Chapter 3, we investigated the wettability alteration of hydrophilic calcite surface by the adsorption of carboxylate molecules. Via a series of DFT calculations and analysis, the thermodynamics involved in the adsorption of carboxylate molecules on the surface were obtained with the geometry of adsorbent. The force field fitting technique was employed to transfer and reproduce this information from the expensive calculation to atomistic MD simulation. Using a number of simulation techniques, it was determined that the non-covalent interaction between the ionic component of carboxylate and the hydrophilic surface formed a thermodynamically stable monolayer of carboxylate that altered the wettability of surface from hydrophilic to hydrophobic. As a result, the secondary adsorption of organic phase occurred.

In Chapter 4, we simulated sodium dodecyl sulfate (SDS) surfactant micelle to understand the particularities of micellar structure. Since there as a plenty of studies done on this materials by both computation and experiment, it was an ideal candidate materials for us to test the performance of modeling scheme using MD simulation based on our current force field parameters. In addition, it was important to develop computational toolkits to characterize the thermodynamic and structural properties of micelle models. We performed long and rigorous MD simulations to obtain the equilibrated SDS micelle and validated the modeling protocol by comparing its structural features to both computational and experimental results. Once it was confirmed that the target structure was successfully modelled, we extended our study to the thermodynamics involved in the conservation of micellar structure in the selected solvent phase. The free energy change was calculated for both the insertion of water molecule into the hydrophobic core and the dissociation of surfactant molecule from the micellar structure. The results of calculation indicated that both processes were highly unspontaneous.

However, in the transition from the fundamental study of micelle to its application, we realized that it would not be efficient to directly attack a full body of nanostructure due to the complexity of calculation. In the case of nanoreactor study (Chapter 5), poly(2-oxazoline)s (POXs) multicompartment micelle was studied using computational methodologies. The known size of this micelle structure was approximately 50 nm of radius, which would contain more than couple millions of atoms in the system. We attempted to simulate the miniaturized size micelle but it was not feasible to verify the uncertainty from the difference in the size. Moreover, the cost of calculation was too expensive to accomplish the goal of study.

For these reasons, the Flory-Huggins theory was employed. The major goal of nanoreactor study was to determine the limiting factor for its performance. The possible problem with nanoreactor is the limitation by the permeation of reactant molecules into the reactive core. Instead of simulating a full body of micelle for investigating the permeation

of molecules, we characterized the nature of interaction between reactant and nanostructure to correlate with permeation. Because the permeation of a given molecule in a given media is govern by not only the structural properties but also the solubility of the molecule in a permeate, it was certain that there should be a strong correlation between the solubility and the rate of reaction in the nanoreactor. Therefore, we hypothesized that each region would result in the distinct difference in the degree of association with reactant since each region was an assembly of blocks that possess similar physical and chemical properties. To complete this task, the Flory-Huggins interaction (χ_{FH}) parameters, whose magnitude indicates the degree of segregation between two components, were generated from the binary mixture of blocks and reactants. The calculation was specifically done using the binary mixture system that contains a homopolymer of each block and reactant molecules. According to the results, a group of reactants, the reaction rate of which was significantly low in the nanoreactor, were much less miscible in the POX polymers than other reactants.

In Chapter 6, because the analysis by χ_{FH} parameters did not include a full body of micelle, we utilized and implemented DPD simulation as a mesoscopic simulation that enables to efficiently simulate extensively large systems. The DPD simulation uses a coarse-graining method that replaces a number of atoms with a bead. The interaction among those beads is expressed by the repulsion that is parameterized from the phase segregation. Therefore the input parameters of DPD particles are converted from the χ_{FH} parameters. However, the χ_{FH} parameters in this simulation are calculated with different variables from the variables used in Chapter 5. For this reason, not only did we illustrated the association of reactant molecules with the nanoreactor, but also the comparison of two sets of χ_{FH} parameters was done to check their consistency. In conclusions, the results of DPD simulation provided both qualitative and quantitative data that lead to the same conclusion as Chapter 5. However, there was a noticeable discrepancy between two sets in terms of both the magnitude and trend of χ_{FH} parameters, which were addressed in Chapter 6.

Overall, each part of the research contributed to developing the computational method to characterize micellar structure. Through both atomistic and mesoscopic simulation, the systematic analysis was accomplished. From a number of trials, the scheme of DPD simulation revealed a great potential as an ideal tool to simulate and characterize such a large scale system. Meanwhile, it was learned that the quality of DPD simulation can be further improved by elaborating the coarse-graining process including the parametrization of the thermodynamics involved in the interaction among components. From the comparison between the results of Chapter 5 and Chapter 6, it was evident that the Hildebrand Solubility parameter based χ_{FH} parameters might be insufficient to convey the detail information of particular thermodynamics within the interaction among functional groups, multiple of which can be contained within a monomeric unit. In addition, the use of a number of identical beads to represent a single compound might be another source of effort that needs to be corrected. As shown in Chapter 6, one monomeric unit contained more than one functional group but only one type of bead was repeatedly used to describe the structural and thermodynamic properties of the unit.

The calculation of χ_{FH} parameters is sufficiently quick enough to handle a broad range of materials. However, it came across to us that the coarse-grained polymeric structure and their input parameters should be more sectionalized to reproduce the details of atomistic model for the quality assurance. With the efforts to enhance the quality of simulation, the results of DPD simulation should become great resources for the experimental purpose since it can deliver not only the details of the internal structure and the critical micellization conditions but also the thermodynamics involved in the evolution of amphiphilic materials. Continuing the χ_{FH} parameters based analysis in order to complete the investigation of molecular association with multicompartment micelle, we propose further computational study of the entire multicompartment micelle nanoreactor using multiscale modeling frame covering from quantum mechanics (QM) to mesoscale coarse-grained (CG) simulation methods such as DPD simulation. In this modeling frame,

122

full-atomistic details in structures and interaction energies of reactants/products and polymer blocks are characterized by QM and MD simulation and transferred via coarse-grained interaction parameters such as Flory-Huggins parameters to the larger scale level simulated by CG simulation method. Through this study, first, with given reactants and products, we will identify the optimal structure of multicompartment micelles by searching various block compositions, which will be evaluated by the association and distribution of reactants/products within the micelle, and then with the given micelle, we will identify the optimal reactants for better association and distribution. We believe that this computational modeling approach will accelerate the identification/development of optimal systems for desirable properties.

APPENDIX A

Additional Figures from Chapter 3

(a)

(b)
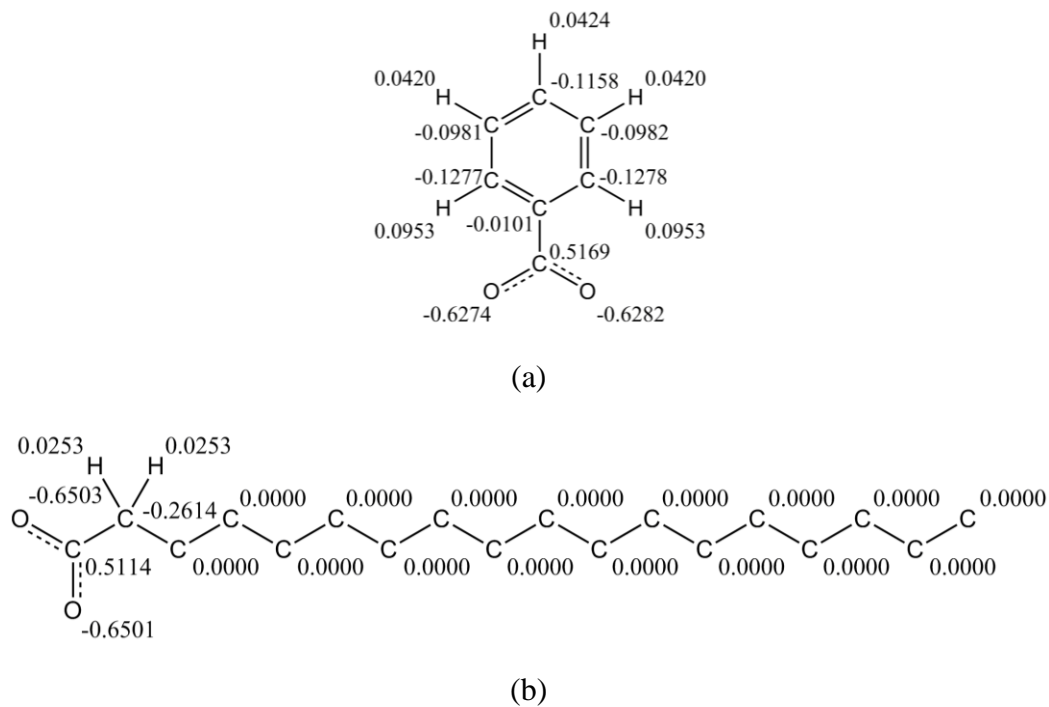
Figure A.1. Chemical structures and partial charges of (a) benzoate and (b) stearate.
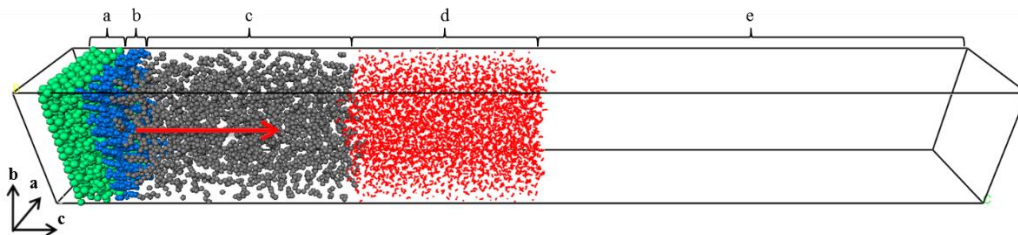
Figure A.2. Multi-phase system for steered molecular dynamics simulation: (a) calcite slab; (b) benzoate monolayer; (c) octane phase with 70 Å of thickness; (d) water phase with 60 Å of thickness; (e) vacuum. The red colored arrow indicates the direction of pulling benzoate during the Steered MD simulation.
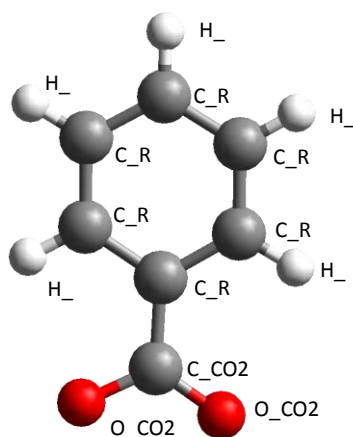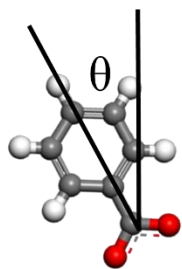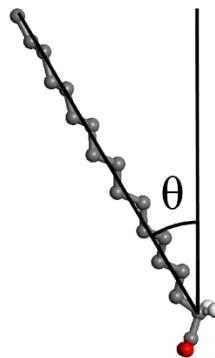

Figure A.3. Force field types used in Benzoate molecule. The red, grey and white balls denote oxygen, carbon and hydrogen, respectively.

Figure A.4. Tilt angles of (a) benzoate and (b) stearate. The red, grey, white colors denote oxygen, carbon and hydrogen, respectively.

APPENDIX B

B1. General

The following contents were provided by collaborators on the experiment from New York University.

B1.1. Materials

All reagents were purchased from standard suppliers and used as received unless otherwise stated. 2-Methyl-2-oxazoline, acetonitrile and chlorobenzene were distilled over CaH_2 and stored under dry argon and molecular sieves (4 Å). Methyltriflate was distilled over barium oxide and stored under dry argon at 4 °C. Dichloromethane was dried by passing through columns of activated alumina. Flash column chromatography was performed using silica gel 60 Å (230-400 mesh) from Sorbent Technologies. Methyl 3-(oxazol-2-yl)propionate (EsterOx, monomer **C**) was synthesized based on adapted literature procedures.[1]

B1.2. Measurements

^{1}H NMR and ^{13}C NMR spectra were recorded at 25°C on a Bruker AC 600 MHz / 400 MHz spectrometer. All chemical shifts are reported in parts per million (ppm) with reference to solvent residual peaks. Gel-permeation chromatography (GPC) was carried out using a Shimadzu pump coupled to a Shimadzu RI detector. A 0.03 M LiCl solution in *N*,*N*-dimethylformamide was used as eluent at a flow rate of 1 mL/min at 60 °C. A set of Polymer Standards columns (AM GPC gel, 10 μm, precolumn, 500 Å and linear mixed bed) was used. M_w^{app}, M_n^{app}, and *Đ* represent the apparent weight-average molecular weight, apparent number-average molecular weight, and dispersity index, respectively. Commercially available poly(styrene) standards were used for calibration. Hydrodynamic diameters of the cross-linked and uncross-linked micelles were

determined at 25 °C by dynamic light scattering (DLS) using a Protein Solution DynaPro instrument with a 663 nm laser module. SEM images were recorded on Carl Zeiss Merlin® Field Emission-Scanning Electron Microscope (FE-SEM). The accelerating voltage was 2 kv and the working distance was 3.9 mm. The SEM samples were prepared by depositing the sample methanol solution onto a piranha solution processed silicon wafer, followed by vacuum drying at room temperature. The particle size was measured by Zeiss FE-SEM built-in program SmartSEM User Interface.

B2. Preparation

B2.1. Monomer synthesis
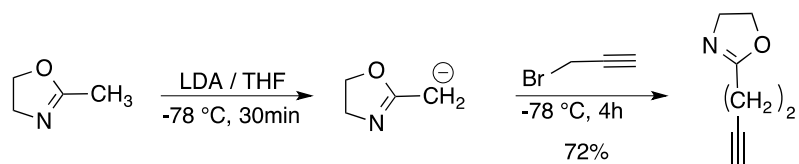
B2.1.1. Monomer B 2-(but-3-yn-1-yl)-4,5-dihydrooxazole

Prepare LDA in situ. Diisopropylamine (1.67 ml, 11.8 mmol) was dissolve in 20 ml THF. The reaction was cooled down to -78 °C and 2.5M *n*-butyllithium in Hexanes (4.724 ml, 11.8 mmol) was added. The reactions was stirred for five minutes at -78 °C followed by an ice-bath for another 15 minutes. The mixture was cooled back down to -78 °C and stirred for five minutes. Then 2-methyl-2-oxazoline (1.00 mL, 11.8 mmol) was added.[2] At -78 °C, the reaction was stirred for 30 minutes to generate the oxazoline anion. 80 wt% Propargylbromide in toluene (1.335 mL, 1.05 eq) was added and the mixture stirred at room temperature for 2.5 hours. The product was extracted with 20 mL water and 20 mL ethyl ether three times. The organic layer was dried with magnesium sulfate. After removal of the solvent, the residue was purified via silica gel column chromatography using ethyl acetate/CH_2Cl_2 (200/100). The yield was 78% which is a significant improvement to previously reported methodologies.[3] ^{1}H NMR (CDCl_3, 400

MHz, δ_{ppm} vs. TMS): 4.17 (t, J = 9.50 Hz, 2H,), 3,78 (t, J = 9.44 Hz, 2H), 2.45 (m, 4H), 1,93 (s, 3 ppm 1H). ^{13}C NMR (CDCl$_3$, 100 MHz, δ_{ppm} vs. TMS): 167.7, 136.7, 115.1, 54.1, 29. 7, and 27.1. MS (ESI): m/z calculated for C$_7$H$_9$NO, 123.15; found, 124.15 (M+H$^+$).
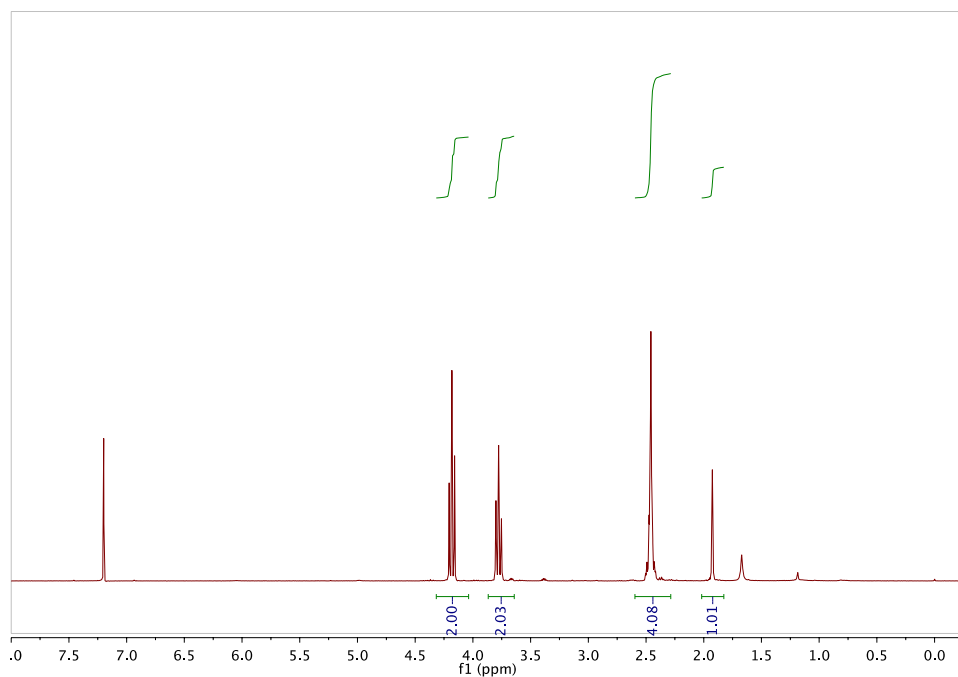

Figure B.1. ^{1}H NMR spectrum of monomer **B**.
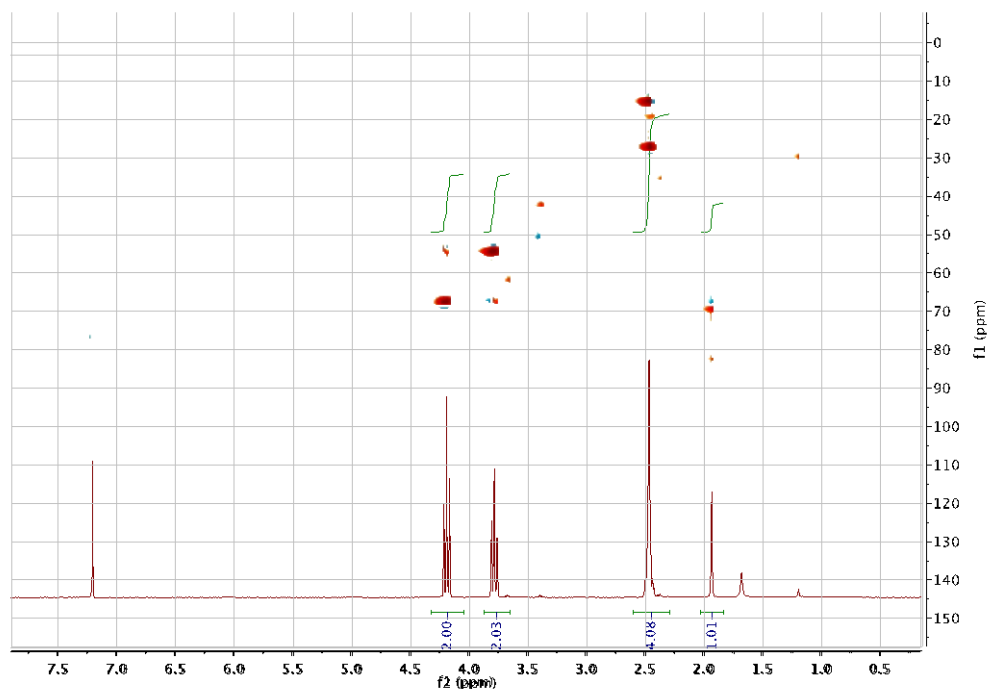
Figure B.2. HSQC NMR spectrum of monomer **B**.

B2.2 Polymer precursor

B2.2.1. Polymer 1

A typical procedure for the cationic ring-opening polymerization was as follow: Methyltriflate (28.29 µL, 0.25 mmol) was added to a solution of monomer **C** EsterOx (0.39 mL, 2.5 mmol) in chlorobenzene (1 mL) and acetonitrile (1 mL). The mixture was stirred for 24 hours at 70 °C. The polymerization was monitored via ^{1}H NMR spectroscopy. After monomer **C** was completely consumed, monomer **B** AlkyneOx (308 mg, 2.5 mmol) and chlorobenzene (1 mL) was added to the polymer solution under an argon atmosphere. The mixture was stirred for eight hours at 70 °C. After monomer **B** was fully consumed, monomer **A** MeOx (1.92 mL, 22.5 mmol) and acetonitrile (2 mL) were added. The solution was stirred at 70 °C for an additional 36 hours. After monomer **A** was fully consumed, the polymerization was terminated via the addition of water (50 µL, 0.5 mmol) and stirred at room temperature for four hours. The polymer was purified by dialysis against DCM and isolated by freeze-drying from dioxane. The repeat units for

A MeOx (a=62.1), **B** AlkyneOx (b=6.7), and **C** EsterOx (c=8.3) were determined by ^{1}H NMR spectroscopy end group analysis according to the methyl group from Methyltriflate at 3 ppm (Figure B3).
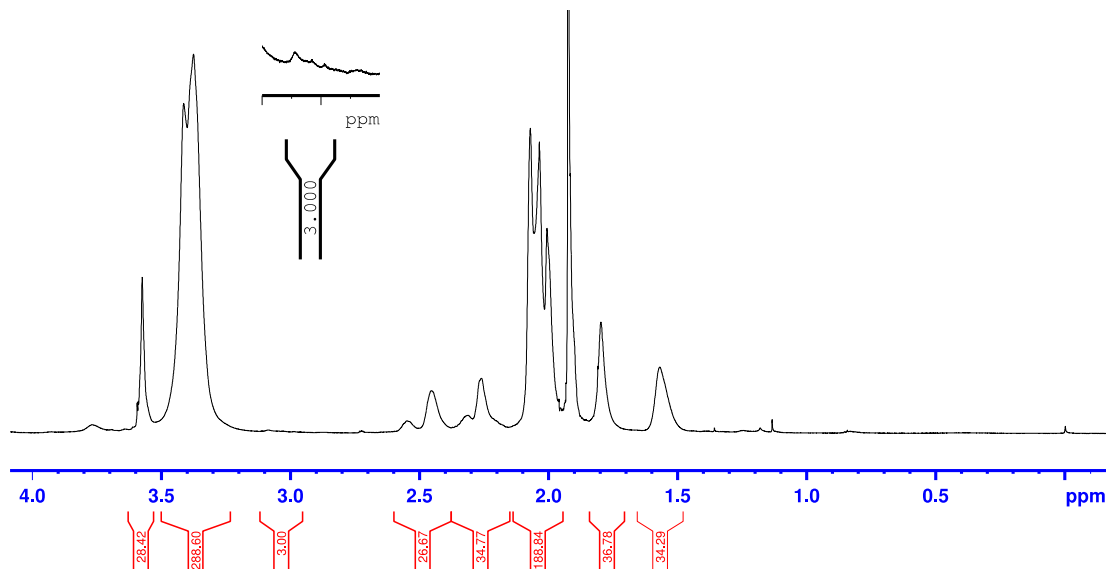

Figure B.3. ^{1}H NMR spectrum of triblock copolymer **2** in CDCl$_3$.

The molecular weight distributions were determined by GPC using DMF as the eluent: M_n^{app} = 7,700 g/mol, Đ = 1.22 (Figure B4).
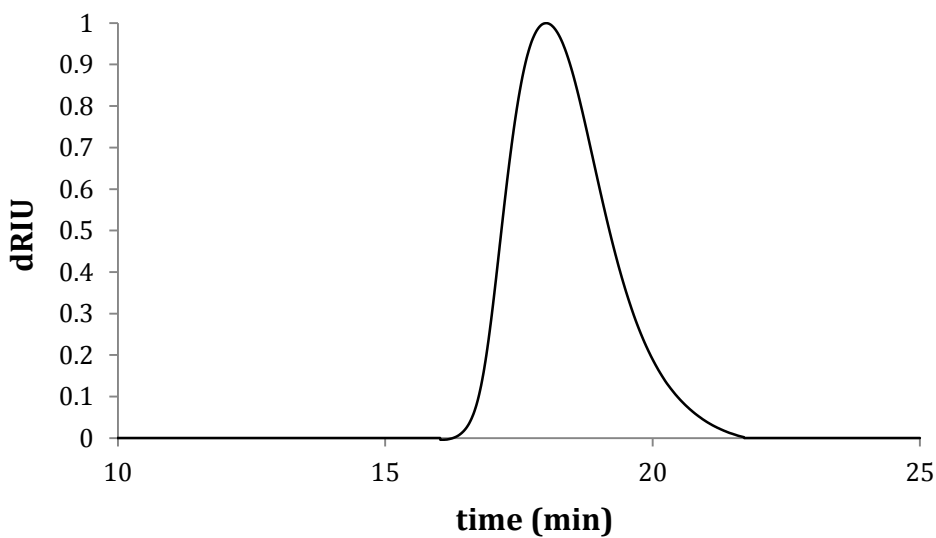

Figure B.4. Normalized gel-permeation chromatogram of triblock copolymer **1**.

131

B2.2.2. Polymer 2

Triblock copolymer **1** (200 mg) was dissolved in 20 mL methanol. Then, 20 mL of a 0.1 M LiOH solution was added. The mixture was stirred at 50 °C overnight. The solvent was removed under reduced pressure and the residue was redissolved in ten mL of water. The solution was cooled to 0°C and neutralized with 0.1 M HCl. The polymer was purified by dialysis against water and dried by lyophilization.

B2.2.3. Micelle supported salen (Polymer 3)

Polymer **2** (carboxylic group 1 eq, 200 mg) was dissolved in DMF (1 mg/mL). Hydroxyl-functionalized salen (1.2 eq, 176 mg), PyBrOP (1.4 eq, 189 mg) and DIPEA (3 eq, 150 ul) were added to the micelle solution. The mixture was stirred at room temperature for 24 hours, purified by dialysis and dried by lyophilization. The degree of salen functionalization was determined by MALDI-TOF (Figure B5). The peak shift indicated the attachment of four salen ligands to the hydrophobic block of polymer **2**.
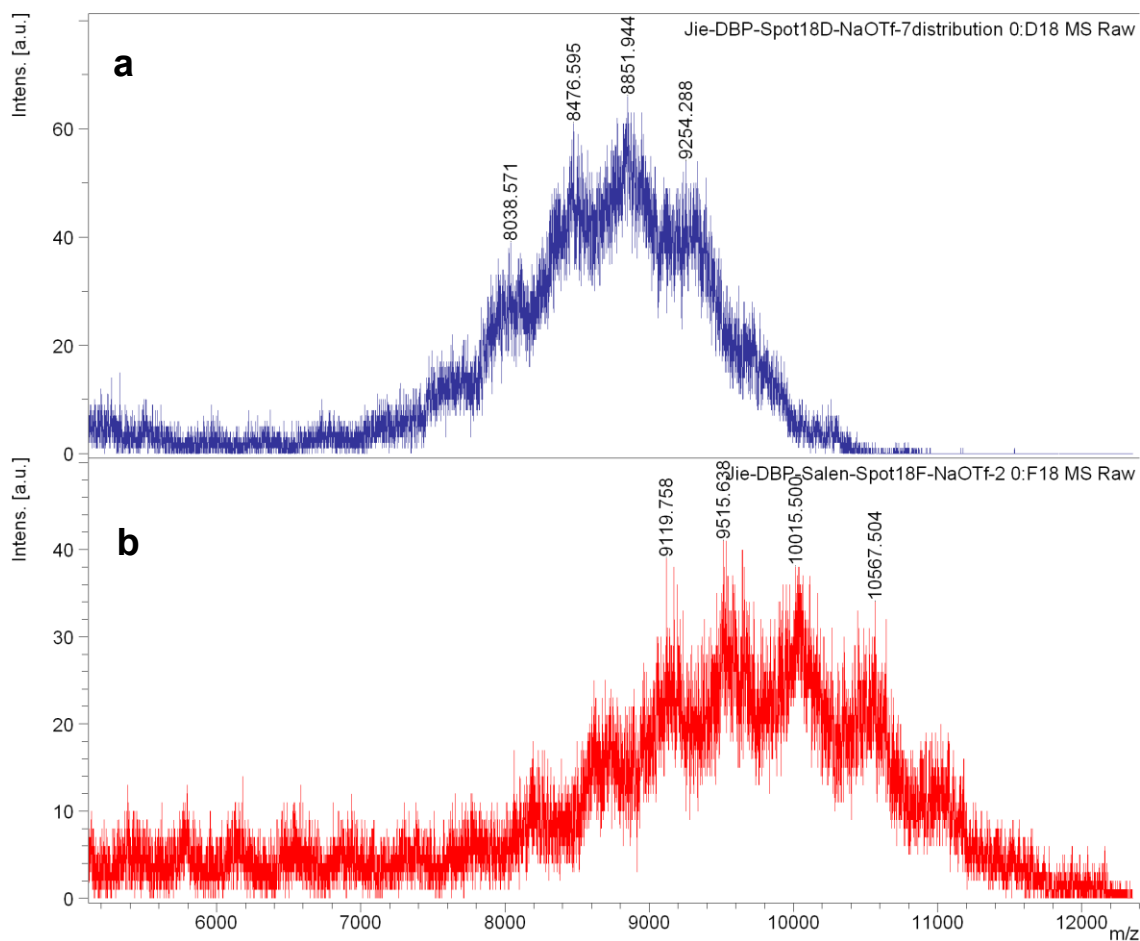
Figure B.5. MALDI-TOF mass spectrum of polymer **2** (a) and polymer **3** (b).

B2.3. Shell Crosslinked micelle supported Co-salen`

### B2.3.1. Micelle formation and cross-linking (micelle 4)

The amphiphilic triblock copolymer was dissolved in water with a concentration of 1 mg/mL. The crosslinking reagent 1,5-pentanedithiol (0.6 eq) was added to the micelle solution and the mixture was stirred at room temperature for two hours. The reaction was degassed via three freeze-pump-thaw cycles. The thiol-yne reaction was initiated by DMPA (0.1 eq) and irradiation with UV light (15W UVP Black Ray UV Bench Lamp XX-15L) while stirring for 24 hours at 4 °C. The reaction mixture was purified by dialysis and dried by lyophilization.

B2.3.2. Cobalt Metallation (Nanoreactor 5)

Crosslinked micelle **4** (1 eq based on salen ligand, 0.5 mmol) was transferred into a glovebox and dissolved in dry CH_3OH (0.5 mg/mL). Cobalt acetate tetrahydrate in dry methanol solution (2 eq, 0.1 M) was added to the micelle solution. The mixture was stirred at room temperature for 48 hours in the glovebox and then stirred in air for five hours. The color of the solution turned to dark brown indicating the formation of the oxidized Co(III)-salen complex. The excess cobalt salt was removed by passing the micelle solution through a celite plug. The cobalt content determined by ICP-MS was 1.3%.

B2.3.3. Dynamic light scattering and SEM analysis

The micelle formation and crosslinking were confirmed by DLS analysis. The hydrodynamic radii of micelle assemblies were around 45 nm in water (Figure B6 A). Before the covalent crosslinking, the micelle assemblies fell apart in non-selective solvents such as DMF as confirmed by the measured hydrodynamic radius of 5.7 nm (Figure B6 B). After crosslinking, the micelle assemblies survived in both selective (Figure B6 C) and non-selective solvents (Figure B6 D). The morphology of the SCM-based nanoreactor **5** was investigated by DLS and SEM. As shown in Figures S6 E and F, the hydrodynamic radius of **5**, determined by DLS, was 47 ± 5 nm, consistent with the radius of 50 ± 10 nm obtained by SEM.
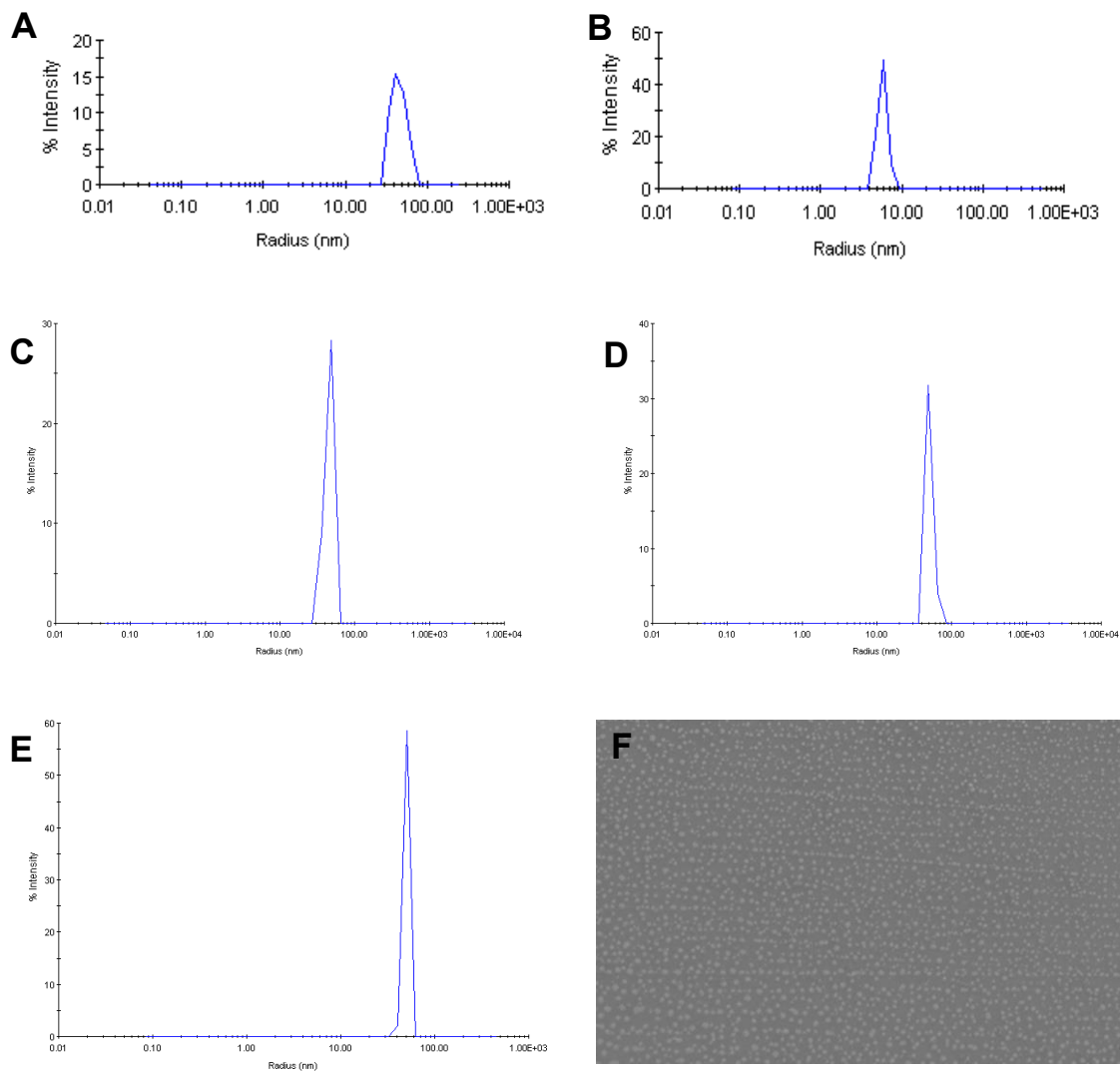
DLS/SEM	Block copolymer	Solvent	Size (nm)
A	**Polymer 3**	water	45 ± 3
B	**Polymer 3**	dimethylformamide	5.7 ± 0.8
C	**Micelle 4**	water	49 ± 5
D	**Micelle 4**	dimethylformamide	50 ± 6
E	**Nanoreactor 5**	water	47 ± 5
F	**Nanoreactor 5**	-	50 ± 10

Figure B.6. DLS results (A-E) and SEM image (F) of the micelle supported catalyst (scale bar: 300 nm).

B3. References

[1]   Zarka, M.T.; Nuyken, O.;Weberskirch, R. *Chem. Eur. J* **2003**, *9,*

[2]   Puts, R.D.;Sogah, D.Y. *Tetrahedron Lett.* **1994**, *35,* 5779.

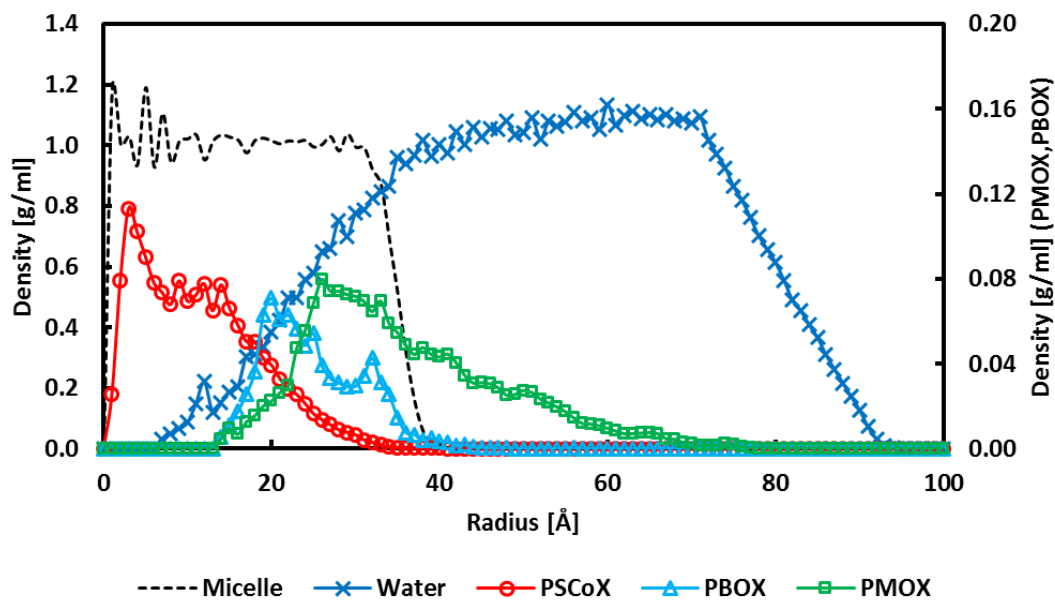[3]   ten Brummelhuis, N.;Schlaad, H. *Polym. Chem.* **2011**, *2,* 1180.

APPENDIX C

Additional Table and Figures for Chapter 6

Table C.1. List of Flory-Huggins interaction parameters for the DPD simulation and the parameters estimated in Chapter 5.

| Polymer Type	Molecules	χ in DPD	χ @ 15 wt%	χ @ 45 wt%	χ @ 70 wt%
PMOX	Reac-Cl	1.67	5.58	6.66	9.97
	Reac-Ph	3.48	4.79	6.51	11.09
	Reac-C4	0.00	3.88	3.21	5.14
	Reac-OPh	0.26	3.14	1.36	4.72
PBOX	Reac-Cl	1.91	3.54	6.33	9.72
	Reac-Ph	3.82	4.44	2.90	6.75
	Reac-C4	0.01	3.32	2.54	6.99
	Reac-OPh	0.36	4.93	3.68	7.01
PSCoX	Reac-Cl	5.48	2.15	4.66	9.54
	Reac-Ph	8.50	-0.69	1.38	7.09
	Reac-C4	1.13	1.18	3.16	6.33
	Reac-OPh	2.43	-0.10	0.80	7.93
PMOX	Pro-Cl	0.09	3.17	0.20	3.13
	Pro-Ph	1.17	3.87	2.78	5.65
	Pro-C4	0.38	2.88	-0.76	1.10
	Pro-OPh	0.06	3.58	0.48	3.12
PBOX	Pro-Cl	0.15	4.25	1.63	4.00
	Pro-Ph	1.37	4.14	1.28	4.87
	Pro-C4	0.28	3.62	0.44	1.33
	Pro-OPh	0.12	3.60	1.76	3.87
PSCoX	Pro-Cl	1.82	0.47	-1.04	3.79
	Pro-Ph	4.53	-0.22	-0.90	5.60
	Pro-C4	0.18	-1.34	-1.82	1.65
	Pro-OPh	1.69	0.11	1.24	6.73
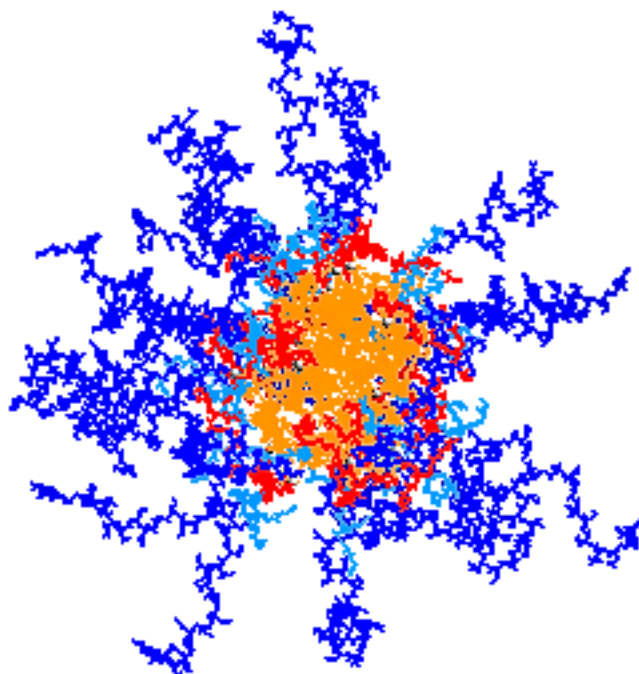
(a)

(b)

Figure C.1. Results of atomistic MD simulation. (a) is the equilibrated micelle structure after 50 ns of NVT-MD simulation. Blue and sky blue blocks denote PMOX and PBOX, respectively. Red and orange blocks denote PSCoX. Water molecules are omitted in (a). (b) is the corresponding radial density distribution plots of micelle. The block compositions used in this simulation is $[PMOX]_{18}[PBOX]_1[PSCoX]_1$ and the aggregate number is 30.
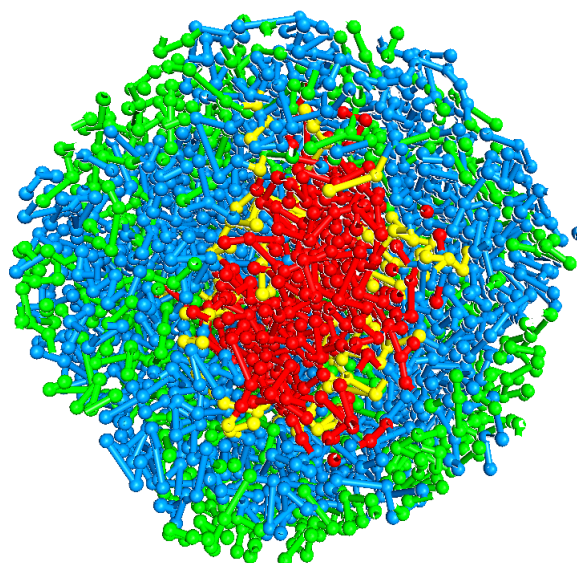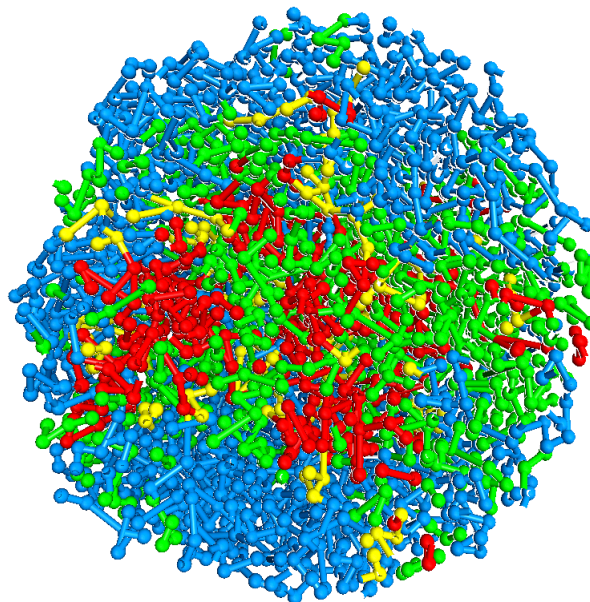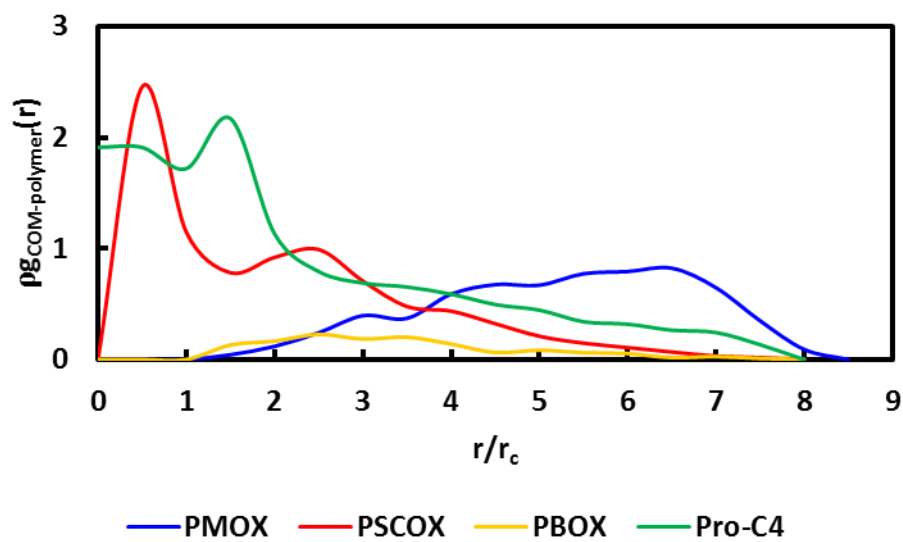
(a)
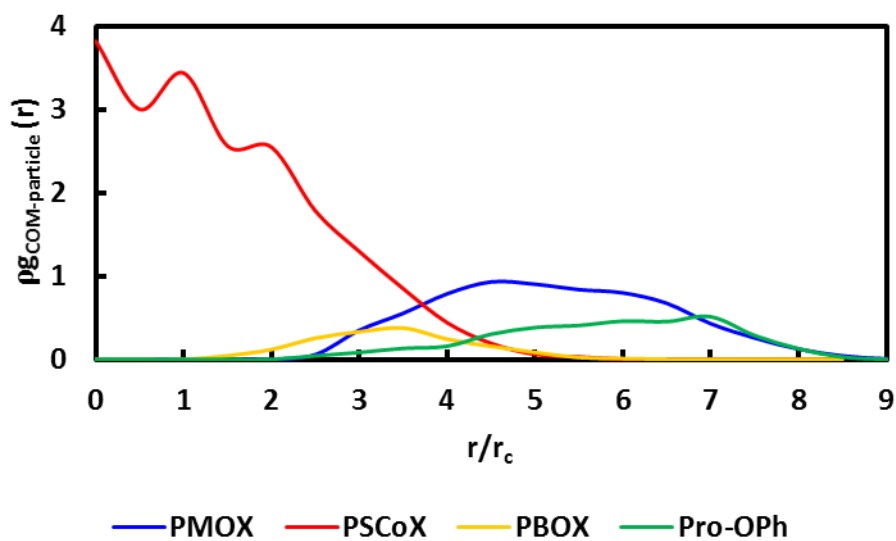
(b)

Figure C.2. Results of DPD simulation with Pro-OPh. (a) is the cross-sectional view of micellar structure. Blue, yellow, red, and green colored regions indicate bead A, B, C (the coarse-grained PMOX, PBOX, and PSCoX blocks), and Pro-OPh, respectively. (b) is the RDF plot of four components from the center of micellar structure.
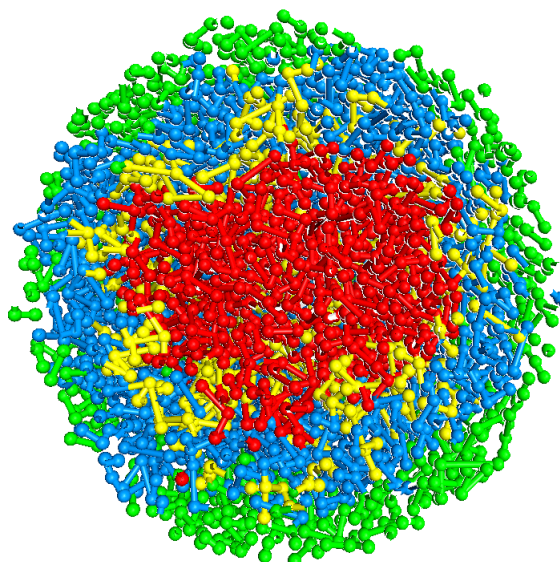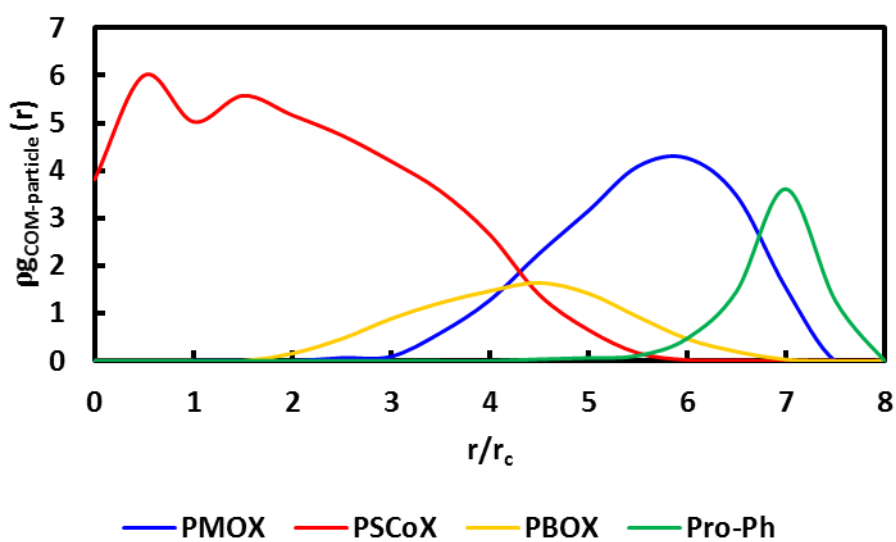
(a)

(b)

Figure C.3. Results of DPD simulation with Pro-C4. (a) is the cross-sectional view of micellar structure. Blue, yellow, red, and green colored regions indicate bead A, B, C (the coarse-grained PMOX, PBOX, and PSCoX blocks), and Pro-C4, respectively. (b) is the RDF plot of four components from the center of micellar structure.
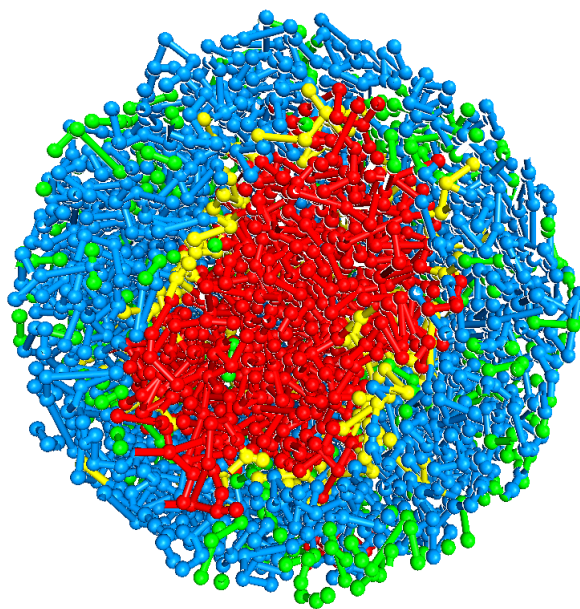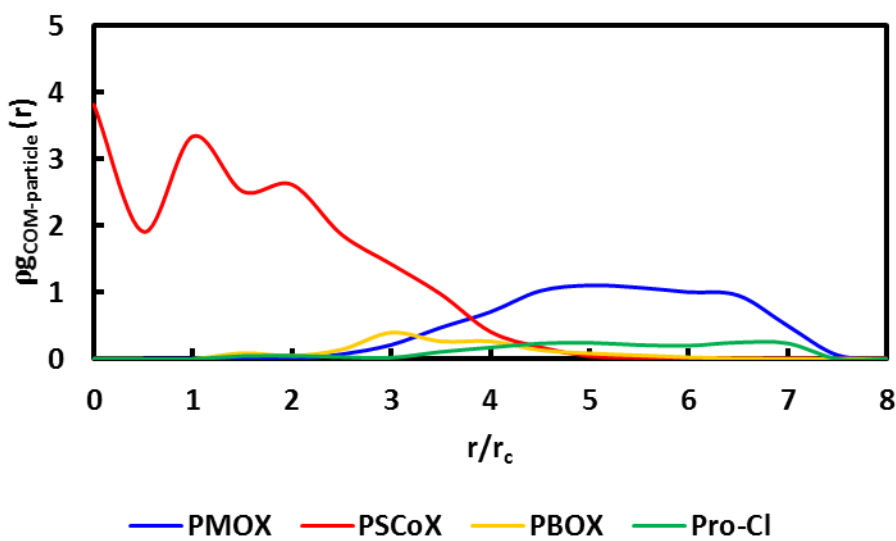
(a)

(b)

Figure C.4. Results of DPD simulation with Pro-Ph. (a) is the cross-sectional view of micellar structure. Blue, yellow, red, and green colored regions indicate bead A, B, C (the coarse-grained PMOX, PBOX, and PSCoX blocks), and Pro-Ph, respectively. (b) is the RDF plot of four components from the center of micellar structure.

(a)

(b)

Figure C.5. Results of DPD simulation with Pro-Cl. (a) is the cross-sectional view of micellar structure. Blue, yellow, red, and green colored regions indicate bead A, B, C (the coarse-grained PMOX, PBOX, and PSCoX blocks), and Pro-Cl, respectively. (b) is the RDF plot of four components from the center of micellar structure.